



universität
wien

DIPLOMARBEIT

Titel der Diplomarbeit

The Volcanic Earthquake Swarm of 1999 at the
Eastern Gakkel Ridge, Arctic Ocean:
A Case Study for a Comparison between a
Probabilistic- and a Conventional Teleseismic Algorithm

angestrebter akademischer Grad

Magister/Magistra der Naturwissenschaften (Mag. rer.nat.)

Verfasserin / Verfasser: Edith Korger
Matrikel-Nummer: A9708506
Studienrichtung (lt. Studienblatt): A416 - Geophysik
Betreuerin / Betreuer: O. Univ. Prof. Dipl.-Ing. Dr.phil. Ewald Brückl

Wien, im Juni 2010

Contents

List of Tables	v
List of Figures	vii
0 INTRODUCTION	1
1 GEOLOGIC SETTING - Mid-Ocean Ridges	3
1.1 Spreading Rate and Thermal Structure	6
1.2 Spreading Rate and Axial Topography	10
1.2.1 Slow Spreading Ridges	11
1.2.2 Ultraslow Spreading Ridges	13
1.3 The 85°E Region at Gakkel Ridge: Observations and Interpretation	30
1.3.1 The Teleseismic Earthquake Swarm of 1999	30
1.3.2 Analysis of the Teleseismic Earthquake Swarm of 1999	31
1.3.3 Geological Framework of the 1999 Swarm at the Volcanic Complex	36

TABLE OF CONTENTS

2	Earthquake LOCALIZATION	39
2.1	Linear Inverse Localization - Hyposat	42
2.2	Nonlinear Inverse Localization - NonLinLoc	43
3	DATA and LOCALIZATION ALGORITHM	49
3.1	Data: Phase Readings	49
3.2	Constraints on Dataset, Localization Parameters, Velocity Model	52
3.2.1	Testing of Dataset	52
3.2.1.1	Epical Coverage	53
3.2.1.2	Azimuthal Coverage	57
3.2.2	Testing of Localization Algorithm	59
3.2.2.1	Search for Maximum of the PDF - Variation in Initial Number of Cells	59
3.2.2.2	Testing of Weighting Station Clusters	63
3.2.3	Testing of Global- and Local Velocity Model	66
4	RESULTS of the Non-Linear Relocalization and of Uncertainties	73
4.1	Quality of Swarm Relocation	75
4.2	Selection of Well-Constrained Events	79
4.3	Stability and Uncertainties of the Solution	82
4.3.1	Stability of well-located Events	82
4.3.2	Uncertainties	83
4.4	Hypocentral Depth Evaluation	84
4.5	Comparison of NonLinLoc probabilistic localization with Hyposat least- squares based algorithm	88
4.6	Evaluation of Station Residuals	91

5	INTERPRETATION	95
5.1	Temporal Analysis	96
5.2	Spatiotemporal Analysis	100
5.3	Source Mechanisms	105
5.4	Final Evaluation of the 1999 Earthquake Swarm	113
5.5	Outlook	115
	Acknowledgements	117
	Bibliography	119
A	Abstract	125
B	Kurzbeschreibung	127

List of Tables

1.1	Segments of Gakkel ridge	17
1.2	Expeditions visiting Gakkel ridge	17
3.1	Magnitudes by number of events and average number of phases used for localization by the ISC	50
3.2	Original dataset of events with $m_b \geq 5$	54
3.3	Homogeneous dataset with number of phases used during localization	55
4.1	Quality parameters for exemplary events.	75
4.2	Range of quality for the overall dataset	78
4.3	Minimum and maximum values for RMS and scattervolume	78
4.4	Quality criteria in localization.	79
4.5	Average quality characteristics of for well-located events	81
4.6	Median lengths of error-ellipsoid semi-axis in depth, adjusted for 2D of NonLinLoc Quality 1-3	84
4.7	Characteristics of two exemplary events for mean depth estimation	86
4.8	Mean depth estimation by difference in arrival times of P- and pP-/sP-phases of two exemplary events	87
4.9	Mean depth estimation calculated under the assumption of a misidentification of a pP-phase as the sP-phase	87

LIST OF TABLES

4.10	Comparison of 68% error-ellipse parameters for well-located events by Non-LinLoc and Hyposat	88
4.11	Statistical parameters of station residuals for selected near-stations.	92
5.1	Seismic energy release during three phases in time	98
5.2	b-values of the magnitude-frequency relation, calculated for the three phases in time	99
5.3	Activated area during each phase in time for the well-located dataset.	100
5.4	Three highly correlating events with location, magnitude and first motion.	108
5.5	Characteristics of calculation of focal mechanisms for three crossover-events.	108
5.6	P-wave first motion of all picks for the three crossover-events.	111

List of Figures

1.1	Layered structure of oceanic crust	4
1.2	Heterogeneous structure of oceanic crust	5
1.3	Overview on source mechanisms of earthquakes at mid-ocean ridges	5
1.4	Worldwide mid-ocean ridge system with full spreading rates	6
1.5	Models for melt accretion at oceanic ridges	7
1.6	Idealized axial transection through fast and slow spreading ridges	8
1.7	Dependence of crustal thickness on spreading rate	8
1.8	Differences in axial topography with spreading rate	10
1.9	Relief as a function of spreading rate	11
1.10	Idealized cross section across axis at center- and end of segment at slow spreading ridges	12
1.11	Accretionary modes at ultraslow spreading ridges	13
1.12	Model of 3D-melt migration	14
1.13	Arctic ridge system	15
1.14	Bathymetry and character of dredged samples from Gakkel Ridge by the AMORE expedition	16
1.15	Bathymetric profile along Gakkel ridge	18
1.16	Lithological variation in basaltic percent along Gakkel ridge	18

LIST OF FIGURES

1.17	Magnetic anomalies along Gakkel ridge	19
1.18	Seismic profiles along Gakkel ridge from the AMORE expedition	20
1.19	Positions of ice-floes and supposed vent fields from the AMORE expedition, plotted with earthquake activity.	21
1.20	Hydrothermal signatures at Gakkel ridge from the AMORE expedition	21
1.21	Bathymetric map of the WVZ	22
1.22	Seismic modelling based on refraction profiles within the WVZ	23
1.23	Microearthquake activity recorded by the AMORE expedition in the WVZ	24
1.24	Bathymetric map of the SMZ	25
1.25	Seismic modelling based on refraction profiles within the SMZ	26
1.26	Microearthquake activity recorded by the AMORE expedition in the SMZ	27
1.27	Bathymetric map of the EVZ	28
1.28	Seismic modelling based on refraction profiles within the EVZ	29
1.29	Microearthquake activity recorded by the AMORE expedition in the EVZ	29
1.30	Bathymetry and back-scattering of the 85°E region	30
1.31	Distribution of hypocenters of large events with CMT solutions	31
1.32	Epical migration of 21 large events	32
1.33	Selected epicenters of the 1999 swarm from NEIC with 21 harvard moment tensor solutions	33
1.34	Hyposat relocation and associated source mechanisms	34
1.35	Station residuals for selected near-stations	35
1.36	Bathymetry of the 85°E volcanic area and photographs of deposits	37
1.37	The 85°E volcanic complex with light-scattering anomalies and investi- gated source sites for forward modelling of the seismoacoustic signals	38
2.1	Examples of body wave phases including nomenclature	39

2.2	Snell's law for a spherical earth	40
2.3	Examples for problems which may arise when the PDF has a discontinuous form	46
3.1	Average number of phases used in localization by ISCloc	50
3.2	Localization of the 1999 earthquake swarm by ISC	51
3.3	Baseline NonLinLoc localization of the 1999 earthquake swarm	52
3.4	Distribution of stations for the curtailed datasets	54
3.5	Comparison of the location of $m_b \geq 5.0$ earthquakes using phase datasets truncated in different epicentral distances.	56
3.6	Azimuthal coverage, events with ≤ 30 registered phases.	57
3.7	Azimuthal coverage, events with > 30 registered phases.	58
3.8	Variation in initial number of cells for OCT-tree algorithm, events with ≤ 30 registered phases.	60
3.9	Variation in initial number of cells for OCT-tree search, homogeneous dataset.	61
3.10	Variations of mean RMS in initial cell-number for different datasets	62
3.11	Variations of mean scattervolume in initial cell-number for different datasets	62
3.12	Influence of weighting algorithm on events < 30 phases used in localization.	63
3.13	Influence of weighting algorithm on events with ≥ 30 phases used in localization.	64
3.14	Variations in mean scattervolume through weighting algorithm usage	65
3.15	AK135 global velocity model	66
3.16	Differences between the global AK135 and the local velocity model	67
3.17	Recording seismometers near the 85°N volcanic complex for which the regional velocity model is used	68

LIST OF FIGURES

3.18	Localization with use of the local velocity model for near-stations, ≤ 30 registered phases.	69
3.19	Variations in mean scattervolume through use of an local velocity model	70
3.20	Localization with use of the local velocity model for near-stations, events with $m_b \geq 5$	71
4.1	Overview over final localized dataset, 250 events	74
4.2	Example of a good fit of the error-ellipsoid to the scattercloud	76
4.3	Example of a bad fit of the error-ellipsoid to the scattercloud	77
4.4	Final well-located dataset, 63 events	80
4.5	Hypocentral depth distribution of the 63 well-located events.	84
4.6	Epicenters of the 63 well-located events, colour-coded for their source depth.	85
4.7	43 events of NonLinLoc Quality 1 and corresponding Hyposat epicenters.	89
4.8	Epicenters of quality 1 events for NonLinLoc and Hyposat	90
4.9	Station residuals for selected near-stations	91
4.10	Residual of selected stations	93
5.1	Earthquake swarms on the MAR between 10°N and 60°N in the years 1964-1989 with number of events and duration	96
5.2	Seismicity based on cumulative number of events	97
5.3	Regression for conversion m_b to M_s from reported values	98
5.4	Cumulative seismic moment per julian day	99
5.5	Overview on spatiotemporal development of the 1999 earthquake swarm .	100
5.6	Spatiotemporal development of epicenters for phase 1	102
5.7	Spatiotemporal development of epicenters for phase 2	103
5.8	Spatiotemporal development of epicenters for phase 3	104

5.9	Seismic moment release plotted together with source mechanisms from CMT-catalogue.	105
5.10	Geographical location of focal mechanisms for phase 1.	106
5.11	Geographical location of focal mechanisms for phase 2.	107
5.12	Geographical location of focal mechanisms for phase 3.	107
5.13	Focal mechanism solutions for the event on April, 5 th	109
5.14	Focal mechanism solutions for the event on April, 6 th	109
5.15	Focal mechanism solutions for the event on April, 9 th	110
5.16	Focal mechanisms for CMT-solutions and the three crossover-events, plotted at their epicentral locations.	112

Chapter 0

INTRODUCTION

In 1999 lasting over 7 months, the largest ever earthquake swarm at a mid-ocean ridge was teleseismically registered worldwide. It featured 252 recorded events, including 11 events with a magnitude $m_b > 5.0$ and originated from around a volcanic complex at 85°E at the eastern Gakkel Ridge.

Gakkel Ridge is situated within the Arctic Ocean and spans from eastern Greenland to the continental Siberian shelf. A full spreading rate of 6-14 mm yr⁻¹ classifies this mid-ocean ridge into the ultraslow spreading class, where heat loss by conductive cooling is thought to decrease magma supply and focus magmatism in widely spaced discrete volcanic centres. In this setting, an earthquake swarm of the duration and magnitude as recorded in 1999 ran directly counter to expectations. Within the ultraslow spreading class, spreading processes are still not clearly understood. The unprecedented earthquake swarm of 1999 provided therefore a unique opportunity to study an active spreading process at an ultraslow spreading ridge. A brief summary of the geology of different spreading ridge classes with emphasis on the ultraslow-class, the special geology of Gakkel Ridge, and a summary of previous studies related to the geologic setting at the 85°E volcanic complex form **CHAPTER 1**.

Due to the remote setting of Gakkel Ridge, a total lack of local or regional seismic stations makes localization of earthquakes especially challenging. First analyses of the 1999 earthquake swarm were based on preliminary datasets and automatic localization procedures. It therefore seemed indicated to relocalize the earthquake swarm using the meanwhile available ISC reviewed dataset. A reliable location of the 1999 earthquake swarm is crucially important for any kind of further investigation, therefore the main emphasis of the following work lies in relocalization and evaluation of the relocalization quality.

For relocation I used the probabilistic nonlinear location procedure NonLinLoc in con-

trast to a relocation which was done in 2009 with the linearized least squares algorithm Hyposat. Within **CHAPTER 2** I summarize the basics of earthquake localization, including an introduction to the conventional least-squares algorithm Hyposat, and the theory of probabilistic earthquake localization as incorporated in NonLinLoc.

Teleseismic localization is heavily dependent on the spatial distribution of recording stations and the number of registered phases. Therefore I tested extensively the influence of velocity model, station coverage in epicentral- and azimuthal coverage and the influence of station clusters on the localization result. **CHAPTER 3** includes the testing of above mentioned parameters. I found a severe dependence of the location on station coverage and a stable result for good constrained events with regard to velocity model and station weighting.

The final relocation was done by using the AK135 velocity model, combined with a regional velocity model for recording stations with epicentral distance $< 30^\circ$. The dataset was reviewed with regard to the quality of the location and reduced to 63 well located events whose epicenter locations are largely independent of the above tested parameters. The new locations of the epicenters show a clustering of events in the central rift valley and the southern rift flank, with the 68% error in error-ellipse semi-major axes of the new localization in the order of 15 km for the best events. Hypocentral depths as given by NonLinLoc are not reliable due to the lack of regional recording stations. A first order estimate of hypocentral depths for two major events calculated by traveltimes-differences between pP- and pS-phases comes out at about 15 km depth.

An epicentral comparison including error-ellipses of NonLinLoc versus Hyposat fails to show a match between the two datasets. Finally, an evaluation of mean station residuals at $< 30^\circ$ epicentral distance results in systematic traveltimes delays towards the East along Gakkel Ridge, indicating lower seismic velocities in this direction than the reference model. **CHAPTER 4** incorporates the final relocation, its uncertainties including a hypocentral depth evaluation, the comparison of the probabilistic relocation to the least-squares solution of 2009, and the evaluation of station residuals.

CHAPTER 5 presents a geological analysis of the earthquake swarm in time and space. The spatiotemporal analysis of the relocated dataset shows three temporal phases: In the first phase up to the 1st of February a breaking of crust activates the area. The second phase from February, 1st up to April, 6th indicates seismic release of energy through heterogeneous crust reacting to magmatic pulses. A clear volcanic event is absent in the data. Three events with highly correlating waveforms within the second week of April which were thought to indicate a volcanic eruption could be explained by strike-slip mechanisms. At around April, 6th, the third phase in the temporal evolution of the swarm characterizes probably an adjustment of the stress field to the new regime.

This diploma thesis focusses mainly on the localization and the evaluation of the probabilistic localization algorithm and less on geological interpretation.

Chapter 1

GEOLOGIC SETTING - Mid-Ocean Ridges

The ocean floor throughout the world is covered by a system of ridges resembling mountain chains, which stretches out more than 60,000 km. Within this network, mid-ocean ridges mark the constructive plate boundaries where passive upwelling of asthenospheric mantle material through decompression takes place. Freezing attaches melt to the base of the lithosphere, to be transported away by the spreading plates. Alternatively melt concentrates into channels while flowing along the impermeable barrier of the cooled off crust. It is directed to the ridge axis to approach the surface through faults and generates new oceanic crust at the ridge axis. Transform faults break up the ridge in intermittent spans.

Tectonic activity and magmatic accretion accompany plate spreading. Often this process of brittle deformation and ascending magma is accompanied by earthquakes which in turn reflect the active spreading process. Generally earthquakes are generated when brittle deformation takes place and the stresses within the matrix exceed the breaking point which depends on rock composition. Within a ductile environment breakage is impossible. Hence the hypocenter of earthquakes tells us that the matrix at this point is still brittle. Knowledge of the composition of the oceanic crustal matrix is gained by laboratory measurements of dredged rock samples from the ocean floor and careful appraisal of seismic measurements in this light.

The idealized layered structure of mid-ocean ridges within a hot thermal environment (Fig. 1.1) applies mainly to the broad spectrum of fast spreading ridges and forms through successive discharge of basaltic material near or at the top of the seafloor through dykes.

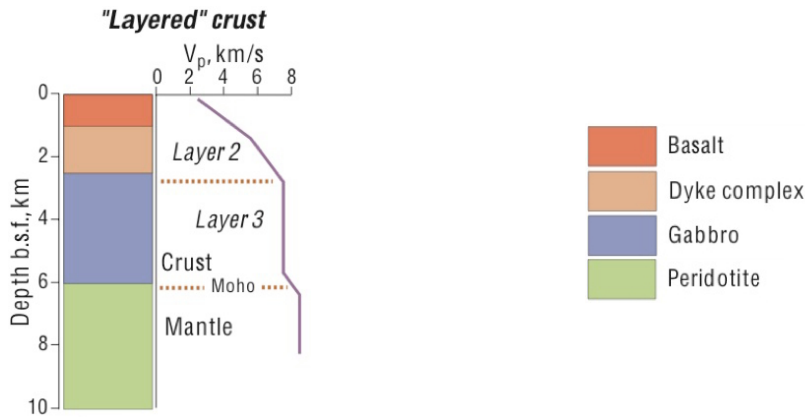


Figure 1.1: Layered structure of oceanic crust (*Mevel, 2003*)

- Layer 1: Sedimentary Layer
Sediments, seismic p-wave velocity (v_p) increases with consolidation. The sedimentary layer is not shown in Fig. 1.1. ($v_p = 1.9\text{-}2.7 \text{ km s}^{-1}$)
- Layer 2: Volcanic Layer (basaltic layer)
At the top of layer 2 we find extrusive basaltic pillow lavas in varying stages of metamorphism, below are sheeted dykes. v_p increases rapidly with depth.
- Layer 3: Oceanic Layer
The oceanic layer consists of gabbros with possible significant serpentinization as a result of increasing depth and temperature. The p-wave velocities are still increasing but with a very much smaller gradient. At a small axial zone ($\approx 20 \text{ km}$) of mid-ocean ridges this layer can have a reduced velocity or even be completely absent. The seismic Mohorovicic-Discontinuity (Moho) at the base of layer 3 defines the change from oceanic crust to upper mantle material.

Within a cold thermal environment the crustal structure of mid-ocean ridges (Fig. 1.2) is heterogeneous and revolves around the absence of significant heat flow. The basaltic layer is often completely absent, serpentinized peridotites are found at the topography instead with lesser serpentinization at greater depths. Within this matrix, gabbroic inclusions are found.

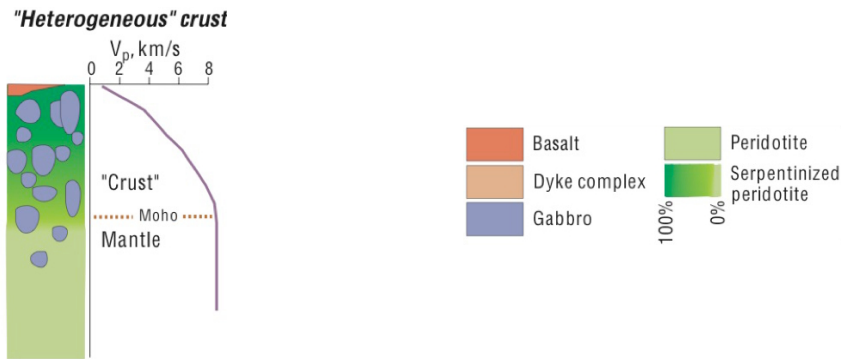


Figure 1.2: Heterogeneous structure of oceanic crust (*Mevel, 2003*)

Seismicity at mid-ocean ridges is mostly confined to shallow events with hypocentral depth of 1-6 km and small magnitudes ($m_b \leq 4$). It seems also that the focal depth decreases with increasing spreading rate (*Bergman and Solomon, 1990*). Earthquakes with large magnitudes are uncommon as small-scale faulting and breakage through magma movement generally release little energy. Therefore earthquakes at mid-ocean ridges are difficult to detect at teleseismic distances.

A double-couple shearing source with normal faulting is predominantly found at the constructive segments, strike-slip is found at transform faults (Fig. 1.3). Comparative studies of mid-ocean ridges indicate that earthquakes originating at the ridge axis are mostly pure normal double-couple, the releasing faults dipping at 45° with strike parallel to the local trend of the ridge axis.

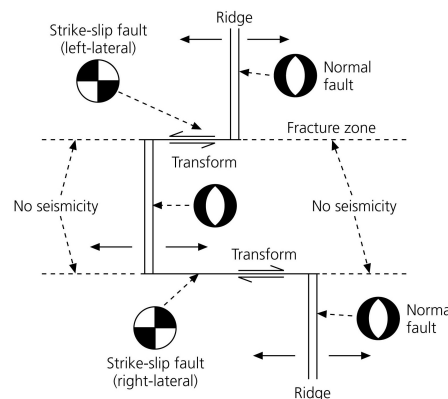


Figure 1.3: Source mechanisms of earthquakes at mid-ocean ridges (*Stein and Wysession, 2003*)

Summary: Earthquakes generated at mid-ocean ridges are mostly caused by magma movement and small-scale faulting. Hence they are difficult to detect at teleseismic distances.

1.1 Spreading Rate and Thermal Structure

If we take a closer look upon the differences within the world-spanning mid-ocean ridge system (Fig. 1.4) we find that the worldwide system of mid-ocean ridges has widely varying spreading rates which are classified into fast (more than 80 mm yr^{-1}), intermediate ($40\text{-}80 \text{ mm yr}^{-1}$), and slow (below 40 mm yr^{-1}) spreading rates. Gakkel Ridge displays the slowest spreading rate with 6 mm yr^{-1} , and the Eastern Pacific Rise the fastest with up to 185 mm yr^{-1} . Throughout this text, spreading velocities are given as full plate separation velocity in mm yr^{-1} except when otherwise indicated.

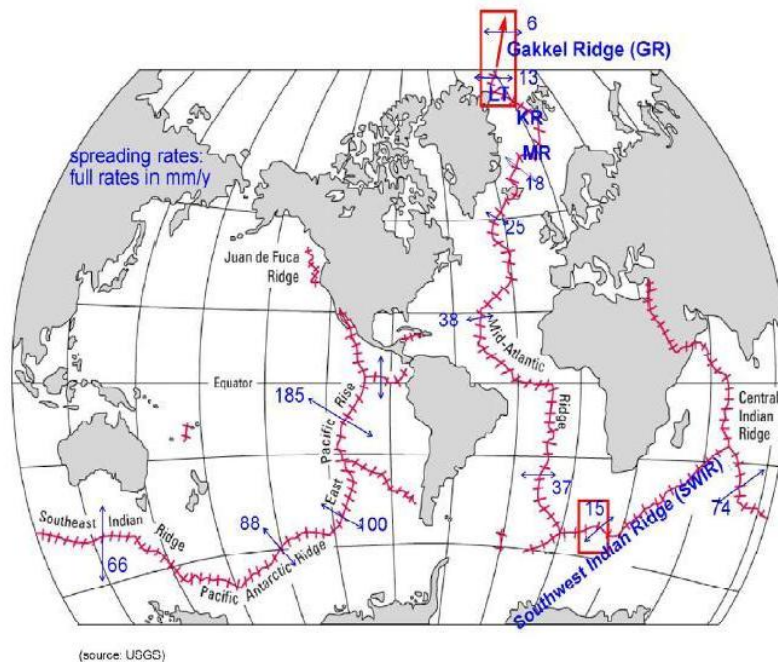


Figure 1.4: Worldwide mid-ocean ridge system with full spreading rates, after *USGS* (1999)

Spreading velocity control the amount of melt supply and the mode of crustal accretion. The thermal structure of the oceanic mantle in turn controls the size and geometry of magma chambers. Samples of mid-ocean ridge basalts (MORB) and depleted mantle material (DMM), dredged from the topography, allow to determine the degree of partial melting through the content of incompatible elements.

Fertile upper mantle material melts when it is brought up adiabatically to a depth of about 40 km. From here on it rises within sill lenses or dykes, losing a portion of its incompatible elements. Eventually the now depleted matrix makes its way to the surface to be dredged and sampled. The Gabbro Glacier Model (*Henstock et al.*, 1992; *Kelemen et al.*, 1997) (Fig. 1.5(a)) and the Sheeted Sill Model (*Boudier et al.*, 1996; *Quick and Denlinger*, 1993) (Fig. 1.5(b)) both describe the pertinent processes. A combination of

both models seems to fit best to different spreading rates (*MacLennan et al., 2004*).

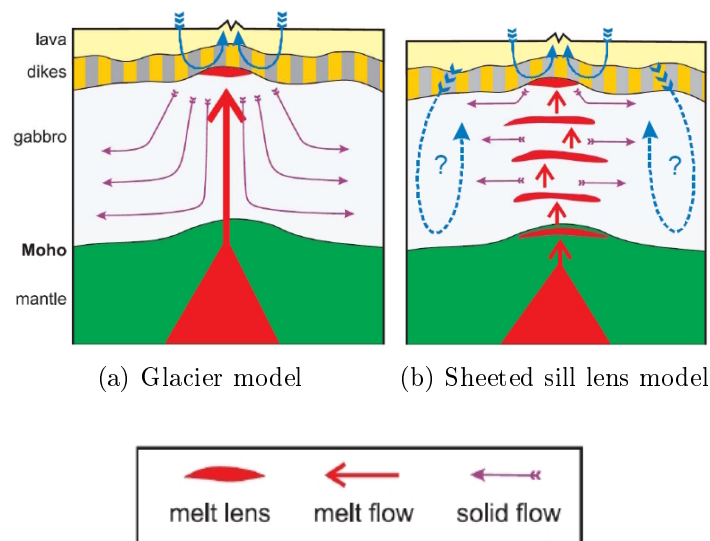


Figure 1.5: Glacier model (Fig. 1.5(a)) and the model for sill lenses (Fig. 1.5(b)) for melt ascent at oceanic ridges. The blue dotted arrows designate possible hydrothermal flow. Redrawn from *Korenaga and Kelemen (1998)*.

Faster moving plates need a larger magma supply at the axis which sits closer to the surface than the slower spreading ones (Fig. 1.6(a)). Therefore we find high partial melting which correlates with a large melt production for a long time and hence a low concentration of incompatible elements in dredged samples of MORB. Axial magma chambers (AMC) are indicated by a low velocity zone extending to the base of the crust, the lateral extension varying dependent on spreading rate. If the ridge in question spreads very slowly as Gakkel Ridge does, loss of heat by thermal conduction becomes critical. This means that melt production is severely limited and very low partial melting occurs (*Bown and White, 1994*). Eventually, deep rooted detachment faults form, allowing seawater to penetrate the lithosphere (Fig. 1.6(b)). AMC, if at all present, are very limited in extension.

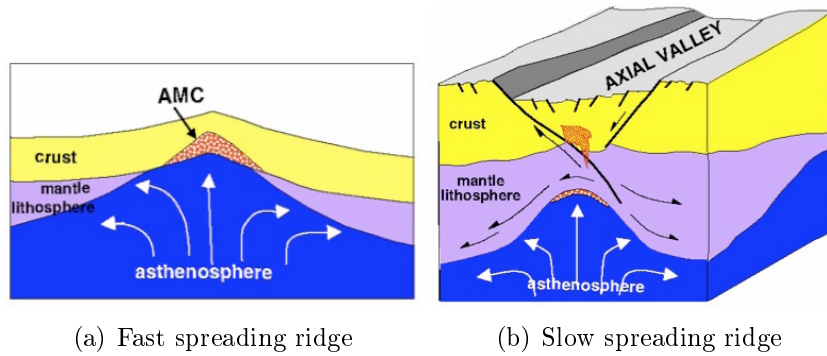


Figure 1.6: Comparison of an axial transection through fast- (Fig. 1.6(a)) and slow spreading ridges (Fig. 1.6(b)), *Mevel 2008 (pers. comm.)*

Crustal thickness also depends on the thermal structure beneath mid-ocean ridges. *Bown and White (1994)* argue for a dependence of crustal thickness on spreading rate (Fig. 1.7) found in refraction profiles modelled with synthetic seismograms and augmented by inversions for rare earth elements. It shows clearly that as the spreading rate decreases below 20 mm yr^{-1} , crustal thickness drops off abruptly.

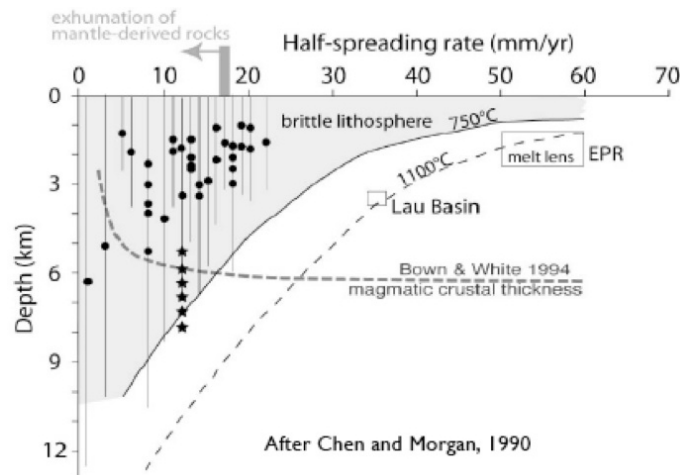


Figure 1.7: Dependence of crustal thickness on spreading rate, modified from *Chen and Morgan (1990)* by *Bown and White (1994)*

In active tectonic areas like mid-ocean ridges brittle deformation gives rise to numerous faults through which water can penetrate deep into the crust. Ocean water at great depths has about 4°C , which almost instantly reduces the temperature of the solid upper crustal segments and cools effectively. Eventually it heats up and rises upward again, forming hydrothermal vents which channel the hot acid water (400°C at ocean floor pressure, pH 2) back into the ocean. The spacing of hydrothermal vents is therefore an indicator of the thermal state.

Summary: Thermal structure beneath mid-ocean ridges forms a linked system with spreading rate. Both determine the thickness of crust, composition of upper mantle material and therefore seismic velocities. The concentration of incompatible elements in MORB's and DMM's reflects partial melting, indicating the abundance of magma supply and pointing to stability and depth of magma chambers. The frequency of hydrothermal venting sites also indicate the thermal state beneath mid-ocean ridges.

1.2 Spreading Rate and Axial Topography

Axial topography depends on the ability of the viscous lithosphere to support the stresses of ductile extension. It is therefore critically dependent on thermal environment. As the distance to the ridge axis increases the lithospheric plate gets more heavy and decreases in volume due to cooling. Sediments bury the rugged topography including numerous rifts and faults, the ocean floor levels out. These are then called the abyssal plains.

We observe systematic differences in axial topography and relief (Fig. 1.8) as a function of spreading rate. Tectonic and magmatic activity is mostly confined within the axial zone, (1) and (2) in Fig. 1.8, whose extension varies up to 20 km with active magmatism occurring within the neovolcanic zone (*Macdonald, 1982*), in an area about 1-2 km wide. The appearance of fast spreading ridges which possess an axial rise and slow spreading ridges which form an axial valley obviously differ 1.8. Faster spreading ridges are characterized by an elevation of the axis with basaltic features found within the axial zone as evidence for active magmatism of an often continuous magmatic supply beneath. Generally speaking, slower spreading ridges have rougher flanks which are to some extent heavily fissured and the rift valley is made up of peridotites as alkaline upper mantle material. As Gakkel Ridge is the world slowest spreading ridge I will focus here on the details of slow spreading ridges.

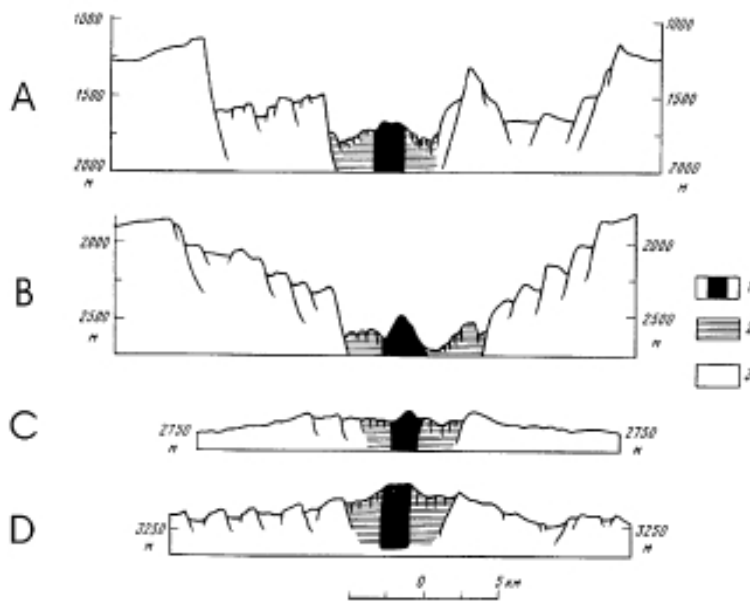


Figure 1.8: Differences in axial topography with spreading rate (*Rundquist and Sobolev, 2002*).
 (1) Extrusive Zone, (2) Axial Valley, (3) Flanking Zone
 (A) Red Sea Ridge 18° N, $v = 1.5 \text{ cm yr}^{-1}$, (B) Mid-Atlantic Ridge 37° N, $v = 2.5 \text{ cm yr}^{-1}$, (C) East Pacific Rise 21° N, $v = 6 \text{ cm yr}^{-1}$, (D) East Pacific Rise 3° S, $v = 15 \text{ cm yr}^{-1}$

1.2.1 Slow Spreading Ridges

Slow spreading ridges have a highly variable appearance and generally speaking, the slower it spreads the more pronounced and deep its median valley, and the more rugged its appearance (Fig. 1.9). The axial rift valley is up to 40 km wide and is flanked to both sides by numerous high rising normal faulting structures (*Rundquist and Sobolev, 2002*). A continuous magma supply is absent under slow-spreading ridges (*Solomon and Toomey, 1992*).

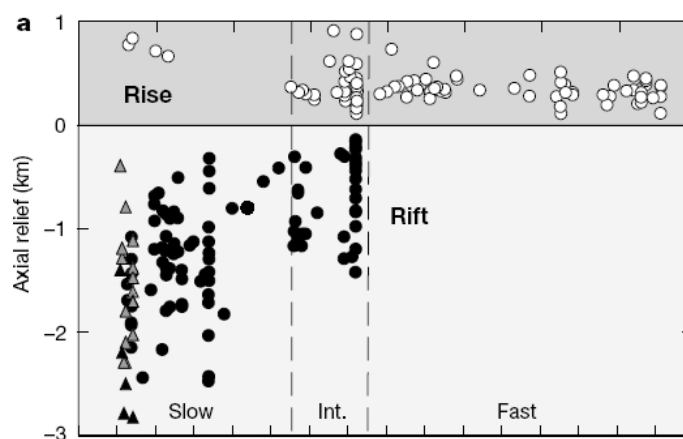


Figure 1.9: Relief as a function of spreading rate (*Dick et al., 2003*)

The overall ridge is segregated into segments, with each segment thermally/magmatically controlled. Sometimes segments at slow spreading ridges are separated by non-transform offsets. Transient volcanic activity takes place within the rift valley at the center of segments, sometimes forming axial volcanic ridges (AVR) which consist of several volcanoes linearly strung together.

At the segment centers (Fig. 1.10(a)) we find that the newly formed crust is cut by numerous fault blocks. These faults scarps form by brittle deformation within the zone of active deformation, possibly constraining the area of magmatism within the axial valley (*Rundquist and Sobolev, 2002*). At the magmatic center of the segment the ridge axis is shallowest (within a hot thermal environment). Exceptions occur when the thermal structure beneath the ridge deviates (e.g. plumes in the vicinity heat up the environment as in the case of the slow spreading Reykjanes Ridge near Iceland - it does not have an axial valley at all.) As the distance to the magmatic center of the individual ridge segment increases and the large number of small faults near the segment center decreases, they are replaced by fewer large faults which are spaced wider apart.

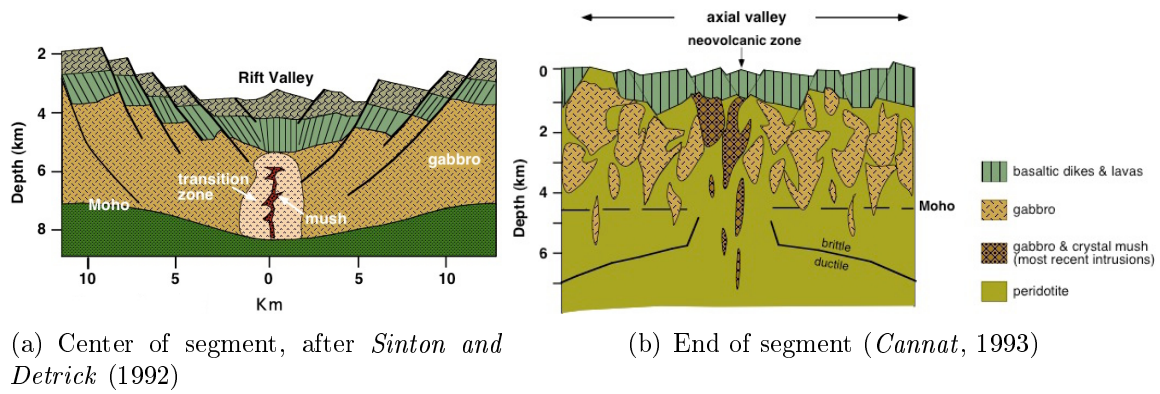


Figure 1.10: Idealized cross Section across axis at center- and end of segment at slow spreading ridges.

The segment ends (Fig. 1.10(b)) are at a bathymetric low within a cold thermal environment. Exposures are very heterogeneous and consist mainly of rocks of deeper origin (serpentinized peridotites, gabbros), emplaced there by detachment faults. Evidence for trapped melt within the lithospheric mantle (mehl!) is also found. Not surprisingly segment ends sometimes host hydrothermal fields.

Summary: Slow spreading ridges are divided into segments which are tectonically and magmatically controlled. Magmatic accretion occurs only sporadically and its phases are separated by long intervals of tectonical extension. Generally, axial topography is controlled by spreading rate, magmatic supply as it accumulates under the ridge, tectonic strain and the rate of hydrothermal circulation. A fault dominated appearance builds up with deep rift valleys and highly variable relief. Small volcanic seamounts are the dominating feature in building crust. Segment centers are at a bathymetric high with episodic volcanoes at the axial center, segment ends expose heterogeneous rocks.

1.2.2 Ultraslow Spreading Ridges

Within the slow spreading ridges the wide range of differing morphological features allows another distinction, namely the ultraslow spreading class. *Dick et al.* (2003) adopted this classification for the finding of *Bown and White* (1994) that at a spreading rate lower than 12 mm yr^{-1} morphology, crustal structure, magmatic and tectonic pattern change abruptly. A spreading rate of 12 mm yr^{-1} seems a threshold step (Fig. 1.9) below which changes in crustal thickness through mantle composition and thermal structure critically affect crustal structure (*Michael et al.*, 2003; *Goldstein et al.*, 2008). Between a spreading rate of 12 and 20 mm yr^{-1} characteristics of the spreading process vary between the slow and ultraslow class over long sections. Gakkel Ridge east of 3°E qualifies as an ultraslow-spreading ridge.

Ultraslow spreading ridges present alternating amagmatic (Fig. 1.11 a.) and magmatic accretionary segments (Fig. 1.11 b.) in the complete absence of transform faults. Volcanism is discontinuous.

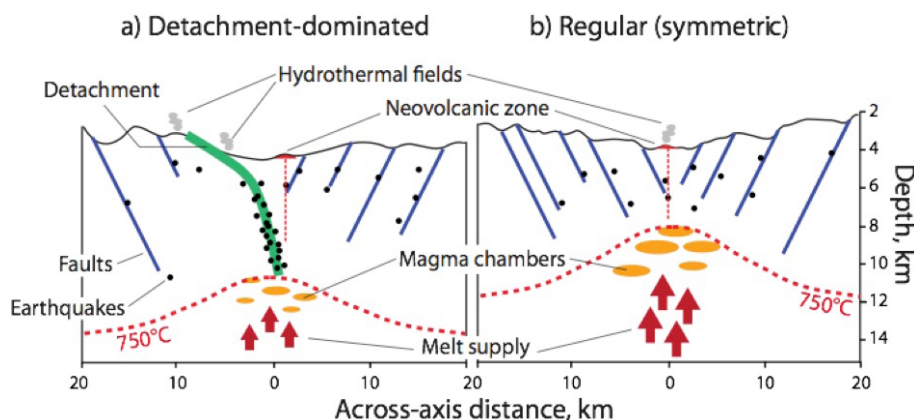


Figure 1.11: Accretionary modes at ultraslow spreading ridges (*Escartin et al.*, 2008).

The magmatic segments (Fig. 1.11 b.) form in a regular accretionary environment. The rift valley walls consist of blocks with normal boundary faults and small non-transform faults. In the segment centers we find highly focused volcanism as saddle points of the bathymetry with circular mantle-bouguer-anomalies, suggesting more melt and/or mantle flow beneath. These volcanic centers are even more prominent than at slow-spreading ridges and the sole source for magmatic accretion.

As the name suggests, amagmatic segments (Fig. 1.11 a.) absorb the stresses of plate movement not through magmatic accretion but through varying symmetric/asymmetric spreading at deeply rooted detachment faults within a shallow axial trough. The primary mode of accretion is an uplifting of mantle horst blocks which in turn form the trough walls. Modelling tells of a thick lithosphere and highly localized deformation (*Lavier et al.*, 1999) with only a thin layer of basalt if at all present, overlying exposed mantle

rocks and virtually no seismic layer 3 (*Jokat et al.*, 2003). Scattered volcanoes tend to form at faults on the rift valley walls. Hydrothermal fields are found both at magmatic and amagmatic segments.

Magma focusses toward the center of segments through 3D-melt channels upwelling (Fig. 1.12), driven by uniform convection. Dikes, lower crustal flow, and/or tectonic events then redistribute the melt throughout each segment.

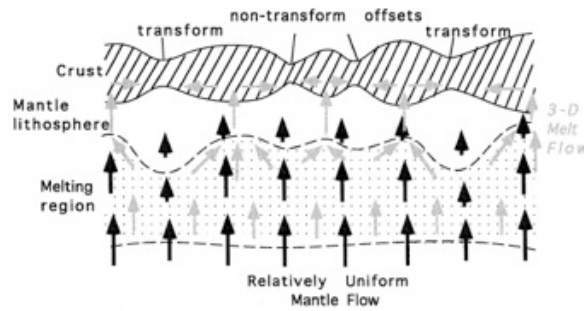


Figure 1.12: Model of 3D-melt migration (*Magde et al.*, 1997). Mantle flow is indicated by black arrows while melt migration is indicated by grey arrows.

The driving factors for topographic appearance of ultraslow-spreading ridges are still under investigation. Spreading rate by itself seems to play an important role as crustal thickness decreases from 4.9 km at 84°W within the magmatic western volcanic zone at Gakkel Ridge to 2.5 km at 83.3°W which lies just on the other side of the boundary between slow- and ultraslow spreading characteristics in the amagmatic sparsely magmatic zone at Gakkel Ridge (*Jokat and Schmidt-Aursch*, 2007). Contrary to this data from refraction seismics *Cochran* (2008) noted at the Southwest Indian Ridge (SWIR) slow characteristics at spreading rates below 11 mm yr⁻¹ and segments with spreading rates higher than 13mm yr⁻¹ to have distinct amagmatic characteristics. Therefore spreading rate cannot be the dominating factor in tectonic appearance.

Goldstein et al. (2008) postulate that changes in chemical composition of the mantle may have a major effect for the ultraslow spreading class. He found evidence that an isotopic boundary exists between 13°E - 16°E Gakkel Ridge, changing the character from magmatic to profoundly amagmatic. A similar chemical boundary exists between the Southeast Indian Ridge east of the Australian-Antarctic discordance with shallow crustal depth and a well developed axial high (magmatic accretion) and the amagmatic Southeast Indian Ridge to the west.

Summary: Ultraslow spreading ridges consist of alternating magmatic and amagmatic segments. Volcanism is concentrated at the segment centers in magmatic segments (regular accretionary environment), within amagmatic segments (detachment oriented) volcanoes are situated at the abundant faulting at the valley walls. Factors influencing ridge appearance are spreading rate and mantle chemism.

section Geology of Gakkel Ridge The Arctic ridge system (Fig. 1.13) begins at its southern end with Knipovich ridge and runs through the Molloy fracture zone to Lena trough at 83°N 6°W northwest of Svalbard. From there it turns into the 1,800 km long Gakkel ridge that connects Lena trough with Laptev shelf, the continental shelf of Siberia. Gakkel

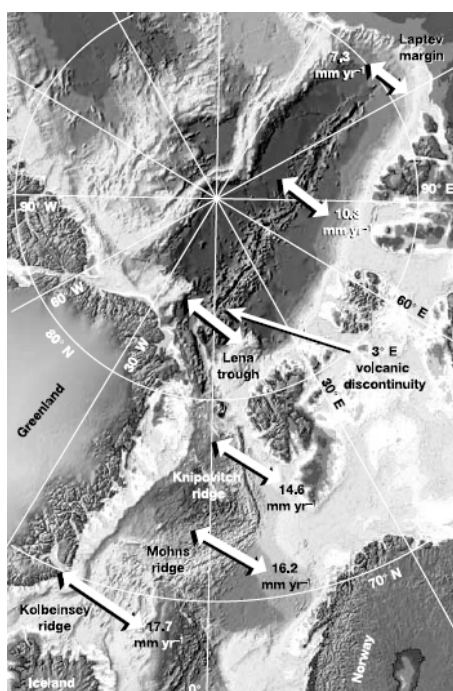


Figure 1.13: Arctic ridge system, spreading rates from NUVEL1 (DeMets *et al.*, 1994) with IBCAO bathymetry (Macnab and Jakobsson, 2003). Fig. from Dick *et al.* (2003)

Ridge has no transform offsets but otherwise an extremely varied appearance. Based on morphology and magmatic character it was divided into three distinct ridge segments with differing characteristics (Michael *et al.*, 2003) (Tbl. 1.1):

- The Western Volcanic Zone (WVZ) (Fig. 1.14) shows volcanic rises along axis, with a bathymetric relief comparable to the Mid-Atlantic-Ridge (MAR). It shows large differences in relief of up to 2 km. The spreading rate is about 13.7 mm yr^{-1} at the intersection of Gakkel ridge and Lena trough.
- The Sparsely Magmatic Zone (SMZ) (Fig. 1.14) is generally amagmatic in character and has a deeper and narrower rift valley floor in between small volcanic centers with a subsequently decreasing spreading rate.
- The Eastern Volcanic Zone (EVZ) (Fig. 1.14) is characterised by highly focused volcanism in prominent volcanic centers. It's spreading rate decreases further to about 7.0 mm yr^{-1} at the far eastern end.

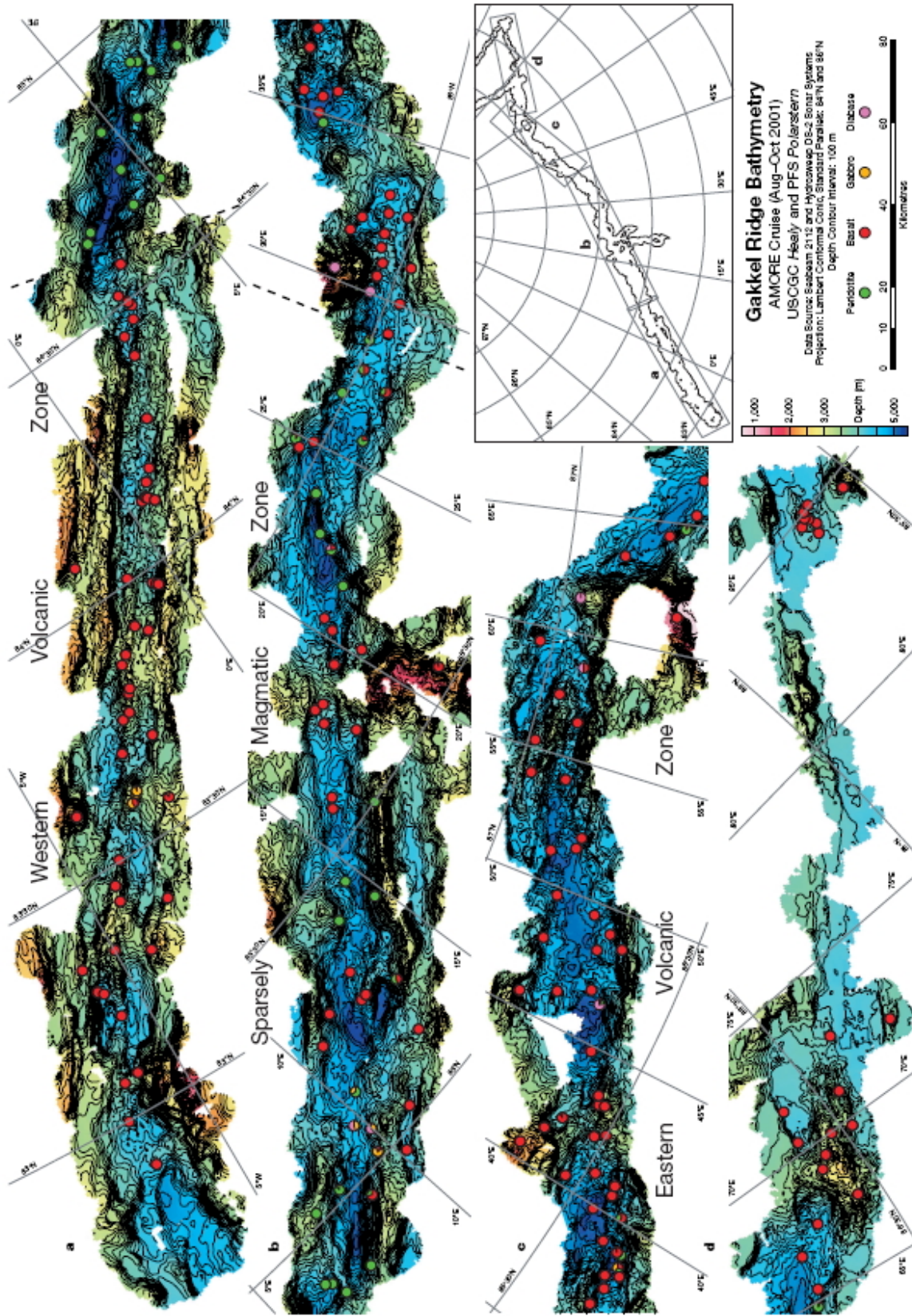


Figure 1.14: Bathymetry and character of dredged samples from Gakkel Ridge by the AMORE expedition (*Michael et al., 2003*). Green dots are peridotites, red dots designate basalts, orange ones are gabbros and violet shows dredged diabase.

Segment	Spreading Rate	Character	Extension
Western Volcanic Zone	13.0 mm yr ⁻¹	Magmatic	83°N 6°W - 84.3°N 3°E
Sparsely Magmatic Zone	- 12.0 mm yr ⁻¹	Amagmatic	84.3°N 3°E - 86°N 29°E
Eastern Volcanic Zone	- 7.0 mm yr ⁻¹	Magmatic	86°N 29°E - 78.5°N, 128°E

Table 1.1: Segments of Gakkel ridge, spreading rates from NUVEL1 (*DeMets et al.*, 1994).

At its western end Gakkel ridge opens with rates which are comparable with other slow-spreading mid-ocean ridges (e.g. MAR). However, the spreading continuously decreases eastwards to values below 7.0 mm yr⁻¹ near the Siberian continental shelf. This makes Gakkel ridge unique for studying the spreading rate dependence of accretion mechanisms.

Over the last 10 years, three expeditions have made an effort to investigate Gakkel ridge:

Year	Name of expedition and conducted experiments
1999	Science Ice Exercises (SCICEX) - Bathymetry - Sidescan Sonar
2001	Arctic Mid-Ocean Ridge Expedition (AMORE) - Bathymetry - Hydrothermal exploration - Dredging - Aeromagnetic measurements - Seismic Refraction - Seismology
2007	Arctic Gakkel Vents Expedition (AGAVE) - Bathymetry with multibeam sonar - Digital seafloor imagery (CAMPER) - Sampling - Hydrothermal exploration - Seismology

Table 1.2: Expeditions visiting Gakkel ridge

Bathymetric data were collected by the SCICEX expedition (*Edwards et al.*, 2001; *Cochran et al.*, 2003). In 2001 the AMORE expedition made the first effort in sampling continuously along the length of Gakkel ridge up to 87°E for bathymetric (*Michael et al.*, 2003) (Fig. 1.15), lithological (*Michael et al.*, 2003) (Fig. 1.16), aeromagnetic (*Jokat and Schmidt-Aursch*, 2007) (Fig. 1.17), refraction seismic (*Jokat and Schmidt-Aursch*, 2007) (Fig. 1.18), seismological (*Schlindwein et al.*, 2007) (Fig. 1.19) and hydrothermal (*Baker et al.*, 2004) (Fig. 1.20) data which are briefly presented in the following figures and discussed in more detail in the description of the individual segments. The AGAVE expedition returned in 2007 to the 85°E volcanic center (*Sohn et al.*, 2008).

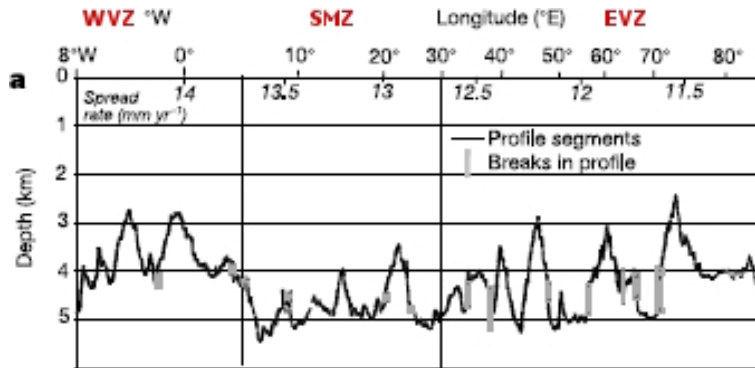


Figure 1.15: Bathymetric profile along Gakkel ridge (*Michael et al.*, 2003).

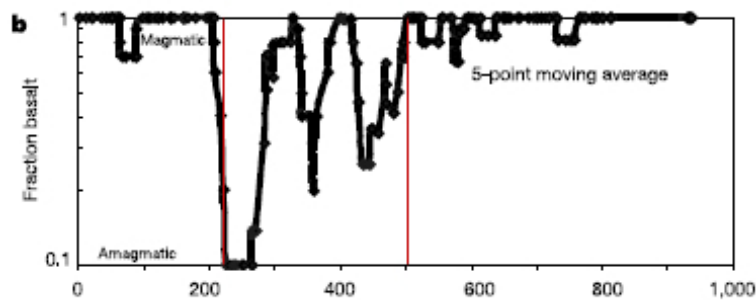


Figure 1.16: Lithological variation in basaltic percent along Gakkel ridge [km], calculated as average of each dredge with a boxcar average for each 5 dredges (*Michael et al.*, 2003).

The total field magnetic anomalies (Fig. 1.17) were measured during helicopter flights by the AMORE expedition. Minimal magnetic anomalies are found at locations where peridotites were dredged. The largest magnetic anomalies were recorded near volcanic ridges which extend off-axis as bathymetric highs. Thus it may be possible to use the strength of the magnetic anomaly as indicator for the thickness of the basaltic layer (*Jokat and Schmidt-Aursch, 2007*).

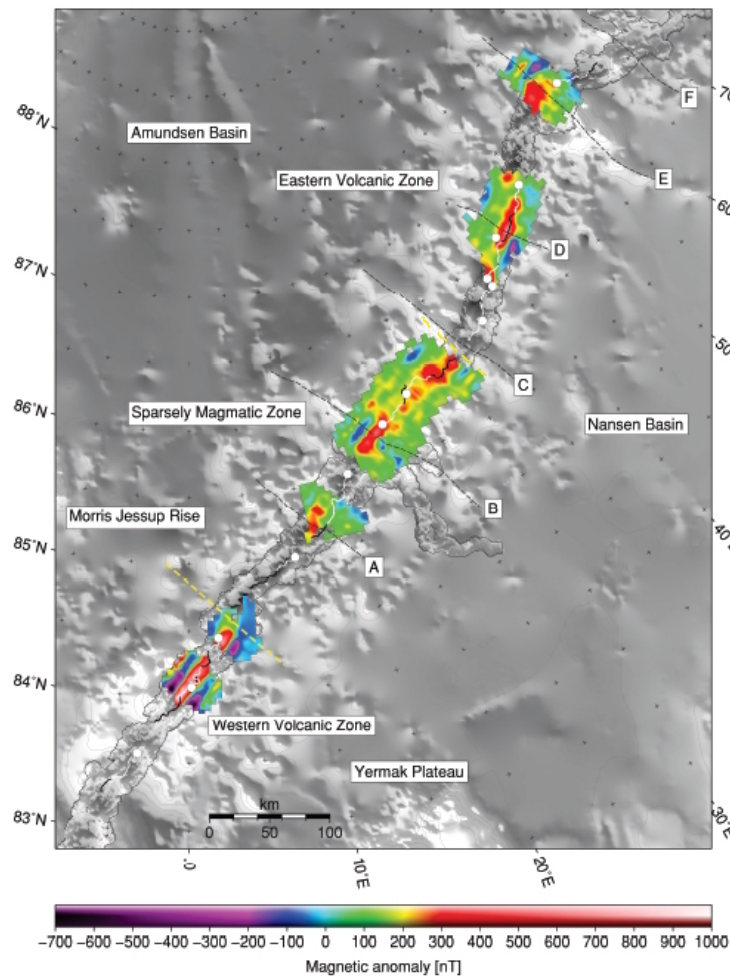


Figure 1.17: Magnetic anomalies along Gakkel ridge, bathymetry (grey) is plotted below (*Jokat and Schmidt-Aursch, 2007*). Yellow dashed lines indicate change of segments WVZ/SMZ and SMZ/EVZ. White dots are seismic stations, dark grey dashed lines show axial ridges.

This was confirmed by refraction seismic data (Fig. 1.18) acquired during AMORE. *Jokat and Schmidt-Aursch (2007)* could not confirm a simple decrease of crustal thickness with decreasing spreading rate but found a strong dependency of crustal thickness on the bathymetric character and lithology of the sampled area.

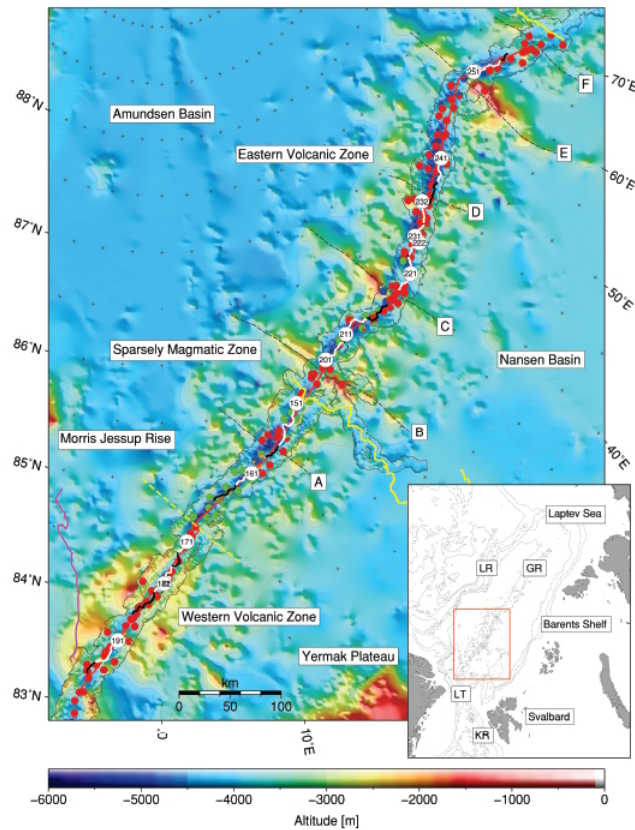


Figure 1.18: Seismic profiles along Gakkel ridge from the AMORE expedition. White circles give seismic recording stations, white/black lines give refraction profiles with numbers. Dashed yellow lines are transition from WVZ/SMZ and SMZ/EVZ. The solid yellow line shows reflection profile within the basin. Coloured dots indicate dredge content (red: Basalt, green: Peridotite, orange: Gabbro, blue: Others). Black dashed lines indicate axial ridges (*Jokat and Schmidt-Aursch, 2007*).

The microearthquake activity recorded by seismological arrays floating on ice-floes with a recording time of 5-11 days during the AMORE expedition (Fig. 1.19) proved that Gakkel ridge is tectonically active (*Schlundwein et al., 2007*). The arrays detected events interpreted as having a tectonic origin on all three sites as well as events with supposed magmatic origin at the sites within the WVZ (GAK0) and EVZ (GAK2). The higher number of events on the northern rift flanks than at the southern flanks of the rift valley at the three sites points to asymmetrical spreading.

Edmonds et al. (2003) and *Baker et al. (2004)* analysed water column data collected by AMORE for signs of hydrothermal plumes. The proposed sites are situated mostly at volcanic centers (Fig. 1.20). Despite its slow spreading rates and a theoretically postulated lack of constant heat sources numerous plumes were detected.

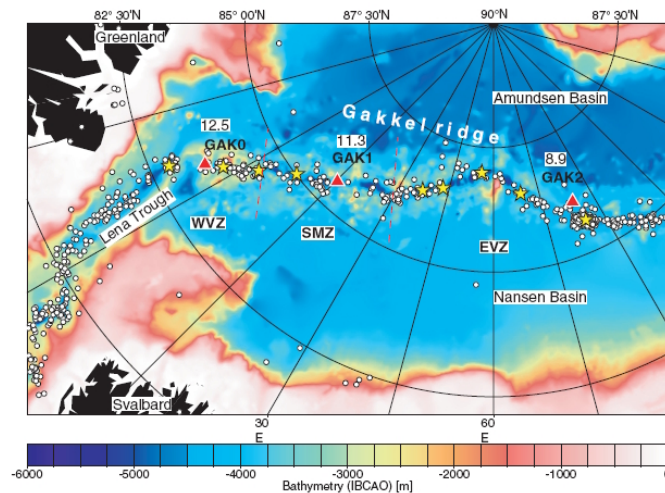


Figure 1.19: Position of the ice-floes (red triangles) which recorded microearthquake activity for the AMORE expedition (*Schlundwein et al., 2007*). Stars indicate supposed vent fields (*Edmonds et al., 2003*), white circles are earthquake epicenters (*Engen and Eldholm, 2003*).

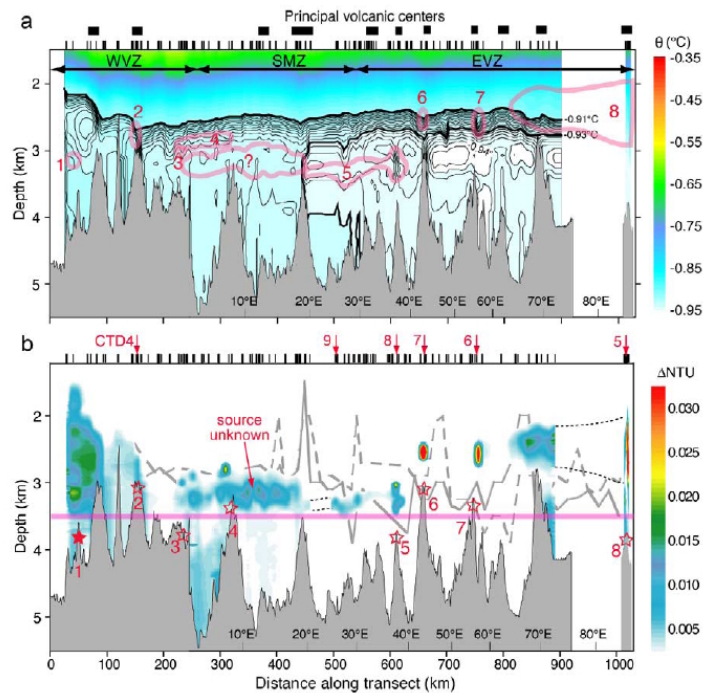


Figure 1.20: Hydrothermal signatures at Gakkel ridge (*Baker et al., 2004*). The top image shows hydrothermal temperature anomalies, the bottom image anomalies in light scattering (NTU). Red stars propose active sites, filled stars indicate confirmed vents. Black bars at top of image show collection of data by miniature autonomous plume recorders (MAPR).

Western Volcanic Zone (83°N 7°W - 84.3°N 3°E)

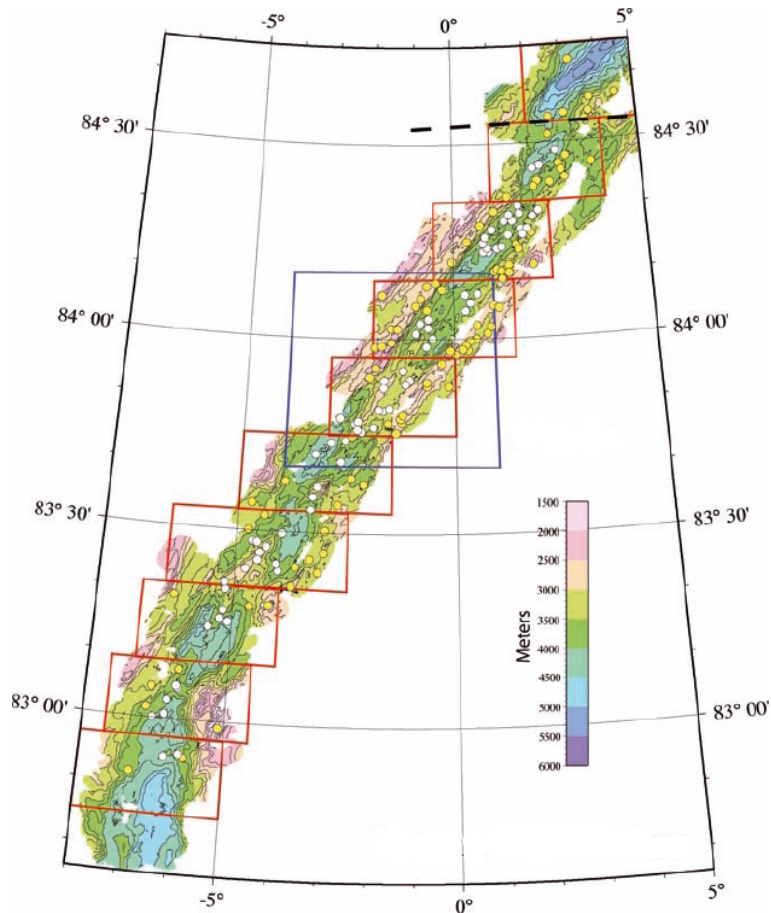


Figure 1.21: Bathymetric map of the WVZ (Cochran, 2008). White and yellow circles are closed concentric structures, interpreted as seamounts.

The bathymetric character of the Western Volcanic Zone (Fig. 1.21) is similar to the MAR (Fig. 1.15) even if the spreading rate is with 12.8 mm yr^{-1} only about half of its southwesterly cousin (Michael *et al.*, 2003). Despite the comparable topographic character to the MAR, Cochran (2008) found that concentric closed structures at the rift valley floor of the WVZ are only about half as frequent as at the MAR. Additionally the height and volume of the seamounts are significantly lower, therefore implying a greatly reduced melt supply.

At the ridge axis, five well defined and more or less elongated volcanic centers exist, the biggest at $4^{\circ}45'W$ and $1^{\circ}45'W$. In addition we find some bathymetric highs within the interjacent shallow valley floor (Fig. 1.15). This suggests an extensive magmatic supply along-axis and partial focusing of melt to the center of segments. Dredging by the AMORE expedition resulted in abundant glassy pillow basalts in the entire area which might point to a redistribution of magma along-axis by dykes.

Near the bathymetric highs the rift valley narrows slightly. The absence of ridge offsets points to lithospheric tectonics as driving factor of magmatic segmentation (*Michael et al.*, 2003). High angle normal faults are found at the rift valley walls, another feature which is found also at slow-spreading ridges.

Three unreversed seismic refraction lines (Fig. 1.18) yielded crustal thicknesses varying from 2.2-3.5 km (Line 190, 5°W) to 4.9 km (Line 180, 0°) and 3.2 km (Line 170, 2°E) (Fig. 1.22) (*Jokat and Schmidt-Aursch*, 2007).

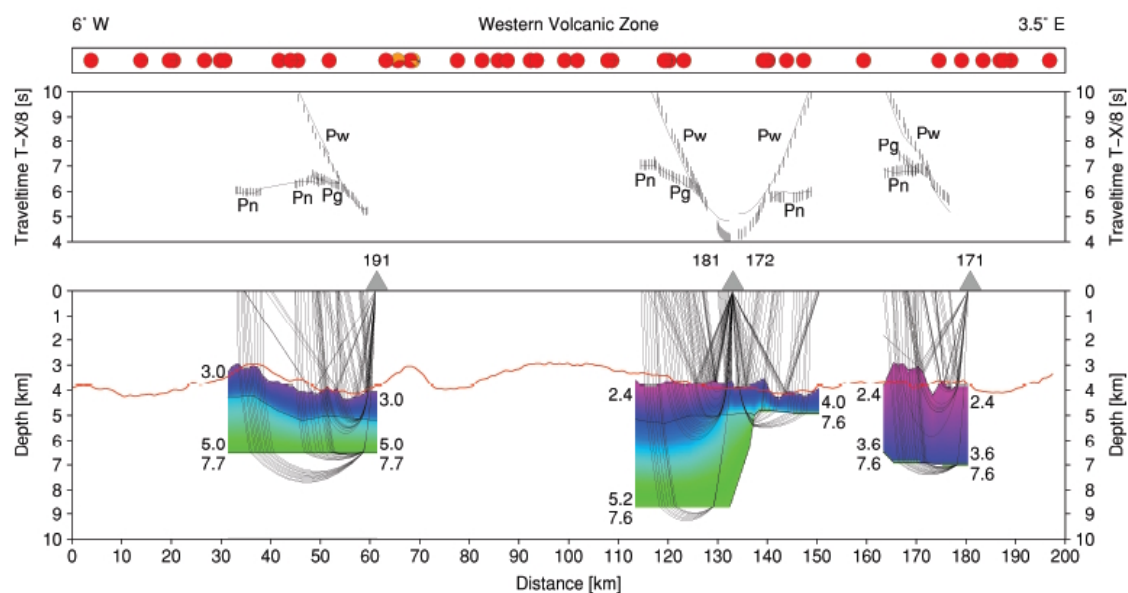


Figure 1.22: Seismic modelling based on refraction profiles within the WVZ by the AMORE expedition (*Jokat and Schmidt-Aursch*, 2007). Coloured dots indicate dredge content (red: Basalt, green: Peridotite, orange: Gabbro, blue: Others).

The magnetic data (Fig. 1.17) contrast the WVZ to the rest of Gakkel ridge in showing a continuously high magnetic anomaly along the rift valley which terminates at the segment end at 3°E. This is possibly an effect of the greater magma supply.

The AMORE expedition found only two hydrothermal signatures within a small area (Fig. 1.20), one of them was confirmed as Aurora vent field at 6° 15'W.

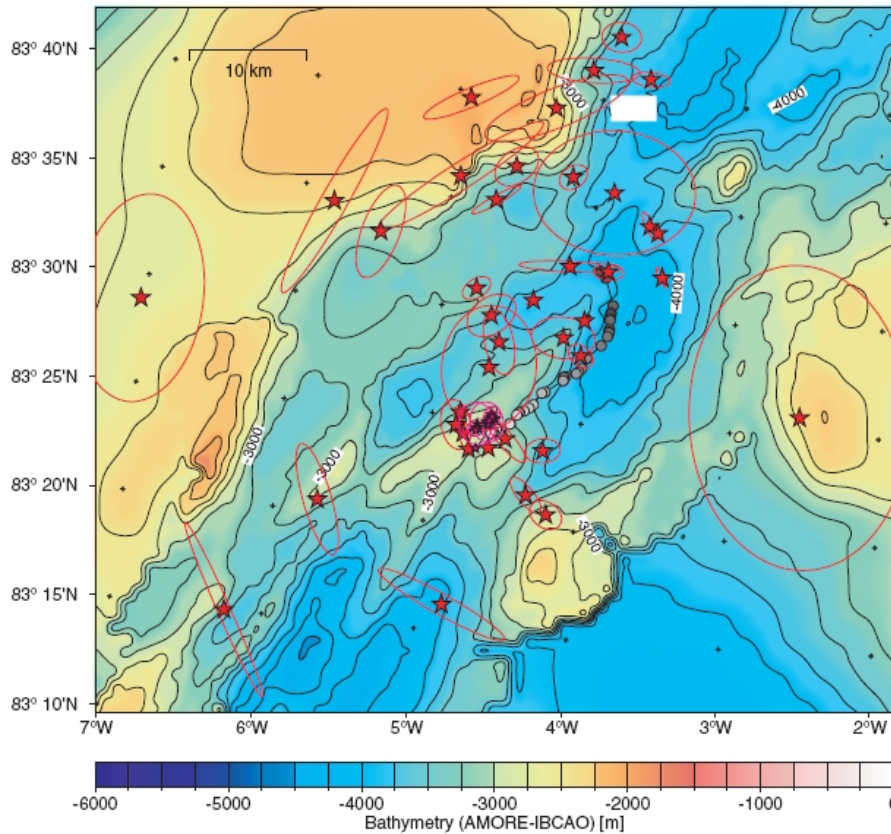


Figure 1.23: Microearthquake activity recorded by the AMORE expedition in the WVZ (*Schlundwein et al., 2007*).

Within the WVZ (Fig. 1.19) the array GAK0 recorded 54 events (Fig. 1.23) of two distinct types. *Schlundwein and Linder (2007)* speculate that the first type corresponds to tectonic origin and hence active faulting. Waveform of the events as well as hypocenter locations in time and space are uncorrelated. The events are located at the rift flanks, and here preferentially at the northern rift valley wall. This may point to asymmetrical spreading. The earthquakes of the second type are clustered in time and space and exhibit similar waveforms. These events locate at a volcanic structure (*Michael et al., 2003*) within the central rift valley at a depth about 2.5 km and are interpreted to be magmatic in origin.

Summary WVZ: Despite the lower spreading rate the WVZ can maintain slow spreading crustal accretion character in a magmatic accretion environment. The Aurora hydrothermal vent field has been confirmed.

Sparsely Magmatic Zone (84.38°N 3°E - 86°N 29°E)

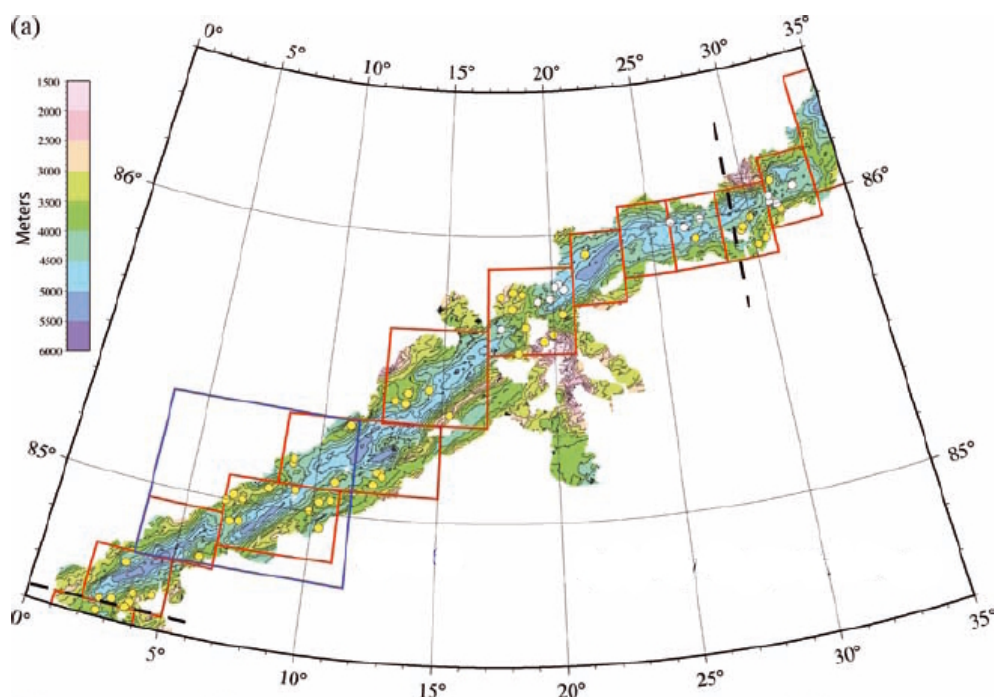


Figure 1.24: Bathymetric map of the SMZ (Cochran, 2008). White and yellow circles are closed concentric structures interpreted as seamounts.

The beginning of the SMZ is defined through a left stepping non-transform offset, abruptly changing the appearance of the ridge. The rift valley floor drops by 1.1 km within 5 km of the offset and the rift valley narrows to only 5-8 km. A lithologic change takes place with basalts abruptly almost completely missing from the dredged rocks (Fig. 1.16), instead the dredges recovered extensive peridotites (Michael *et al.*, 2003). The magnetic anomaly drops off suddenly within 20 km of the offset (Fig. 1.17). An amagmatic accretion mode seems to be indicated, particularly at the start of the segment.

At 7°E an oblique transform offsets the axis 15 km to the right and a similar axial valley continues further. Two volcanic centers at 13°E and 19°E focus melt and AMORE expedition recovered some basalt at 13°E. The 19°E volcanic center is accompanied by a shallowing of the rift valley and an across-axis ridge. At this volcanic center only basalts have been dredged.

Between 13°E and 16°E Goldstein *et al.* (2008) found an isotopic boundary which divides westerly DUPAL isotopic- and easterly normal pacific/atlantic isotopic characteristics. It is possible that this chemical boundary together with slow spreading is responsible for a threshold step to ultraslow appearance of the ridge (Cochran, 2008).

Throughout the SMZ the few existing seamounts are situated along faults in the rift valley walls or at the edge of the valley rather than at the rift axis (*Cochran, 2008*). Two large diffuse hydrothermal anomalies are found within it's boundaries (Fig. 1.20).

The AMORE expedition shot 4 seismic refraction profiles within the SMZ (Fig. 1.18). Crustal seismic thickness of 1.4-1.5 km (Line 160, 8°E), 2.5 km (Line 150, 15°E), 1.9 km (Line 200, 20°E) and 2.1 km (Line 210, 25°E) (Fig. 1.25) are consistently smaller than in the WVZ. Line 150 shows the thinnest crust. Both line 150 and 160 sample amagmatic sections and it is therefore not clear if they reflect oceanic crust or altered mantle material.

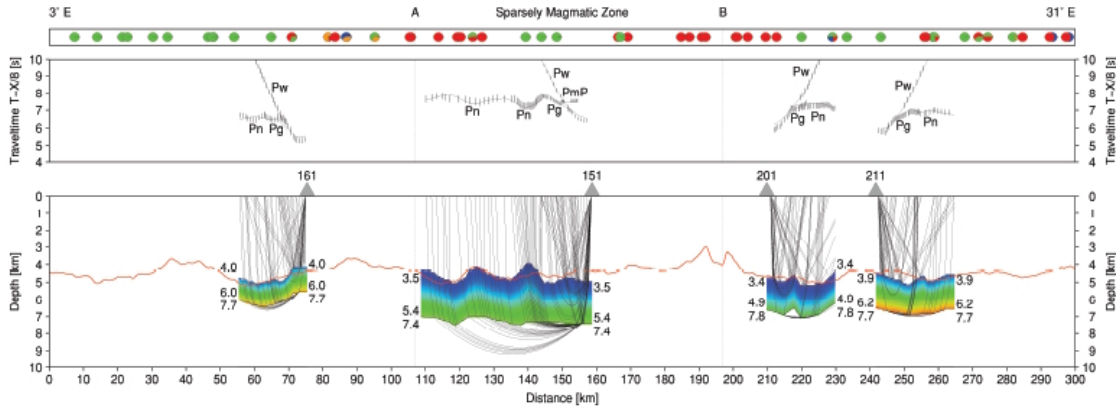


Figure 1.25: Seismic modelling based on refraction profiles within the SMZ by the AMORE expedition (*Jokat and Schmidt-Aursch, 2007*). Coloured dots indicate dredge content (red: Basalt, green: Peridotite, orange: Gabbro, blue: others).

Array GAK1 from the AMORE expedition drifted in the SMZ between 15° and 17°E (Fig. 1.19) over an amagmatic spreading section of the ridge, between the two volcanic centers (13°E, 19°E). The 39 events recorded by the array (Fig. 1.26) are predominantly located within the central rift valley, with some events at the northern rift flank. This could point to active tectonics and asymmetric spreading (*Schlindwein et al., 2007*). In comparison with the number of events recorded at the WVZ and the EVZ, the event rate at the SMZ is significantly smaller.

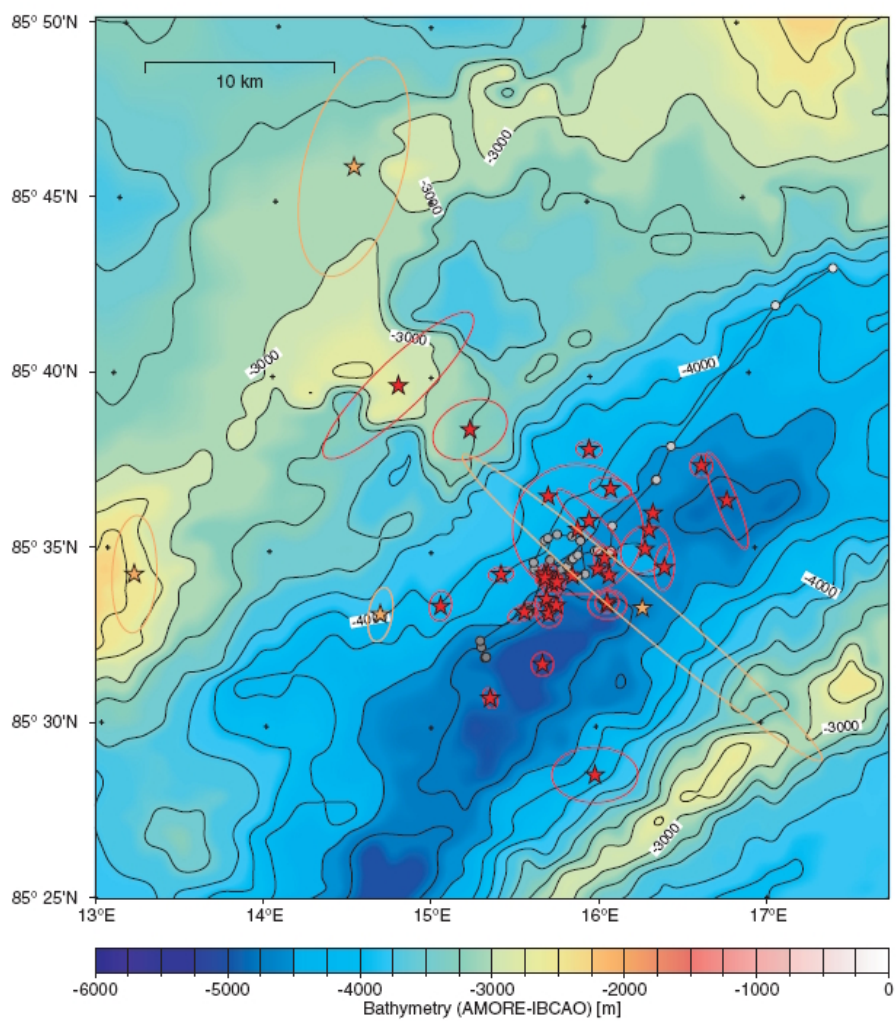


Figure 1.26: Microearthquake activity recorded by the AMORE expedition in the SMZ (*Schindwein et al., 2007*).

Summary SMZ: From the western to the eastern end of the SMZ the bathymetric differences in depth gets smaller. West of the 17°E oblique offset the mode of accretion seems to be amagmatic, further east it changes again to magmatic. Two volcanic centers east and west of the oblique offset are found.

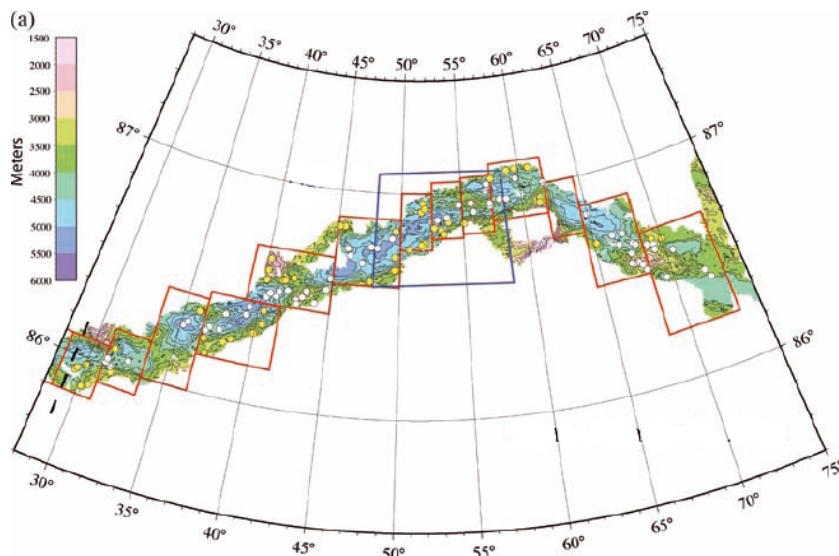
Eastern Volcanic Zone (86°N 29°E - 78.5°N , 128°E)

Figure 1.27: Bathymetric map of the EVZ (Cochran, 2008). White and yellow circles are closed concentric structures, interpreted as seamounts.

Although of volcanic character, the appearance of the EVZ is very different from the WVZ. A highly variable relief with a deep axial valley (Fig. 1.15) goes along with numerous elongated volcanic centers along axis (31°E , 37°E , 43°E , 55°E , 69°E , 85°E , 93°E) which are separated by amagmatic sections. The volcanic axis has 8 - 12 km offsets which are completely contained within the rift valley (Michael *et al.*, 2003). Tectonics form a distinct change in ridge axis orientation without thickened crust (Cochran *et al.*, 2003; Michael *et al.*, 2003) at 30°E and 62°E .

The 85°E volcanic center is the largest within the EVZ and also the most recently active as AMORE recovered fresh basalt from this area (Michael *et al.*, 2003). It is also a major hydrothermal source. Throughout the EVZ hydrothermal activity is noticeable in discrete centers, the signature of the 85° volcanic center is recordable as far west as 69°E (Fig. 1.20). Dredging recovered almost exclusively basalt (Fig. 1.16).

Seismic refraction modelling can give crustal thicknesses only to about 60°E (Fig. 1.18): 2.7 km (Line 220, $40\text{--}45^{\circ}\text{E}$), 2.7 km and 3.3 km (Line 230, $45\text{--}50^{\circ}\text{E}$), 2.9 km (Line 240, 55°E) and 3.5 km (Line 250, 60°E) (Fig. 1.28), showing an increase compared to the SMZ. However, all seismic lines are situated near or across axial bathymetric highs and sample the increased magmatism at these centers.

Array GAK2 (Fig. 1.19) recorded a total of 59 events (Fig. 1.29) at the rift flanks about 35 km northwest of the 85°E volcanic center. No microearthquakes of magnitudes 2 and larger occurred at the volcanic center itself. Instead a swarm of over 200 seismoacous-

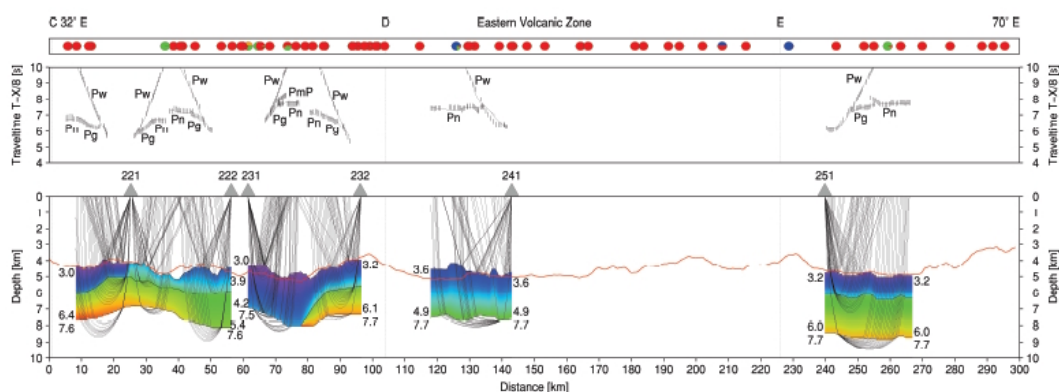


Figure 1.28: Seismic modelling based on refraction profiles within the EVZ by the AMORE expedition (*Jokat and Schmidt-Aursch, 2007*). Coloured dots indicate dredge content (red: Basalt, green: Peridotite, orange: Gabbro, blue: Others).

tic events was detected in the central valley near the volcanic center. This has been interpreted as the sounds of an ongoing submarine eruption (*Schindwein et al., 2005*).

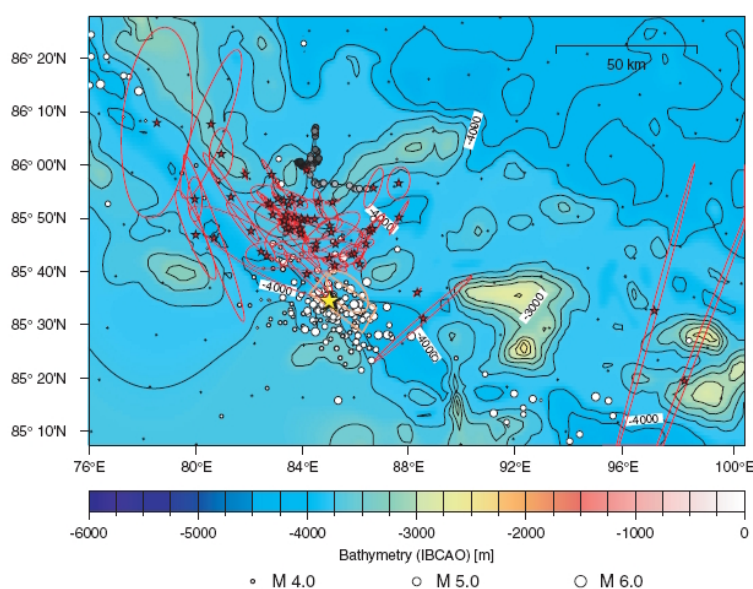


Figure 1.29: Microearthquake activity recorded by the AMORE expedition in the EVZ (*Schindwein et al., 2007*).

Summary EVZ: A highly variable relief goes along with numerous volcanic centers and hydrothermal sources, the most prominent at 85°E. The mode of crustal generation through melt generated at the axis seems to be the same as that of the eastern segment of the SMZ with melt transported to focused volcanic centers.

1.3 The 85°E Region at Gakkel Ridge: Observations and Interpretation

1.3.1 The Teleseismic Earthquake Swarm of 1999

The earthquake swarm of 1999 at around 85°E, 85.5°N consisted of 252 teleseismically recorded events, registered in the ISC database *ISC* (2008), starting on January the 17th with a $m_b = 4.2$ event and terminating on the 24th of September with a sole event after more than a month quiescence.

The swarm was exceptional in every respect, from the total number of events to the recorded high magnitudes with $m_{bmax} = 5.2$ so it caught the attention of the scientific community almost immediately. Fortunately, during the swarm the SCICEX expedition conducted a sidescan-sonar investigation of Gakkel ridge, compiling a bathymetric map of Gakkel ridge (Fig. 1.30) and giving a first framework for a tentative geological interpretation.

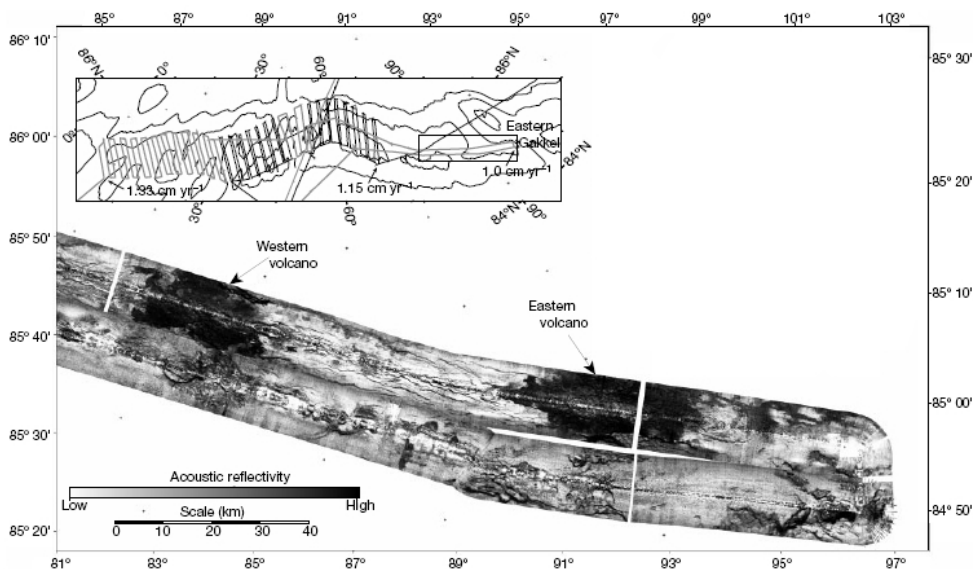


Figure 1.30: Bathymetry and back-scattering of the 85°E region (*Edwards et al.*, 2001): The upper left inset shows tracklines for a part of the SCICEX survey in close up with the rectangular area in close up below. High backscatter areas are labelled the western volcano and the eastern volcano. The area of the western volcano corresponds to the swarm location.

1.3.2 Analysis of the Teleseismic Earthquake Swarm of 1999

Müller and Jokat (2000) performed a first analysis of the swarm based on the NEIC catalogue (*NEIC*, 2010). They could distinguish between two phases, before and after the 4th of March, based on b-values and source mechanisms of the biggest 23 events with Harvard centroid-moment-tensor (CMT) solutions:

During the first phase, the greatest number of events occurred with almost exclusively double-couple source mechanisms indicating normal faulting in an extensional stress regime. At the beginning of phase 2, the source mechanisms changed to events with predominantly non-double couple components.

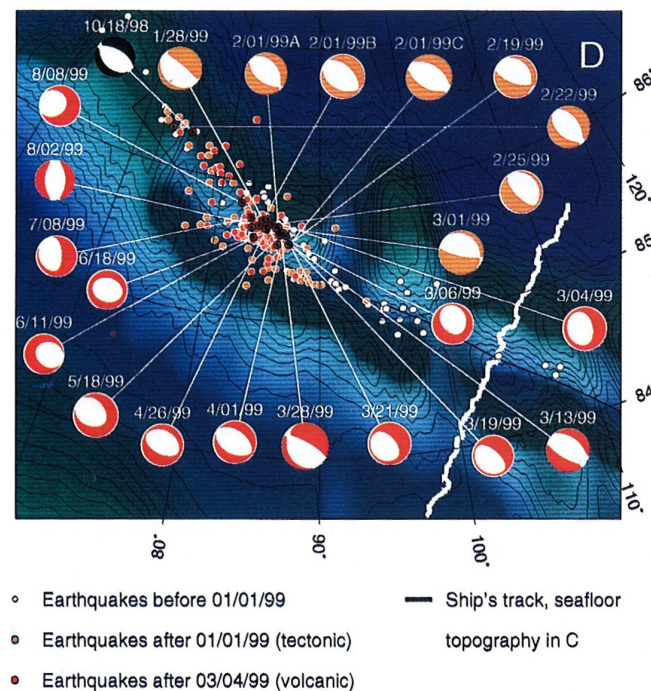


Figure 1.31: Distribution of hypocenters of large events with CMT solutions (*Müller and Jokat*, 2000), NEIC location (*NEIC*, 2010)

Furthermore, the b-values of the magnitude-frequency relationship increase significantly from 1.4 to 1.9 when calculated for the pre-March 4 and the post-March 4 events with a magnitude of completeness m_{bc} of 4.5. The b-value is calculated from the cumulative number of events and their magnitudes above a magnitude of completeness m_{bc} which indicates a threshold-value for recording of all occurring events. Generally, the b-value gives the ratio of the number of events with high magnitudes to the number of events with low magnitudes. A preponderance of small events versus large events results in large b-values ($b > 1$) which are therefore typical for swarm events lacking large magnitude main shocks. The events of 1999 from the NEIC-catalogue had high b-values and were

taken to be swarm-like. *Müller and Jokat* (2000) interpreted the swarm as having normal faulting tectonic events before March 4 and events from volcanic origin, for example caldera-collapsing events after March 4.

Later, *Tolstoy et al.* (2001) used also NEIC data (*NEIC*, 2010), supplemented with the Reviewed Event Bulletin data of the IDC (*IDC*, 2000). They interpreted the swarm as having a volcanic character, based on a more or less consistent b-value of about 1.5 throughout the entire duration of the swarm. This differs from the findings of *Müller and Jokat* (2000).

The non-double couple characteristic of later events could point to caldera-collapsing events (*Müller and Jokat*, 2000) but *Tolstoy et al.* (2001) found it more likely to indicate a distortion of source mechanisms due to changed elastic moduli from intrusions.

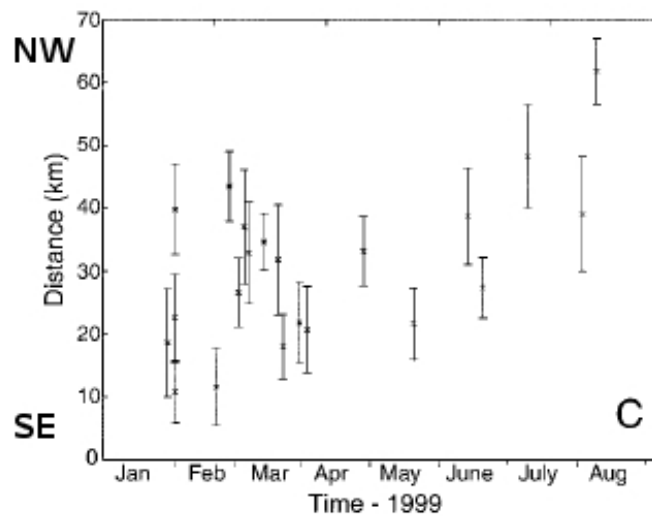


Figure 1.32: Epicentral migration of 21 large events from reference point (88°E , 85.5°N) (*Tolstoy et al.*, 2001), USGS event location

They also plotted the temporal evolution of the swarm as along-axis distance from a reference point at the southeastern end of the swarm at 88°E , 85.5°N (Fig. 1.32), showing a migration of the larger earthquakes to the northwest. This was interpreted as the propagation of magmatic dykes at a horizontal speed of 8 m/h which is significantly lower than dyke-propagation events observed at other ridges (*Dziak et al.*, 1995; *Dziak and Fox*, 1999; *Tolstoy et al.*, 1999).

The largest cluster of events in time and space took place on February 1 with three high magnitude events (Fig. 1.33) within the potential flow area observed by *Edwards et al.* (2001). This makes it likely that a major dyke ascended under the volcanic complex in the center of the valley from an initial depth greater than 5 km and triggered the observed bounding-wall events. The parental magma body may be within the mantle which would also explain the chemical composition of Gakkel ridge lavas.

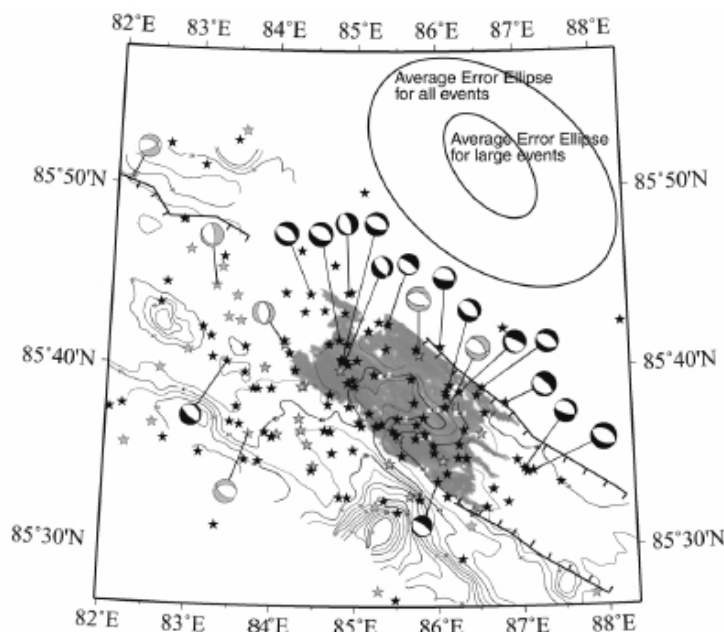


Figure 1.33: Selected epicenters of the 1999 swarm from the NEIC-catalogue (*NEIC*, 2010) with harvard moment tensor given for 21 large events. Grey stars and matched source mechanisms indicate events which took place after 6th of May. 100 m contours are given for the bathymetry. The lava-flow area postulated by *Edwards et al.* (2001) is shaded in grey, (*Tolstoy et al.*, 2001).

The subsequent northwest-migration of events slowly extended to the western end of the high backscatter area observed in the SCICEX expedition up to May 6 (Fig. 1.33). *Tolstoy et al.* (2001) interpreted this as a succession of vertical magmatic pulses, migrating northwestwards from a deep source.

Recently *Riedel and Schlindwein* (2009) relocated the swarm of 1999 (Fig. 1.34) with the localization routine Hyposat (*Schweitzer*, 2001). As databasis they used the meanwhile available seismologist reviewed ISC catalogue (*ISC*, 2008). In contrast to locations in catalogues they applied an optimized regional velocity model supplemented by IASP91 (*Kennett and Engdahl*, 1991) and PREM (*Dziewonski and Anderson*, 1981) for deeper structures. An average error of 10 km in the semimajor-axis of the epicenters remains within a confidence interval of 95%. The depth of events is far less constrained.

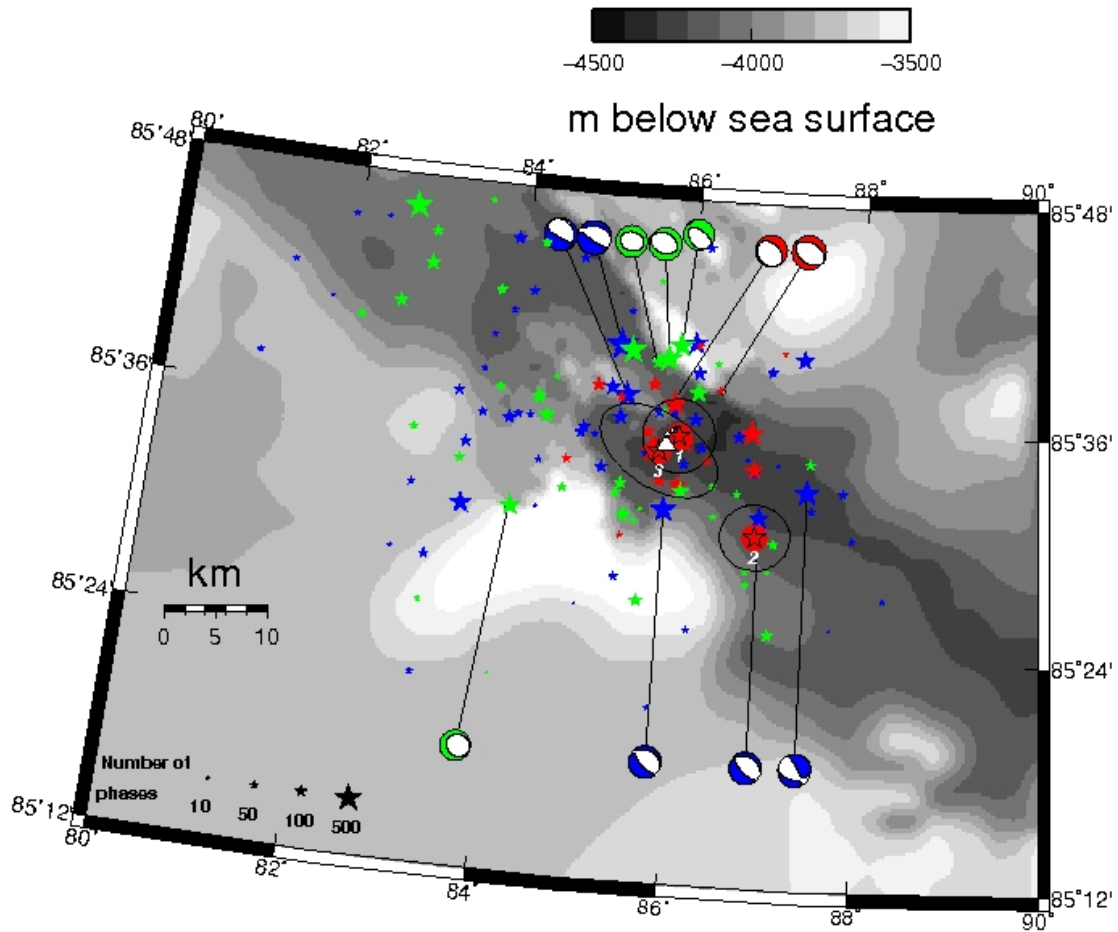


Figure 1.34: Hyposat relocation, numbered events are drawn with error ellipses, colours of the epicenters and associated source mechanisms refer to episodes in time (blue: 1999/01/17-1999/03/01, red: 1999/03/02-1999/04/13, green: 1999/04/14-1999/09/24) (Riedel and Schlindwein, 2009).

Station residuals for events with root-mean-square (RMS) < 1 sec mostly cluster around 0 sec. However, negative station residuals remained for North Atlantic stations (in particular KBS, SPITS but to a lesser extent also all other examined stations), implying that seismic waves sample a higher velocity region in this direction as predicted by theoretical models. By contrast, the westernmost Alaska stations (ANM) and the eastern Siberian stations (TIXI, SEY) display strongly positive station residuals (Fig. 1.35) and presumably lower velocities in the eastern direction.

A cross correlation analysis of the waveforms at the nearest stations found only three highly correlating events. These peculiar events occur within 5 days and locate close to each other at the adjacent southern flank in the vicinity of Oden volcano (Fig. 1.34), reflecting the same source mechanism.

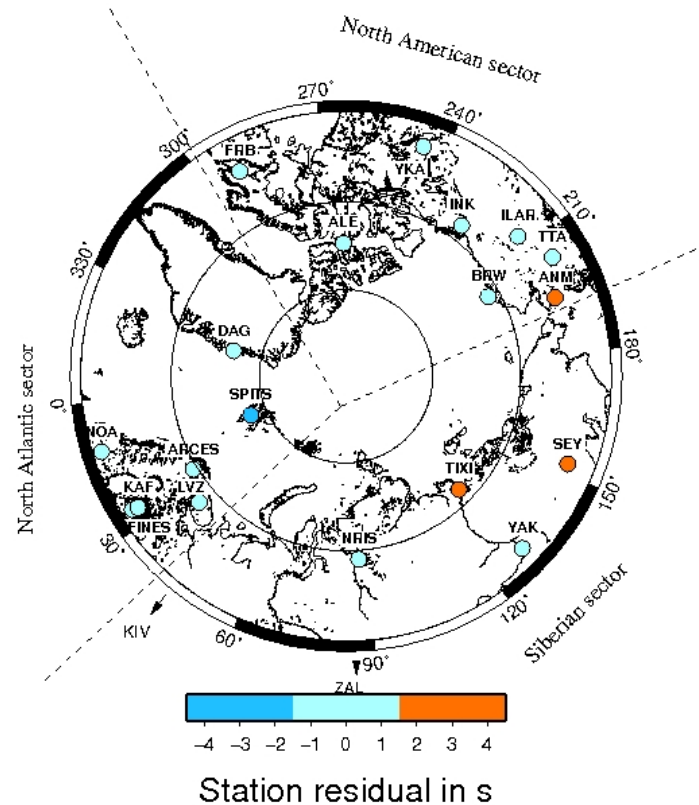


Figure 1.35: Station residuals for selected near-stations (*Riedel and Schlindwein, 2009*).

Analysing in particular averaged event depths using a median window in time, *Riedel and Schlindwein (2009)* subdivided the seismicity in three episodes. Within the first, tectonic activation of the entire ridge segment occurs. Five high magnitude events $m_b > 5$ might indicate faulting down to the upper mantle. Events mirror heterogeneous crust and are predominantly normal-faulting. The second episode (after March 1) is characterised by ascending hypocentral depths, less high magnitude events and increasing non-double couple components for a more narrow activated area around the three similar events which belong to the late part of this phase and indicate possibly an ascending dike. Episode three started around April 14 with a drastic drop in seismicity rate. This phase corresponds to the second phase of seismicity defined by *Tolstoy et al. (2001)* and could be triggered by tectonic adjustment.

1.3.3 Geological Framework of the 1999 Swarm at the Volcanic Complex

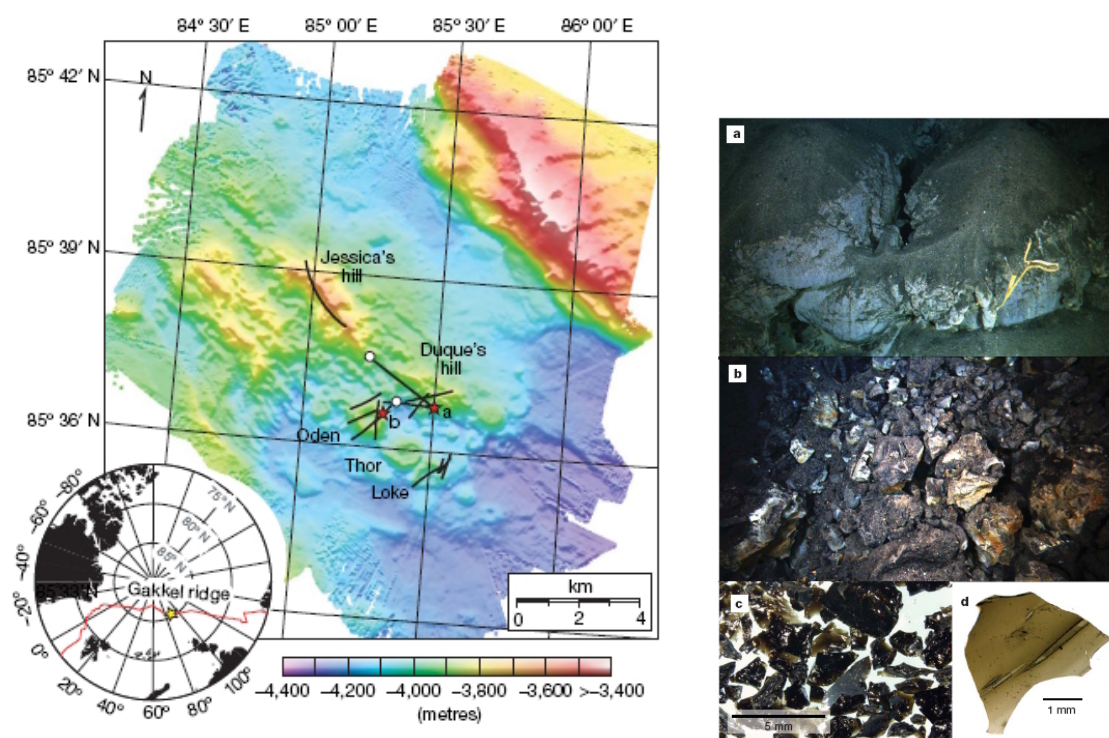
In 1999 the SCICEX expedition passed over the active area and found regions of high acoustic backscatter (*Edwards et al.*, 2001), marked in dark grey in Fig. 1.30. They are within the rough area where most earthquakes have been preliminarily located. *Edwards et al.* (2001) interpreted the strong reflective echoes as freshly erupted lava flows over a large area (marked grey in Fig. 1.33).

Further evidence for recent volcanic activity stems from the observation of a massive hydrothermal plume with unusual thickness and height of rise (Fig. 1.20) compared to other vent sites at Gakkel ridge and other ridges (*Edmonds et al.*, 2003; *Baker et al.*, 2004). The water column anomaly was detected as far west as 69°E and is interpreted to result from a massive event plume maintained over more than one year (*Edmonds et al.*, 2003), and thus eventually relates to the presumed volcanic activity connected with the earthquake swarm in 1999.

In 2007 the **AGAVE** expedition returned to the 85°E volcanic site and found that the signature of the hydrothermal plume had considerably diminished in thickness and amplitude from 2001 to 2007, indicating waning activity (*Stranne et al.*, 2010).

They also found further evidence for unusual volcanic activity at this location: A newly acquired high-resolution bathymetry of the site of the 85°E complex (Fig. 1.36(a)) showed numerous distinctive cratered cones aligned along axis in the central valley. The biggest such axial structures have been named Oden, Thor and Loke. They are typically up to 2,000 m in diameter and some 100 m high with a flat top and a prominent central crater.

Analysis of samples from two sites (Fig. 1.36(a)) showed nearly entirely juvenile clasts of glassy basalt in the form of angular fragments with small amounts of Limu o Pele (Fig. 1.36(b), d) included. This pyroclastic deposits are evidence for explosive volcanism which must be driven by primary gas as explosive water-rock interactions are impossible beyond the critical water depth of about 3,000 m. An order of magnitude higher content of magmatic volatiles than observed in MOR magma is required to drive these explosive eruptions. This volatile content could be produced locally when magmatic gases accumulate at the top of the magma chamber. The large earthquakes may have fractured the stable roof of the magma chamber and triggered an eruption. *Sohn et al.* (2008) speculates that magma chambers at ultraslow-spreading ridges may build up over long time-intervals within the deep crust, supporting infrequent explosive discharges of volatile-rich magmas.



(a) Bathymetry of the 85° E volcanic area acquired during AGAVE (Sohn *et al.*, 2008). White circles are sites where samples have been taken from seafloor at 4,000 m water depth (Sohn *et al.*, 2008). Stars with letters show sites of photos in Fig. 1.36(b). Black lines are CAMPER profiles for high resolution digital seafloor imagery.

Figure 1.36: Bathymetry of the 85°E volcanic area and photographs of deposits from this area.

Along the black lines in Fig. 1.36(b) digital imagery was obtained which showed unconsolidated pyroclastic deposits covering the entire photographed area (Fig. 1.36(a)). The clasts were distributed through multiple falls and showed spatial variations of thickness as well as differences in colour. The thickest deposits of up to 0.1 m were lying on weathered, broken lava flows at Jessica's Hill and Duque's Hill (Fig. 1.36(a)). Only a light dusting of pyroclastic deposits on fresh pillow lavas and sheeted flows have been observed covering Oden and Loke volcanoes. These findings contradict the interpretation of Edwards *et al.* (2001) of the high backscatter region as fresh lava flows from a single eruption but rather speak for multiple episodes of explosive volatile discharge. The new bathymetry and evidence for explosive volcanism led Schlindwein and Riedel (2009) to reanalyse the 200 seismoacoustic events recorded in 2001 and tentatively interpreted to result from ongoing volcanic activity (Schlindwein *et al.*, 2005).

Riedel and Schlindwein (2009) did a forward modelling of the seismoacoustic signals into the water column with a point source Ricker wavelet placed directly at the seafloor at different locations (Fig. 1.37) within a source region indicated by changing backazimuths of the signals recorded during the drift of the seismic array. The source area lies confidently within overlapping backazimuth sectors near the southern rift boundary fault (Fig. 1.37). However a specific volcanic structure could not be identified as the source region lies south of the area covered by multibeam data.

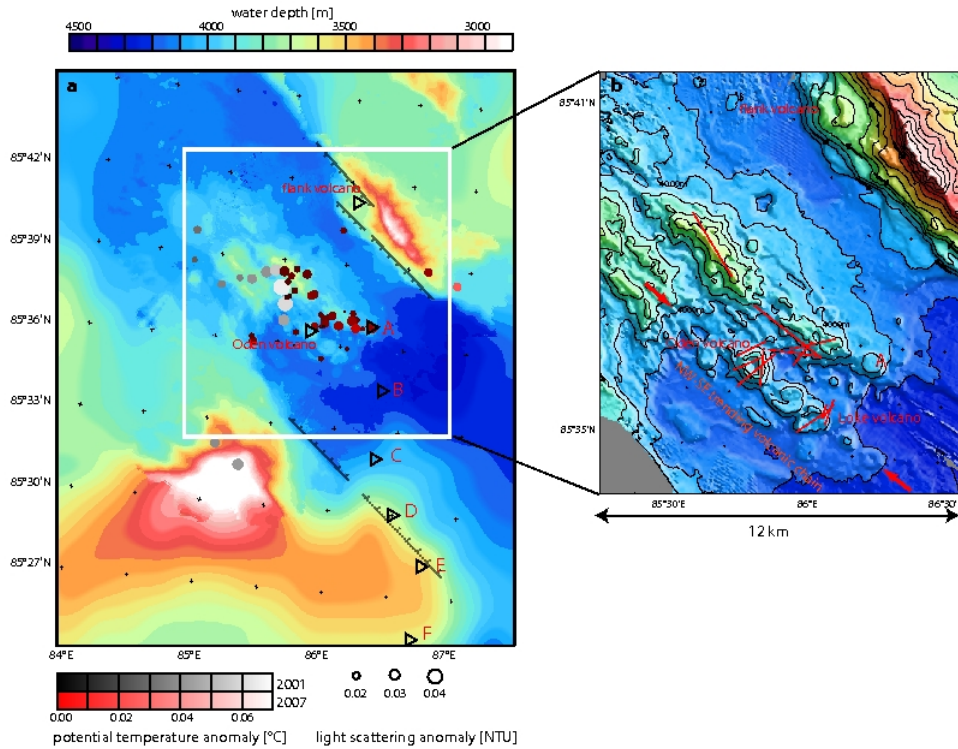


Figure 1.37: Close up of the 85°E volcanic complex, including light-scattering anomalies from AGAVE and AMORE expeditions. Triangles show the investigated source sites for forward modelling of the seismoacoustic signals (*Schlindwein and Riedel, 2010*)

A Strombolian eruption style fits best the observed impulsive signals and their rhythmical occurrence (*Chadwick et al., 2008*). Magmatic gases are assumed to rise faster in a narrow conduit than the magma ascends, the gases discharge explosively when reaching the surface. *Schlindwein and Riedel* (2010) speculate that the Strombolian events represent mild degassing explosions along major faults that mine a magma chamber which possibly started to discharge in 1999.

In 2007, three seismological arrays on ice floes recorded about 400 microearthquakes in the central rift valley but no more seismoacoustic signals (*Schlindwein and Linder, 2007*). Combined with the decreased hydrothermal activity this might indicate that the area has come to post-eruptive rest.

Chapter 2

Earthquake LOCALIZATION

When a transient stress imbalance is produced within or on the surface of an elastic medium, it releases energy in the form of elastic waves which travel spherically outward from the source. These are seismic waves. Their properties are subject to elastodynamics and depend on the medium through which they propagate. During propagation the rays sample the earth's interior (Fig. 2.1), before they are recorded at the surface. For the following theoretical statements I have made use of the book of *Stein and Wyession* (2003).

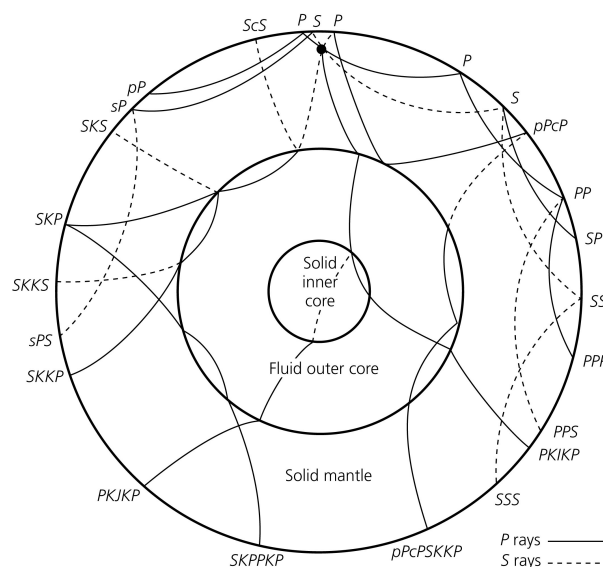


Figure 2.1: Examples of body wave phases including nomenclature, sampling different depths and portions of the earth (*Stein and Wyession, 2003*).

Each ray is identified by its horizontal slowness (p) which is therefore also called the ray parameter. Integrating p along the ray path given by the angular distance (Δ) gives the

traveltime (T). As p is constant for its ray but the ray propagates through media with different properties, the raypath changes as given by Snell's law (Eq. 2.1) for a spherical layered earth (Fig. 2.2):

$$p = \frac{r_1 \sin i_1}{v_1} = \frac{r_2 \sin i_2}{v_2} = \frac{dT}{d\Delta} \quad (2.1)$$

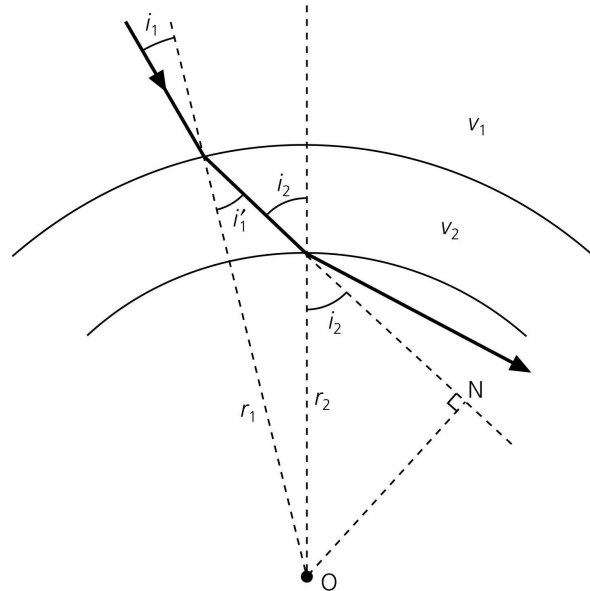


Figure 2.2: Snell's law for a spherical earth (*Stein and Wysession, 2003*).

The earth can be modelled as a series of spherical shells of uniform-velocity material. Generally, velocity increases with depth. Snell's law gives the dependence between incidence angle (i) and velocity (v) of the ray. i is defined as the angle between the ray path and the radius-vector. At each layer's boundary the incidence angle of the leaving ray changes according to the velocity of the succeeding layer. When $i = 90^\circ$ the ray alters direction, it 'bottoms out' and returns again to the surface.

When a receiver records ground motion and we have information about the origin time and place of these motions we are able to obtain the traveltime (T) of the wave from the origin to the source. Traveltime can be expressed as a linear equation (Eq. 2.2) of ray parameter, angular distance (Δ) and intercept time (τ). After reorganization for τ , this equation can be used to invert traveltime for velocity, depending on Δ .

$$T(p) = p\Delta(p) + \tau(p) \quad (2.2)$$

For the calculation of hypocenters, it is imperative to know the structure of the earth. Recordings of seismic rays which originated from well-constrained natural or artificial

seismic sources and sampled different portions of the earth give information about its velocity and structure. In the 1940s, the Jeffrey-Bullen tables for a radially symmetric earth model with continental crust were compiled by combining traveltimes data from many different sources and angular distances for various body phases. Essentially this model is still correct today. In the new models, refinements for specific regions e.g. between crust and mantle have been included. It is important to remember that all thus derived velocity models describe the earth as radially symmetric with homogenous layer properties. Regional differences especially within the crust and upper mantle which can have a large impact on traveltimes are neglected in the standard earth models.

The most widely used velocity models today are the following:

- PREM (*Dziewonski and Anderson, 1981*)
- IASP91 (*Kennett and Engdahl, 1991*)
- AK135 (*Kennett et al., 1995*)

Approximating the complex earth structure by a spherically symmetric earth model introduces an error into the localization of earthquakes which is unavoidable but not easy to constrain as it depends for example on local heterogeneity of the crust and upper mantle in the source region. This error is difficult to quantify and its size can only be assumed.

Earthquake localization means to fit one origin to all recorded times and phases. This can be accomplished by either forward modelling or solving the inverse problem. The forward calculation starts at an assumptive origin and computes the raypath repeatedly until an origin is found which best satisfies all recordings. For each calculation a unique solution is found.

The inverse problem in contrast starts at the recording point and traces the raypath backwards to the source. This can be accomplished by either the linear inverse problem or the nonlinear inverse problem.

Summary: In earthquake localization we have to reason from the recorded ground motion back to the origin. This can be done through forward modelling or through solving the inverse problem in linear or nonlinear methods. An earth model must be used for localization but it introduces an error which is difficult to quantify.

2.1 Linear Inverse Localization - Hyposat

Hyposat (*Schweitzer, 2001*) starts at a hypothetical hypocenter location calculated by the mean of backazimuth solutions at the recording stations. The first source time (t_0) is derived by Wadati's approach for the arrival times of primary and secondary waves (t_{ps}) in equation 2.3. The source depth can be fixed at the start to be calculated after a final epicenter solution has been reached.

$$t_0 = t_{ps} - \left(\frac{\Delta}{v_{ps}} \right) \quad (2.3)$$

The linear forward problem then is solved by iterative inversion of the generalized matrix inversion code (GMI) (*Menke, 1978*) using the single-value-decomposition algorithm. The GMI itself (Eq. 2.4) is build up of a linearized system of normal equations consisting of phase information and partial derivatives for longitude, latitude and depth.

$$\begin{bmatrix} 1 & \frac{\delta t_i}{\delta lat} & \frac{\delta t_i}{\delta lon} & \frac{\delta t_i}{\delta z_0} \\ 0 & \frac{\delta dt_j}{\delta lat} & \frac{\delta dt_j}{\delta lon} & \frac{\delta dt_j}{\delta z_0} \\ 0 & \frac{\delta p_k}{\delta lat} & \frac{\delta p_k}{\delta lon} & \frac{\delta p_k}{\delta z_0} \\ 0 & \frac{\delta azi_l}{\delta lat} & \frac{\delta azi_l}{\delta lon} & 0 \end{bmatrix} \cdot \begin{bmatrix} \delta t_0 \\ \delta lat \\ \delta lon \\ \delta z_0 \end{bmatrix} = \begin{bmatrix} \Delta t_i \\ \Delta dt_j \\ \Delta p_k \\ \Delta azi_l \end{bmatrix} \quad (2.4)$$

t_i is a row with travel times and their residuals Δt_i

dt_i is a row with travel-time differences between two phases observed at the same station and their residuals Δdt_i

p_k is a row with observed ray parameter observations and their residuals Δp_k

azi_l is a row with observed backazimuth (from station to epicenter) observations and their residuals Δazi_l

The standard deviation is used as weighting parameter. For each iteration, the matrix and the standard deviations are recalculated until the solution is satisfactory.

Hyposat works with the standard velocity models (e.g. IASP91 (*Kennett and Engdahl, 1991*), AK135 (*Kennett et al., 1995*)), optionally it is possible to define horizontally layered velocity models for use at defined stations to take regional or local velocity variations into account.

As error indicator the root-mean-square (RMS) residual is calculated for each station and the confidence ellipsoid in 2D given for a preset confidence level.

2.2 Nonlinear Inverse Localization - NonLinLoc

The relationship between observable data and the model which generates them is generally expressed as $d = g(m)$. d are the observable parameters which are given as a physical system g acting on a model m . For solving the non-unique inverse problem of hypocenter location, NonLinLoc (Lomax *et al.*, 2000) uses a probabilistic correlation between the model parameters and observable parameters. The prior information about the location of an earthquake is expressed as a *a priori probability density* over the search area, which is linked to the final location, contained within the posterior probability distribution.

The general discrete problem (Tarantola and Valette, 1982) consists of describing the state of information contained in a parameter and defining this state of information with the use of probabilities over a parameter space: The probability distribution $p(A)$ (Eq. (2.5)) over a manifold of a physical parameter A is given by the probability density $f(x)$ in a coordinate system x :

$$p(A) = \int_A f(x)dx \quad (2.5)$$

An example is the *a priori probability density* which is independent of later observations which are investigated but gives information about the investigated area.

A homogeneous probability distribution $M(A)$ (Eq. (2.6)) is calculated using a normalized probability density $\mu(x)$ over a volume A with $\mu(x)$ given as $\mu(x) = \nu(x)/V$. $\nu(x)$ here denotes the distribution of volume over the region A and it need not be constant:

$$M(A) = \int_A \mu(x)dx \quad (2.6)$$

The likelihood or volumetric probability (Eq. (2.7)) corresponds to the ratio of the probability density $f(x)$ to the homogeneous probability density $\mu(x)$.

$$\varphi(x) = f(x)/\mu(x) \quad (2.7)$$

In the case of the involvement of more than one parameter i.e. probability, the use of a conditional probability distribution is indicated. A conditional probability distribution, that is the probability of an event A occurring while dependend on the occurance of an event B , can be expressed as a special case of a conjunction of probabilites. Applying this to the relationship between observed data d and a physical system G acting on the model m and assuming Gaussian uncertainties C_T within a otherwise linear G , we get the

theoretical probability density $\Theta(d, m)$ which represents the information on the physical correlation between d and m and includes the uncertainties of G in a mildly nonlinear manner (Eq. 2.9). It is expressed as a joint probability density $\Theta(d, m) = \Phi(d|m) \cdot \mu_M(m)$. Here $\Phi(d, m)$ denotes the conditional probability density for the observations d (Eq. 2.8) and $\mu_M(m)$ the homogeneous probability density on the model m :

$$\Phi(d, m) = \text{const} \cdot \exp(-1/2 \cdot (d - G(m))^t \cdot C_T^{-1} \cdot (d - G(m))) \quad (2.8)$$

$$\Theta(d, m) = \text{const} \cdot \exp(-1/2 \cdot (d - G(m))^t \cdot C_T^{-1} \cdot (d - G(m))) \cdot \mu_M(m) \quad (2.9)$$

Neglecting C_T as it is Gaussian, gives Eq. 2.10 which is only valid if all errors related to the observed data d are Gaussian (e.g. calculated traveltimes related to the velocity model, phase pick errors):

$$\Theta(d, m) = \delta(d - g(m)) \cdot \mu_M(m) \quad (2.10)$$

The *posterior probability density* $\sigma(d, m)$ is therefore given by Eq. 2.11 which includes the theoretical probability density $\Theta(d, m)$, a normalization constant k , the a priori probability density $\rho(d, m)$ and the homogeneous state of information $\mu(d, m)$:

$$\sigma(d, m) = k \cdot \frac{\rho(d, m) \cdot \Theta(d, m)}{\mu(d, m)} \quad (2.11)$$

When breaking up the data- and the model-space and integrating over the data-space D we get the solution for the posterior information in the model-space M (Eq. 2.12).

$$\sigma(m) = k \cdot \rho_M(m) \int_D \frac{\rho_D(d) \cdot \Theta(d|m)}{\mu_D(d)} dd \quad (2.12)$$

The probability that a point x lies within the region A is the integral of $\sigma(m)$ over the area A .

The likelihood-function $L(m)$ gives the integrated expression without the constant k and the a priori probability density dependent only on the model $\rho_M(m)$ and is a measure of how good the model m explains the data d .

For teleseismic earthquake analysis, NonLinLoc uses a spherical earth model in geographical coordinates. Consistent with above mentioned limitations imposed by the probabilistic approach, errors of phase time picks and the errors for travel time calculation inherent in the velocity model are assumed to be Gaussian. It follows the earthquake location methods of Tarantola and Valette (1982), Moser et al (1992) and Wittlinger et al (1993).

A break-up of the joint a priori probability density in information on hypocenter parameters h_0 , t_0 and information on the true traveltimes t and assuming a Gaussian error distribution around the measured traveltimes τ gives an a priori probability density $\rho(t)$ of Eq. 2.13 with w_{ij}^ρ as a sum of variance matrices for theoretical and observed traveltimes.

$$\rho(t) = \exp \left[-\frac{1}{2} \cdot \sum_{i=1}^K \sum_{j=1}^K w_{ij}^\rho (t_i - \tau_i) \cdot (t_j - \tau_j) \right] \quad (2.13)$$

The conditional probability density function $\Theta(t|h_0)$ describes then the probability that the true arrival times t can be calculated from the calculated travel times $T(x_i)$ (Eq. 2.14).

$$\Theta(t|h_0) = \exp \left[-\frac{1}{2} \cdot \sum_{i=1}^K \sum_{j=1}^K w_{ij}^\Theta (t_i - T(x_i) - t_0) \cdot (t_j - T(x_j) - t_0) \right] \quad (2.14)$$

Therefore the posterior probability density function for the location x_0 can be found through integrating over the origin time interval t_0 (Eq. 2.15) and written as the product of a normalization constant K with a misfit-function (Eq. 2.17):

$$\sigma(x_0) = \exp \int_{-\infty}^{\infty} \sigma(h_0) dt_0 = K \cdot \exp \left[-\frac{1}{2} \cdot g(x_0) \right] \quad (2.15)$$

$$g(x_0) = \sum_{i=1}^K \sum_{j=1}^K w_{ij} \cdot r_i(x_0) \cdot r_j(x_0) \quad (2.16)$$

with

$$r_i(x_0) = \tau_i - \frac{\sum_{k=1}^K w_{ik} \cdot \tau_k}{\sum_{k=1}^K w_{ik}} - T(x_i) \quad + \quad \frac{\sum_{k=1}^K w_{ik} \cdot T(x_k)}{\sum_{k=1}^K w_{ik}} \quad (2.17)$$

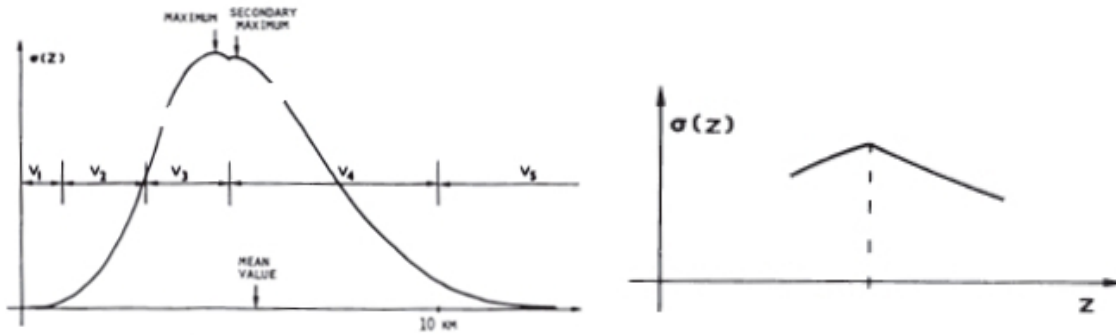
NonLinLoc calculates first the maximum-likelihood origin time via a probability density function (PDF) given in Eq. 2.18. This reduces the 4D problem to 3D (longitude, latitude, depth).

$$t_0 = \frac{\sum_{i=1}^K \sum_{j=1}^K w_{ij} \cdot (\tau_i - T(x_i))}{\sum_{i=1}^K \sum_{j=1}^K w_{ij}} \quad (2.18)$$

A 3D spatial traveltime grid for each phase (*Le Meur* (1998); *Le Meur et al.* (1997)), calculated with eikonal finite-differences following *Podvin and Lecomte* (1991) gives additionally the ray take-off angles in dip and azimuth through interpolation between adjacent nodes. Problems may arise if two or more rays simultaneously arrive near a node.

In actual localization the posterior PDF for the event is calculated in space throughout the grid using the analytical version of Eq. 2.12 for the marginal PDF in (x,y,z) (Eq. 2.15). The maximum value of the PDF is then taken as the preferred, maximum likelihood hypocenter (Eq. 2.16).

Tarantola and Valette (1982) warn that a discontinuous velocity model induces secondary maxima into the posterior PDF at the indicated depths, complicating the search for the maximum and causing a higher density of scatter samples to be drawn from the adjacent areas (Fig. 2.3(a)). Also if the posterior PDF has a maximum at the boundaries of the velocity layers it can cause the localization to oscillate and give hypocenters corresponding to the provoking boundary (Fig. 2.3(b)).



(a) Hypocenter has a second maximum (*Tarantola and Valette*, 1982) corresponding to a depth discontinuity. (b) Cause of oscillating hypocenter (*Tarantola and Valette*, 1982). This is an example of the discontinuity of the slope of the posterior PDF σ .

Figure 2.3: Examples for anomalous PDFs which are caused by a discontinuous velocity model.

The posterior PDF is normalized by assuming that the integral over the search volume is unity (*Lomax et al.*, 2000). For global mode, the search volume is the whole earth.

Samples are drawn in proportion to the value of the PDF and the volume of each grid cell, therefore defining a volume over the enclosed space which is designated in the following as the scattervolume.

As quality indicator of the PDF the covariance matrix is calculated from the scattersamples and transformed into standard error-ellipsoid parameters for 68% confidence level. The spatial extension of the PDF is given by the scatter volume for the 68% confidence interval within the final grid cell searched. Standard RMS travelttime residuals are output as well.

Chapter 3

DATA and LOCALIZATION ALGORITHM

3.1 Data: Phase Readings

Previous analyses of the earthquake swarm from 1999 were based on different datasets: *Müller and Jokat* (2000) used the NEIC catalogue, *Tolstoy et al.* (2001) relied in their analyses on the USGS event locations supplemented with the REB, and *Riedel and Schlindwein* (2009) drew on the comprehensive bulletin of the International Seismological Centre (ISC) (*ISC*, 2008). In this catalogue, ISC publishes a hypocenter with an origin time calculated by the stepwise linear forward localization routine ISCloc (*Luckett and Storchak*, 2006).

For my relocation I also decided to use the phase readings as published in the reviewed bulletin of ISC (*ISC*, 2008) about two years after the events, as they were carefully reviewed concerning incorrect allocation of phases to each event and should provide a good basis for relocation.

The 252 events of the 1999 earthquake swarm include 134 events with body wave magnitudes $m_b \geq 4.0$ including a total of 11 events $m_b \geq 5$. Table 3.1 gives the distribution of magnitudes to the number of events and the average number of phases used for localization by ISC. The distribution of average number of phases used in localization versus magnitude m_b (Fig. 3.1) shows an exponential increase of average number of phases with increasing magnitude, whereas at very high magnitudes $m_b \geq 5.0$ the localization algorithm ISCloc (*Luckett and Storchak*, 2006) seems to curtail excess phases.

m_b	no	av.phases	m_b	no	av.phases	m_b	no	av.phases
3.1	2	4	4.0	27	21	5.0	7	241
3.2	1	4	4.1	20	31	5.1	2	301
3.3	3	4	4.2	13	37	5.2	2	297
3.4	8	6	4.3	17	50			
3.5	14	6	4.4	15	59			
3.6	20	8	4.5	12	86			
3.7	22	9	4.6	7	128			
3.8	24	15	4.7	6	135			
3.9	24	17	4.8	5	192			
			4.9	1	215			

Table 3.1: Magnitudes by number of events and average number of phases used for localization by the ISC (*ISC*, 2008)

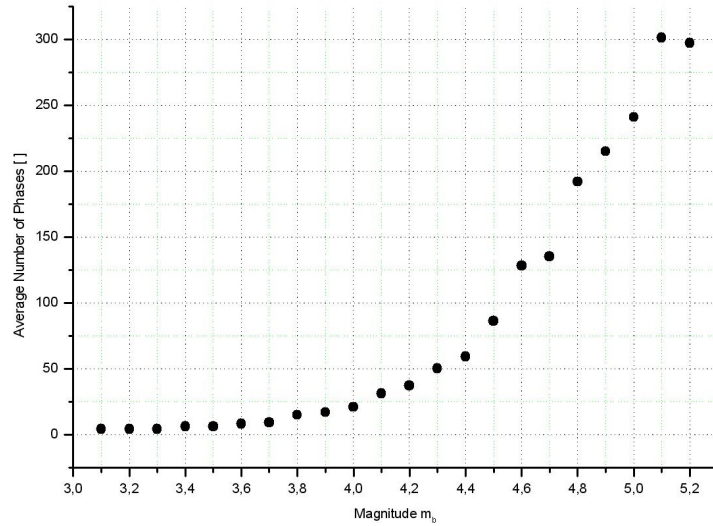


Figure 3.1: Average number of phases used in localization by ISCloc (*Luckett and Storchak*, 2006) versus magnitude m_b .

ISCloc (*Luckett and Storchak*, 2006) was used for the most part with a fixed depth of 10 km, yet some hypocenters were localized with variable depth. For 13 of these events with each less than 10 registered phases, high RMS values in the order of 80 seconds remained such that no reliable epicenter could be determined. The average RMS for the subsequent dataset of 239 events amounts to 1.13 seconds.

The ISC localization of the complete dataset (Fig. 3.2) gives epicenters around the 85°N/85°E volcanic complex, which I colour-coded for their recorded body-wave magnitudes m_b :

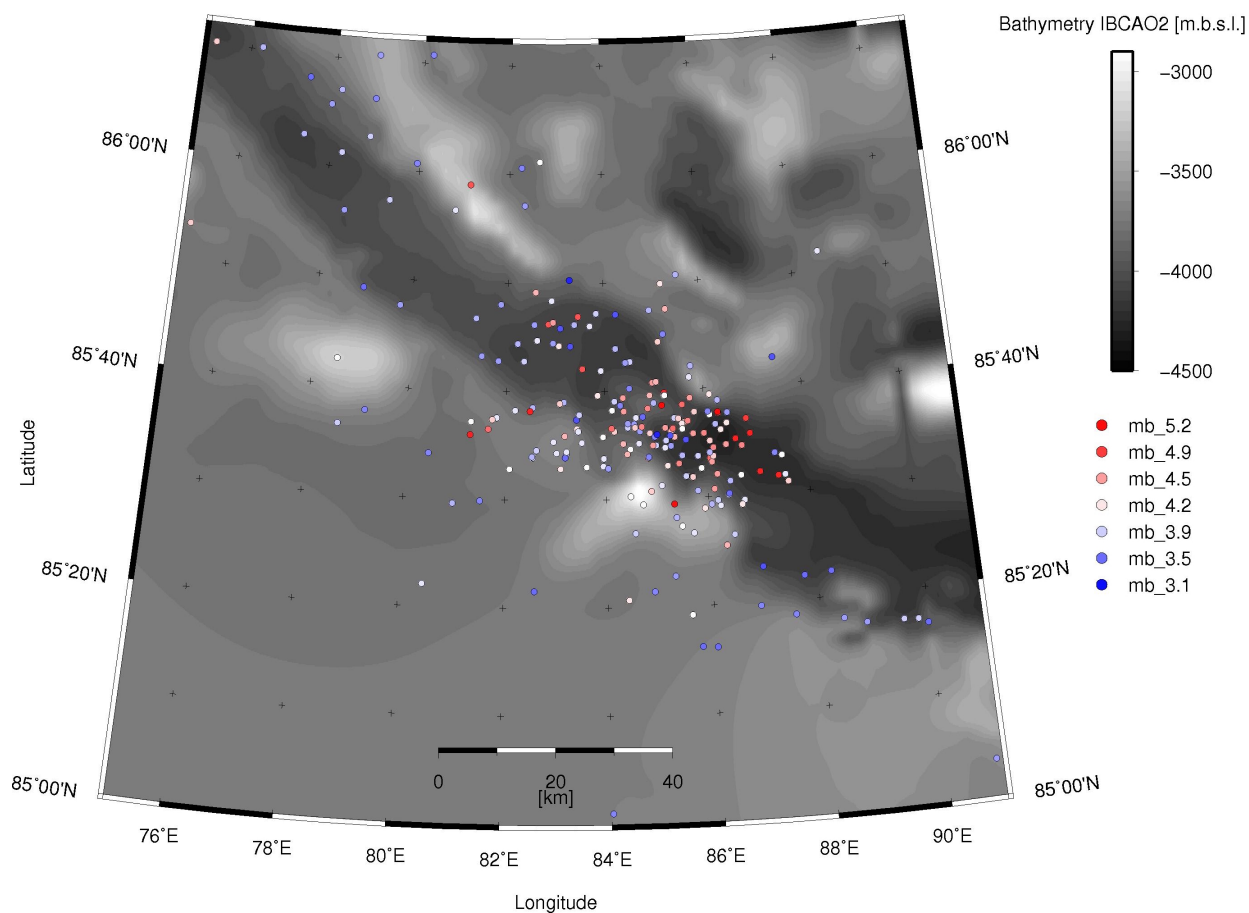


Figure 3.2: Localization of the 1999 earthquake swarm by ISC (reviewed bulletin), 252 events

3.2 Constraints on Dataset, Localization Parameters, Velocity Model

3.2.1 Testing of Dataset

For a baseline I localized the complete dataset with NonLinLoc only with the global AK135 velocity model, without further refinements like a local velocity model or additional weighting (Fig. 3.3). As initial number of cells searched through by the Grid-Search parameter LOCSEARCH OCT for the maximum of the PDF I accepted provisionally the recommended standard values 96 48 6 for the x-,y-,z-number of initial cells. In this figure I also color-coded the localized events by the number of phases which were used for localization.

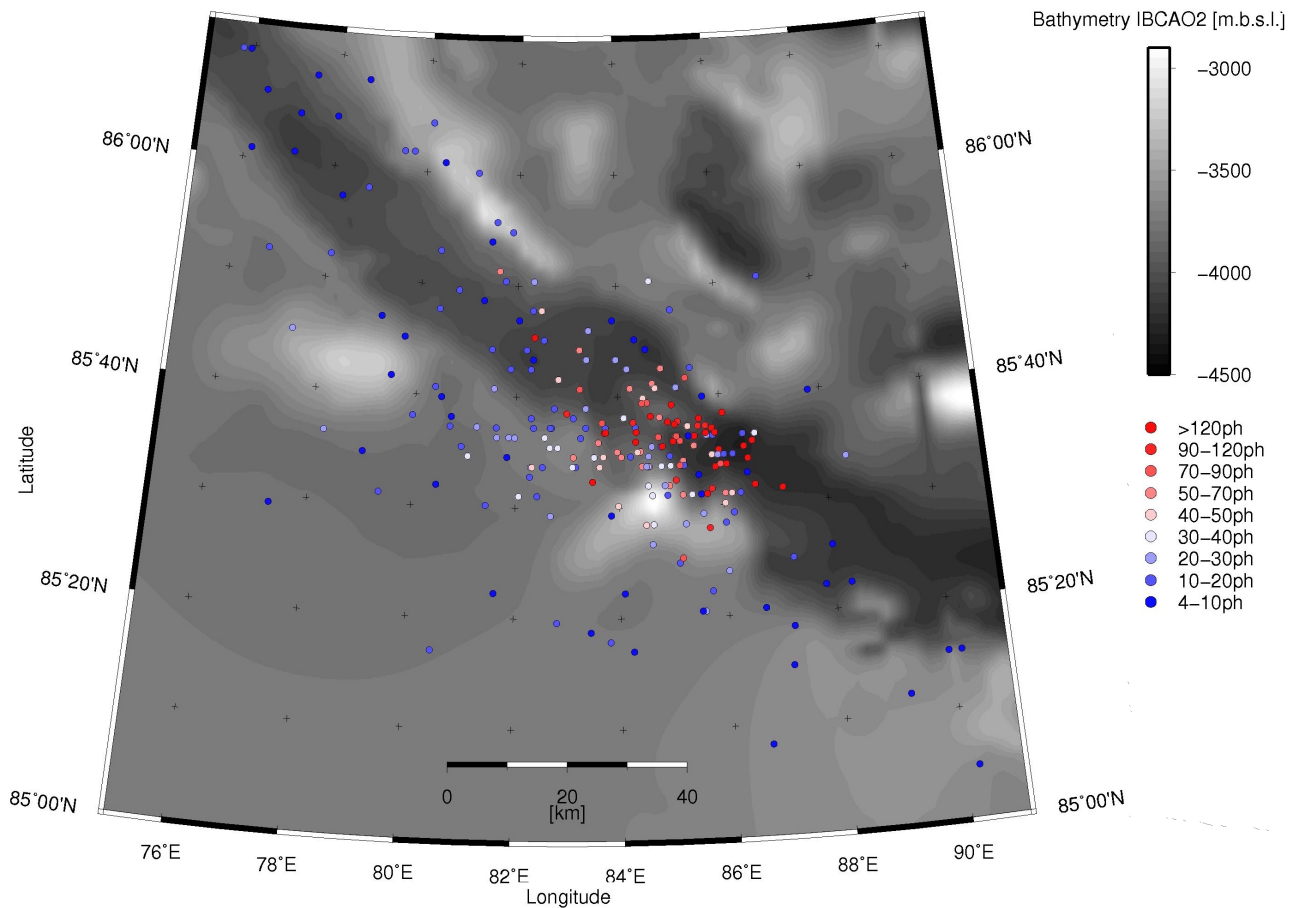


Figure 3.3: Baseline NonLinLoc localization of the 1999 earthquake swarm using AK135 (*Kennett et al., 1995*) as a global velocity model. The colors refer to the number of phases used in localization.

The baseline localization of 250 events yields an average RMS of 1.33 sec varying from 0.04 sec to 8.75 sec , the scattervolume of individual events also varies within six orders of magnitudes between 10^2 km^3 for the best constrained events to 10^8 km^3 for the worst as a result of large differences in the quality and quantity of the raw data of each individual event.

For the testing of the dataset and subsequently of the localization parameters I have relied on Gaussian-error parameters and the volume of the final scattercloud as it is not imperative here to localize the events with best possible accuracy, but rather to identify parameters which characterize a dataset that can be relied upon to give epicenters not controlled by data-inherent low quality. Picking I have assumed to be only flawed by Gaussian errors as all events have been reviewed by the ISC (*ISC*, 2008) already before being released in the comprehensive bulletin and hence I did not personally check picks on each individual recorded phase.

To test how the localization responds to the different qualities inherent in the raw data as displayed in number of registered phases and azimuthal coverage of registering stations I restricted the data to pertinent parameters and localized subsequently with the recommended standard values LOCSEARCH OCT 96 48 6.

3.2.1.1 Epicentral Coverage

For testing of epicentral coverage I compiled a homogeneous dataset for the 11 $m_b \geq 5$ events (Tbl. 3.2) which consisted only of recording stations present in all 11 events. For the homogeneous dataset, the actual number of registered phases differs somewhat throughout the events, however only P- and S-waves were used during the actual localization. The recording station farthest away was BGCA with about 83° epicentral distance. The complete homogeneous dataset was assumed to be well located which is supported by a small average RMS of 1.1 sec as well as small scattervolumes in the order of 10^3 . Event number 2984484 did not localize in the 85°E region and was hence excluded from testing.

Subsequently I curtailed the dataset such that only stations with an epicentral distance $\leq 30^\circ$, $\leq 40^\circ$ and $\leq 50^\circ$ were used during localization (Tbl. 3.3). This limits the quality of the dataset, but it simulates poorly observed earthquakes with a small number of registered phases in the near-field, allowing to constrain the effect a small number of phases (i.e. small magnitudes) has on the localization.

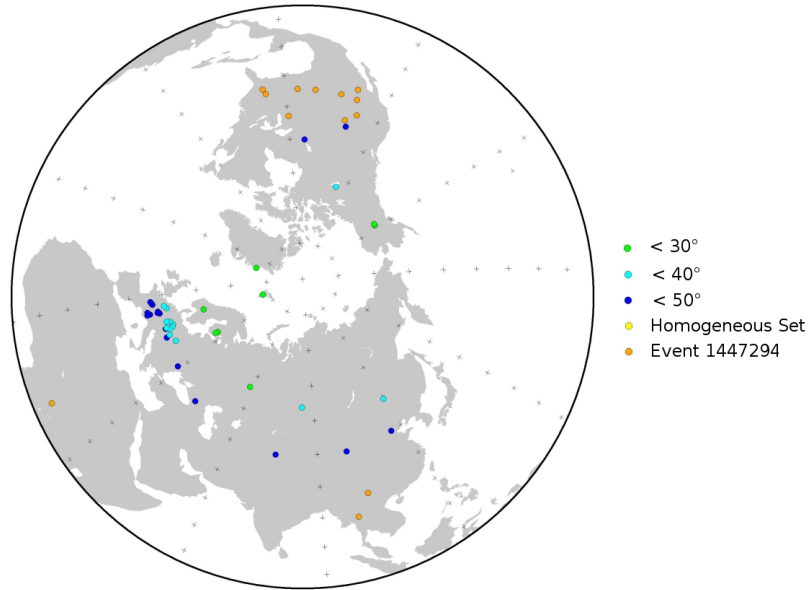


Figure 3.4: Distribution of stations for the curtailed datasets. At the wider datasets, all stations from more curtailed dataset are used in localization too. Included also was an exemplary event (event 1447294) for the full phase readings of an $m_b \geq 5$ event.

A skewing of epicenters to the southwest in the order of about 20 km while using the $\leq 30^\circ$ dataset in comparison to the localization of the complete homogeneous dataset is obvious as the curtailing truncates the cluster of European stations as well as nearly all American stations which could counteract the remaining number of stations mainly located in northern Europe. The visual distribution of epicenters is diffuse, southwesterly of the rift valley.

Date	Hr:Min	Event No	Registered Phases	Max. epicentral distance ($^\circ$)
1999/02/01	04:52	2982550	246	83.94 $^\circ$
1999/02/01	09:56	2982575	262	83.86 $^\circ$
1999/02/01	11:56	2982587	325	89.69 $^\circ$
1999/02/19	19:10	2984270	226	83.99 $^\circ$
1999/03/13	01:26	2993307	382	83.83 $^\circ$
1999/03/21	15:24	2994081	290	83.92 $^\circ$
1999/04/01	10:47	3011289	280	83.97 $^\circ$
1999/04/26	13:20	3013722	259	83.41 $^\circ$
1999/05/18	20:20	3048797	269	83.91 $^\circ$
1999/06/18	19:47	3095662	360	83.90 $^\circ$

Table 3.2: Original dataset of events with $m_b \geq 5$

Date	Hr:Min	Event No	Full Homogeneous Set	$\leq 50^\circ$	$\leq 40^\circ$	$\leq 30^\circ$
1999/02/01	04:52	2982550	59	46	24	9
1999/02/01	09:56	2982575	60	47	27	11
1999/02/01	11:56	2982587	62	49	29	11
1999/02/19	19:10	2984270	54	43	23	10
1999/03/13	01:26	2993307	66	53	29	13
1999/03/21	15:24	2994081	59	47	25	11
1999/04/01	10:47	3011289	58	47	24	10
1999/04/26	13:20	3013722	60	50	28	11
1999/05/18	20:20	3048797	61	48	27	11
1999/06/18	19:47	3095662	66	52	30	13

Table 3.3: Homogeneous dataset with number of phases used during localization

Using the $\leq 40^\circ$ dataset, the epicenters are still skewed to the southwest but by a lesser amount, some are displayed at the southern rift valley walls. As a magnitude $m_b = 4.1$ earthquake is located using on average 31 phases (Tbl. 3.1), this roughly equals the effect a limit in recording stations of $\leq 40^\circ$ epicentral distance has on the localization.

The $\leq 50^\circ$ dataset in comparison to the complete homogeneous dataset is finally collectively located within the central rift valley, although also about 5 km southwestwards.

The difference in curtailed epicenter location (complete homogeneous dataset, $\leq 83^\circ$ epicentral distance) to the actual localization (all available phases, minimum 106° epicentral distance) of the 11 events can be said to be a shifting of epicenters to the southeast in the order of 5-10 km.

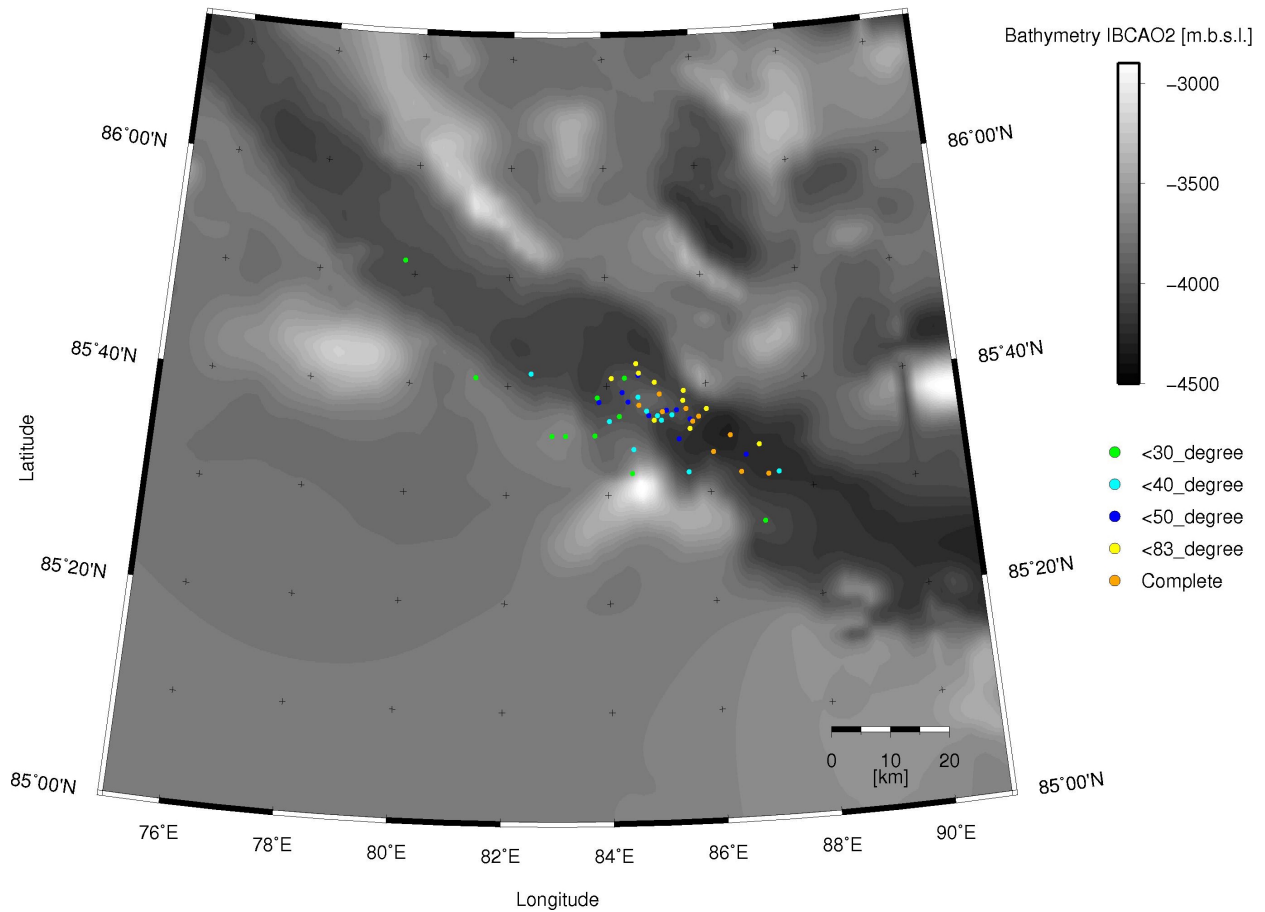


Figure 3.5: Comparison of the location of $m_b \geq 5.0$ earthquakes using phase datasets truncated in different epicentral distances.

In conclusion, a limited number of phases with only relatively near recording stations in one direction of the globe can severely distort the localization of the epicenter. For the $85^\circ\text{E}/85^\circ\text{N}$ region this corresponds to a shifting of epicenters to the southwest. Small events localized at the rift flanks may also be skewed, with the true locations within the central rift valley. Therefore all events with $m_b \leq 4.2$ or less than 50 phases have to be evaluated very carefully for their epicentral coverage before accepting the epicenters as the true event location. In addition it is advisable to review the final dataset with regard to the maximum epicentral distance as events with less than 50° epicentral coverage are likely shifted to the southeast.

3.2.1.2 Azimuthal Coverage

The testing of the azimuthal distribution of recording stations utilizes the maximum azimuthal gap between stations. I used two datasets which were compiled from the complete set of 252 events: the first set containing all events with a number of registered phases ≤ 30 (154 events) which I presume to be poorly constrained as indicated by the analysis of the homogeneous, 40° -constrained dataset. The second set includes all remaining events with > 30 phases used in localization (96 events).

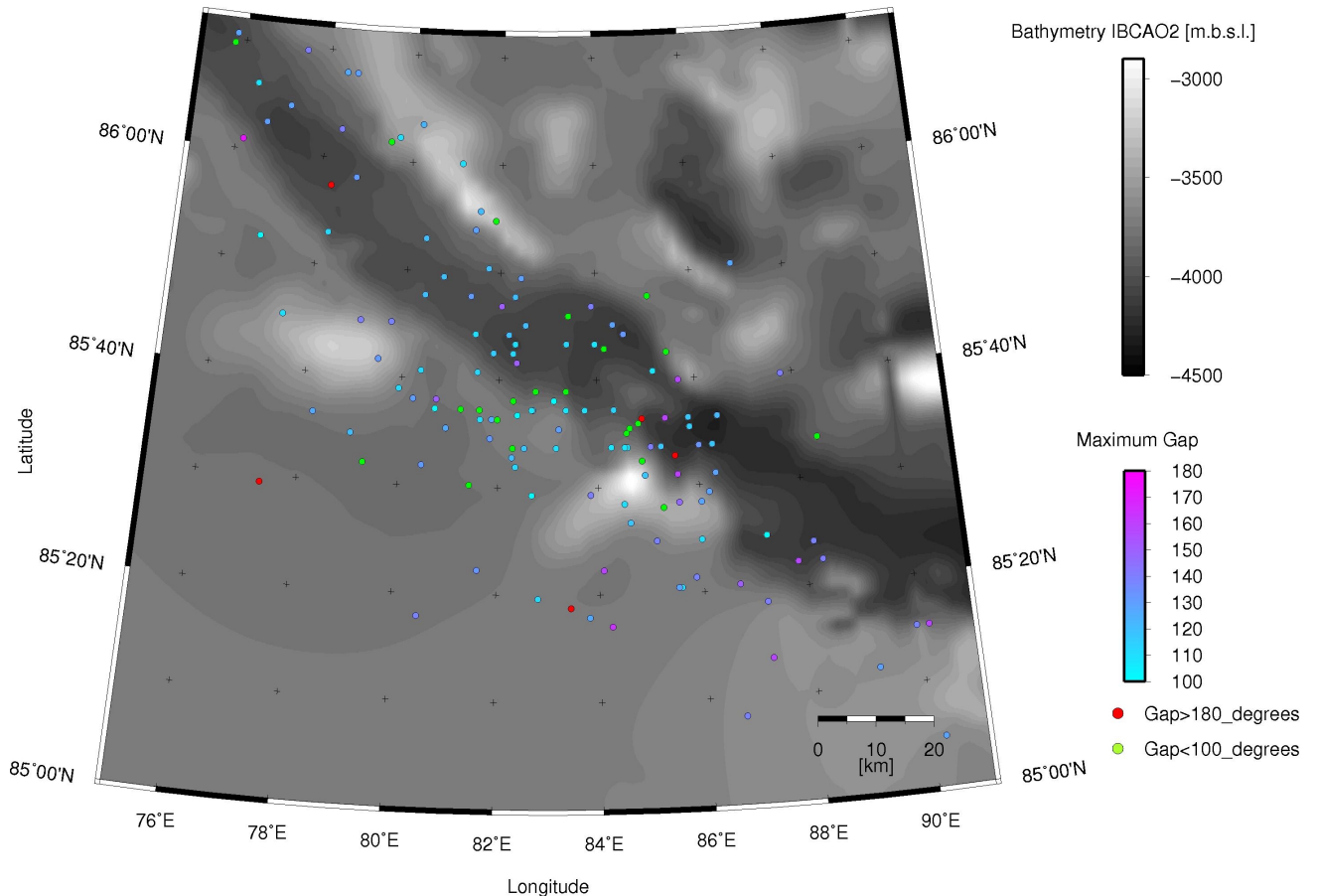


Figure 3.6: Azimuthal coverage, events with ≤ 30 registered phases.

Within the poorly constrained dataset (Fig. 3.6), only 23 events have a maximum gap less than 100° . Of these, three events display high scatter volumes ($\geq 10^5 \text{ km}^3$) and cannot in the following be considered to be reliably located. Of the remaining subset of 20, the best 5 events have up to 83.135° epicentral coverage. For these events the mean scatter volume is nevertheless high with $2.5 \cdot 10^4 \text{ km}^3$, the mean RMS amounts to 1.43 sec. The remaining 18 events cover $\leq 80^\circ$ epicentral distance.

Events with high gap $\geq 160^\circ$ tend to locate scattered southeast of the volcanic region except for the worst events with $\geq 180^\circ$ gap which are distributed widely and also display ≤ 10 phases used for localization. The southwesterly scattering of events with smaller maximum gaps of $\leq 160^\circ$ can be attributed to the small number of phases.

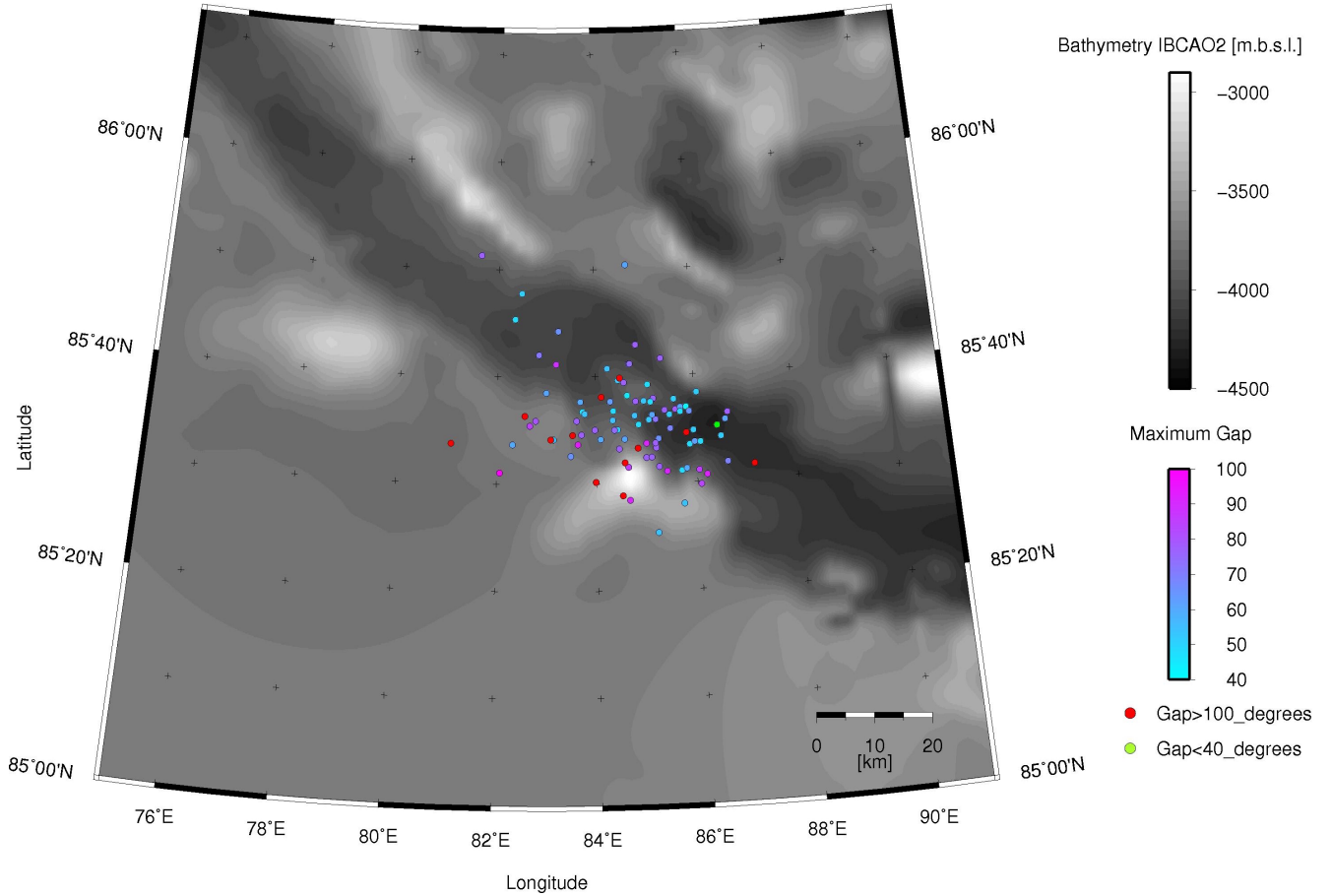


Figure 3.7: Azimuthal coverage, events with > 30 registered phases.

The dataset with events > 30 registered phases (Fig. 3.7) displays a concentration of events with relatively high maximum gaps $\geq 90^\circ$ at the southern rift valley wall. The number of phases used in localization for these events does not exceed 46. Events with small maximum gaps $\leq 60^\circ$ cluster within the central rift valley or locate at or very near the southern rift valley wall. A majority of these events were localized with more than 60 phases, only three events used less.

In summary, a high azimuthal gap $\geq 160^\circ$ can cause a shifting of epicenters in the southeastern direction. The southwesterly shifting of events beyond the southern rift valley walls is likely induced by the small number of phases ≤ 46 . Events with more than 50 phases used for localization are therefore likely to have small maximum gaps $\leq 90^\circ$. They predominantly cluster within the central rift valley.

3.2.2 Testing of Localization Algorithm

3.2.2.1 Search for Maximum of the PDF - Variation in Initial Number of Cells

The grid search algorithm Oct-Tree (LOCSEARCH OCT) systematically divides a grid into ever finer eight cells which are then evaluated for the value of their PDF in the center of each single cell. The best cell is then used as a starting point for the next iteration, giving an importance sampling of the PDF with a high density of cells in areas of a higher value of the PDF.

In global mode the grid spans the whole earth, oriented along the meridians. I set two parameters for termination of grid-search: First, a minimum node size of 0.01° (x,y) / 0.01 km (z) as the smallest grid cell to search for the maximum of the PDF and secondly a maximum number of 100,000 nodes to divide. The criterium for the maximum number of nodes cuts in when the initial grid is too coarse, causing the localization to be incorrect as it aborts the search for the maximum too soon. When a greater initial number of cells is chosen the search for the maximum of the PDF is terminated when the grid cells become smaller than the defined minimum cell size. This would yield correct epicenters.

For detecting an optimal starting number of cells for the whole dataset I varied the LOCSEARCH OCT parameter for 144, 96 (standard), 48, 23, 16 and 1 initial grid-cells in x-direction. The number of cells in y- and z-direction was adjusted accordingly. To get an idea how poorly constrained events react to the Oct-Tree search method, I tested with the dataset of events with ≤ 30 phases used in localization (Fig. 3.8) and subsequently with the better constrained homogeneous dataset to minimize distorting effects from epicentral- and azimuthal distribution (Fig. 3.9).

For the poorly constrained dataset the visually observable longitudinal arrangement of epicenters for each initial number of OCT cells (Fig. 3.8) (e.g. only comparing epicenters in blue with each other) is probably caused by the linear subdivision of cells in the process of searching for the pdf. Generally it seems as most epicenter-variations are arranged from northwest to southeast.

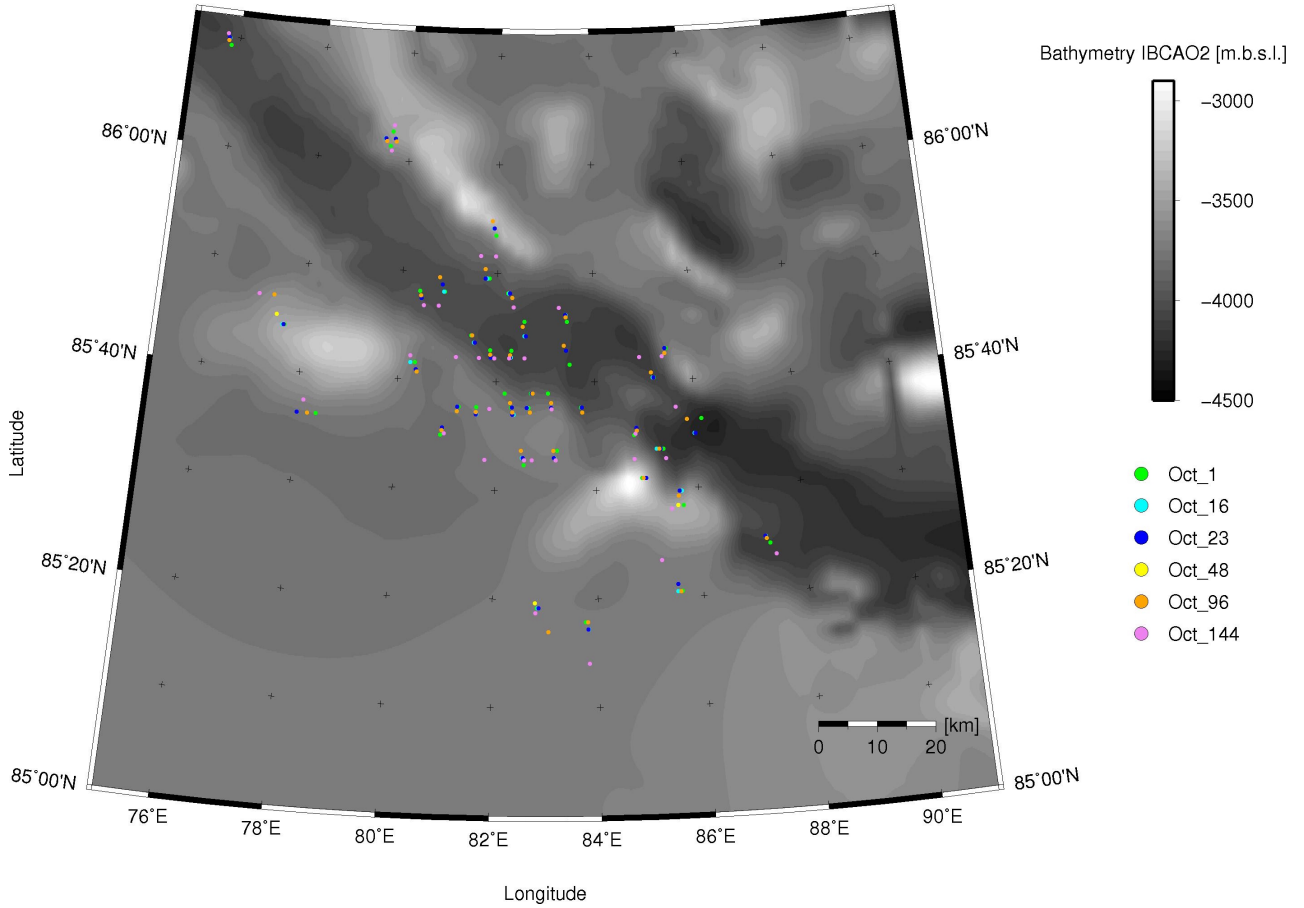


Figure 3.8: Variation in initial number of cells for OCT-tree algorithm, events with ≤ 30 registered phases.

For the homogeneous dataset with about 60 phases used during localization (Fig. 3.9) for each event (Tbl. 3.3), the starting number of cells scarcely makes a difference to the calculation of the epicenter (inlay of Fig. 3.9). A visual evaluation shows that OCT 1 almost always lies at the fringe of the epicenter distribution. OCT 48 lies mostly very near OCT 96. Both mostly seem to designate the center of mass of the epicenter distribution within the homogeneous dataset. The differences in epicentral location do not exceed about 2 km.

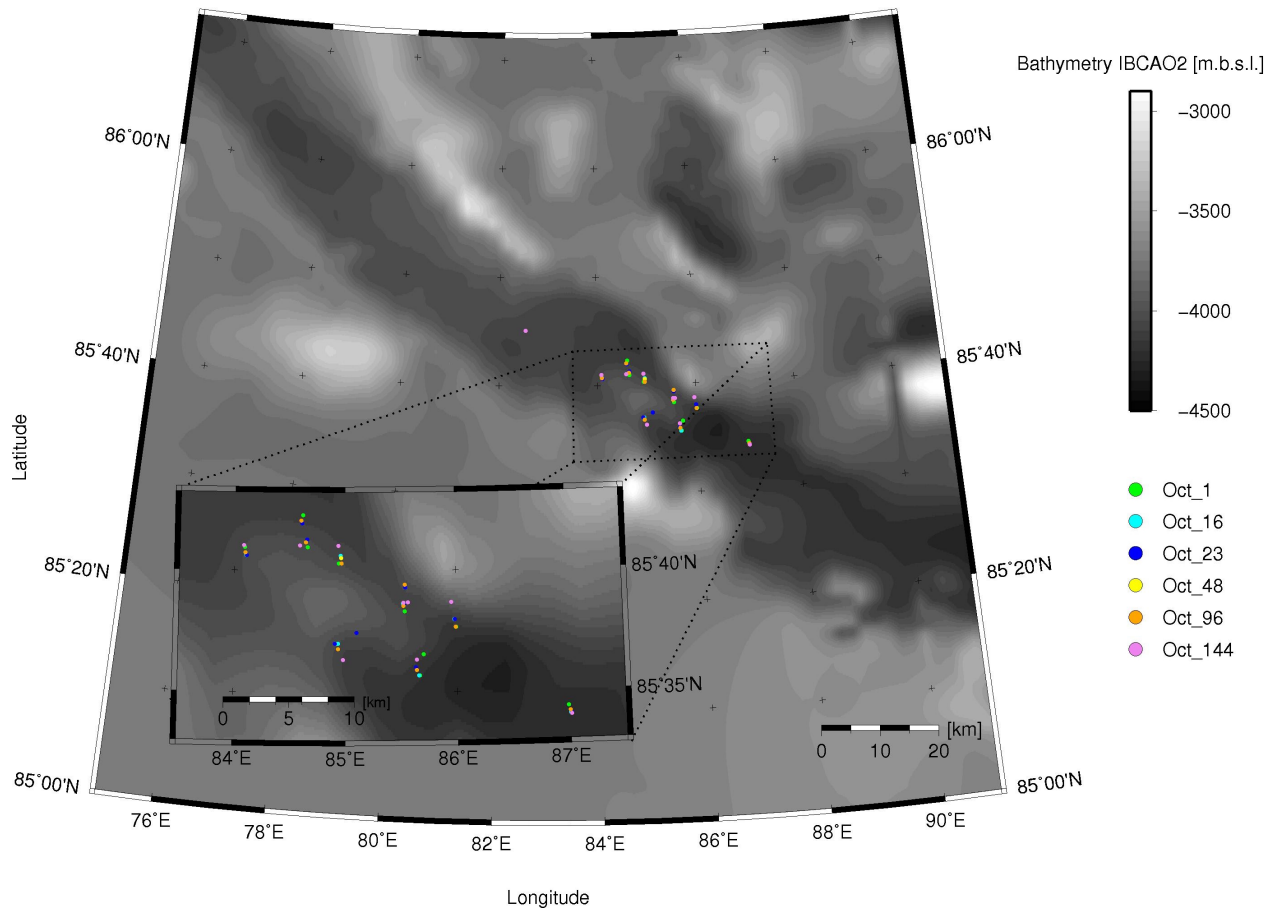


Figure 3.9: Variation in initial number of cells for OCT-tree search, homogeneous dataset.

For choosing an optimal initial cell-number for the whole dataset I plotted the mean RMS and the mean scattervolume for both datasets (≤ 30 phases used in localization as well as homogeneous dataset) (Fig. 3.10 and Fig. 3.11):

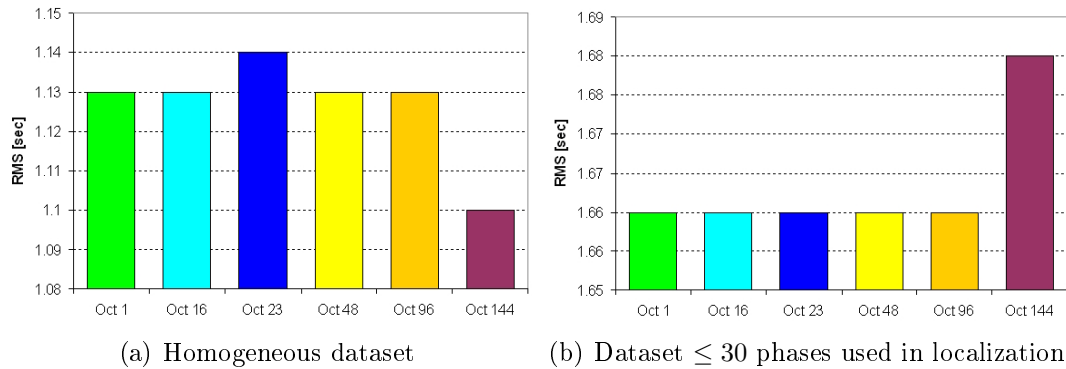


Figure 3.10: Variations in initial cell-number with different datasets as displayed by the mean of RMS [sec].

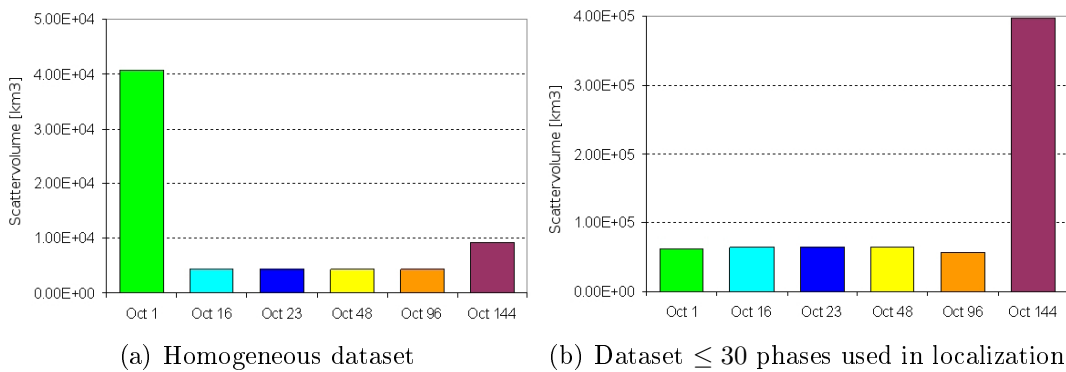


Figure 3.11: Variations in initial cell-number with different datasets as displayed by the mean of the scattervolume [km³].

For the ≤ 30 dataset OCT 96 has a slightly smaller mean of scattervolume than the other starting number of cells. Within the homogeneous dataset no distinction is observable between OCT 16, OCT 23, OCT 48 and OCT 96. To finally choose an optimal starting number of cells I exclude OCT 1 and OCT 144 as both have high scattervolumes. OCT 23 disqualifies by the slightly elevated mean RMS for the homogeneous dataset. From the lack of distinctive characteristics within the remaining numbers, I chose OCT 96 as optimal parameter on the basis of visual observation (it designates the center of mass within the homogeneous dataset) as well as the slightly smaller value within the ≤ 30 dataset.

3.2.2.2 Testing of Weighting Station Clusters

For the calculation of the posterior probability density function, LOCMETH provides the equal-differential times likelihood function (EDT) (Zhou, 1994), which is weighted by the variance of the origin-time estimates over all pairs of readings (EDT_OT_WT). This reduces the impact of outliers in the data and provides in effect a weighting of readings during location. Within LOCMETH I also defined the minimum number of 4 phases which have to be accepted before localization.

NonLinLoc also provides the means to weight station readings relative to the average distance between all pairs of stations as control mechanism for station clustering (LOCSTAWT). In order to constrain the effect of local station clusters (i.e. european stations) on the localization I used LOCSTAWT with the mean distance between all station-pairs as cut-off distance. I applied this weighting to two datasets, the first with events with less than 30 phases used in localization (Fig. 3.12), secondly only events with ≥ 30 phases used in localization as an indicator of the reaction of better constrained events (Fig. 3.13).

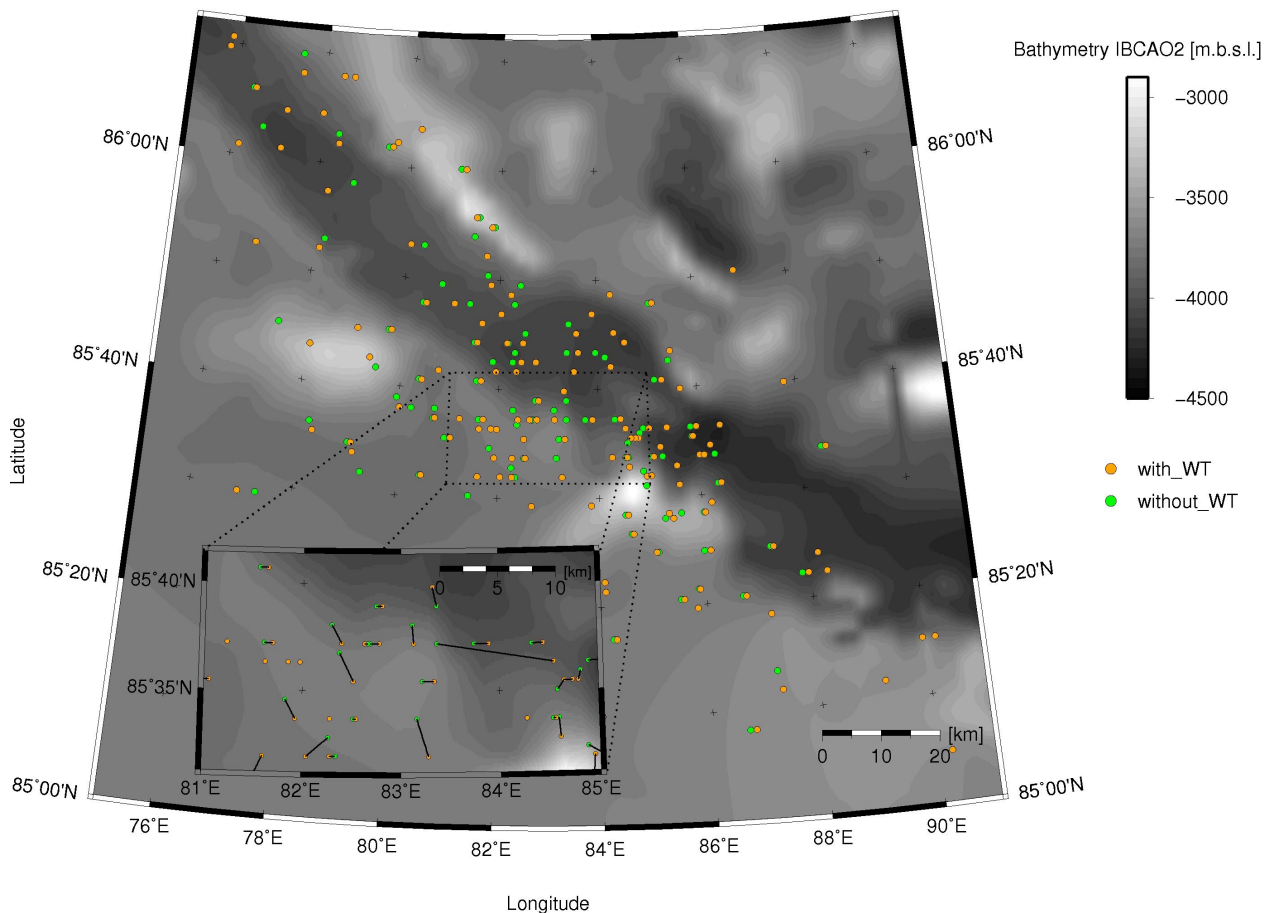


Figure 3.12: Influence of weighting algorithm on events < 30 phases used in localization.

Only some of the epicenters in the less constrained dataset show a prominent difference in location caused by the weighting algorithm (Fig. 3.12). The lack of difference between the weighted and unweighted results for the remaining events may be caused by such a low number of recording stations that no spatial station clusters exist in the dataset.

For the well constrained events (Fig. 3.13) the lack of significant epicentral difference may be caused either by the effectiveness of the weighting algorithm EDT_OT_WT used in calculation of the final PDF or by the high number of balancing phases which downweight the influence of station clusters.

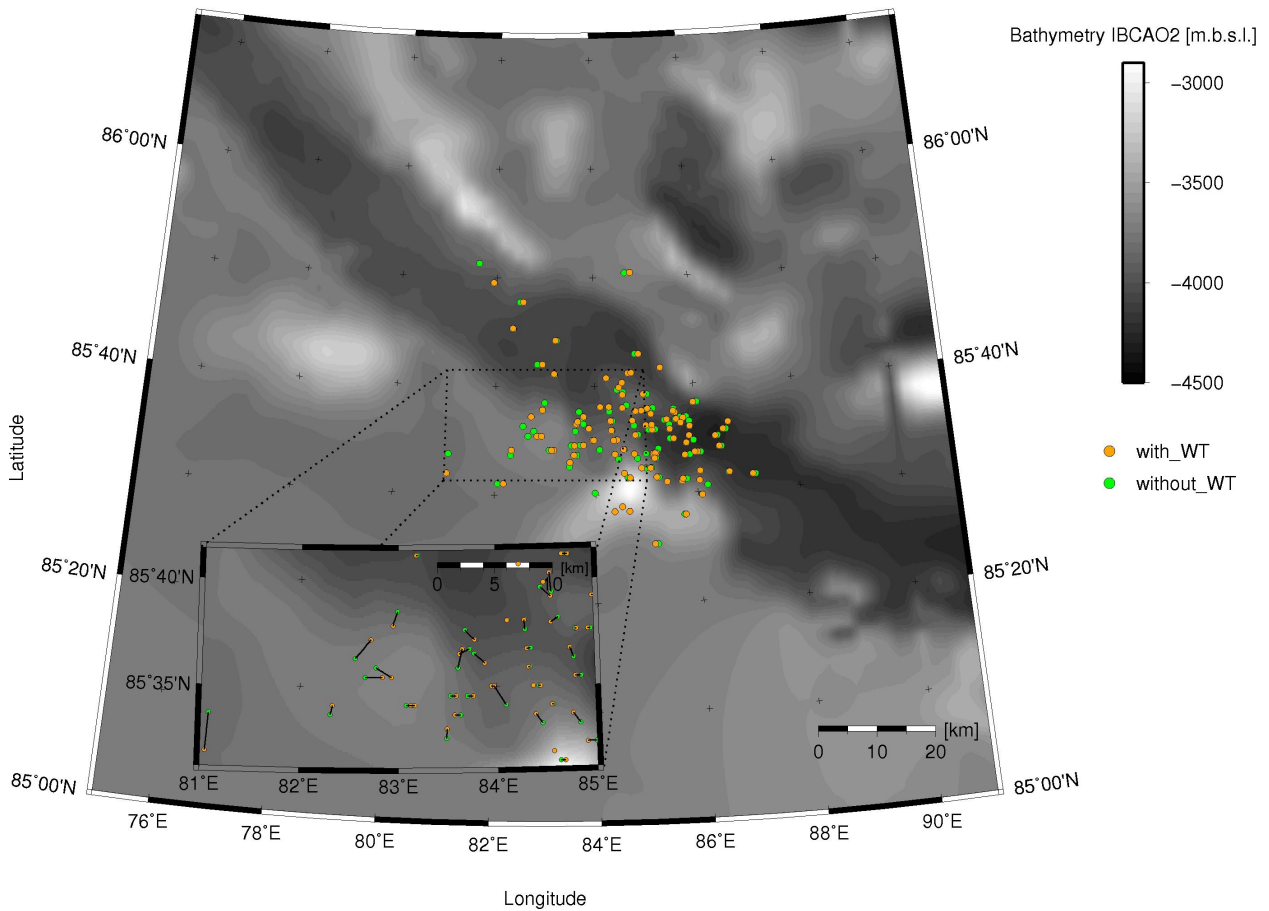


Figure 3.13: Influence of weighting algorithm on events with ≥ 30 phases used in localization.

This also expresses itself through the difference in scattervolumes between the unweighted and the weighted set (Fig. 3.14). The mean scattervolume of the less constrained dataset is slightly better for the weighted set, indicating that a localization including weighting does work a bit better, however the scattervolume does not significantly drop. For the better constrained set no difference in mean scattervolume is observable at all.

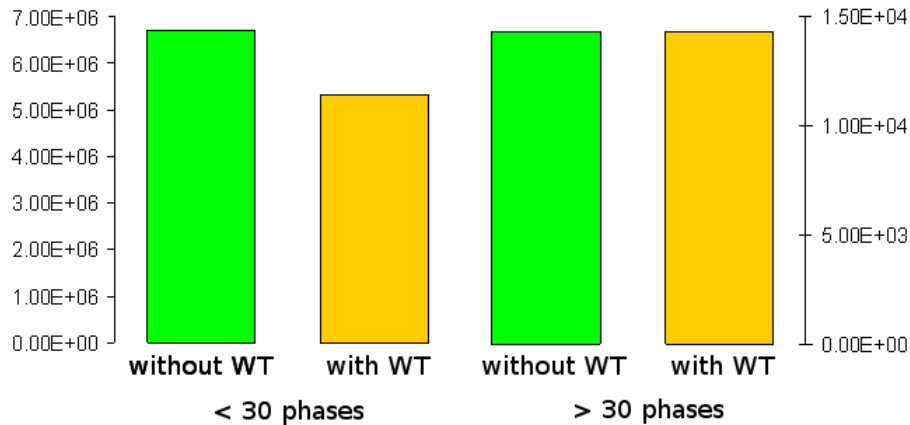


Figure 3.14: Influence of weighting algorithm expressed through scattervolume [km³] of datasets for < 30 and ≥ 30 phases used in localization.

In conclusion, the weighting algorithm provided by NonLinLoc LOCSTAWT does not significantly influence the calculation of epicenters, not even if the events are not well constrained.

3.2.3 Testing of Global- and Local Velocity Model

For teleseismic earthquake localization NonLinLoc uses the whole earth as grid for the calculation of traveltimes. I implemented the AK135 velocity model (*Kennett et al., 1995*) (Fig. 3.15) for global traveltimes calculation.

As required by *Tarantola and Valette (1982)* NonLinLoc uses a gaussian error matrix for the model error inherent in the traveltimes tables. It is built up of a typical error of the traveltimes to a station (LOGGAU) and an exponential factor dependent on the distance between any two stations. I have set the typical error LOGGAU to 1 sec.

An additional traveltimes error gives the parameter LOGGAU2, which specifies a fraction of the traveltimes with a set minimum and maximum error. It can be thought of as a picking error or an additional station-distance weighting. I have used 0.01 as the fraction of the traveltimes to be used, 0.05 sec as minimum error and 2 sec as maximum error. These are standard values.

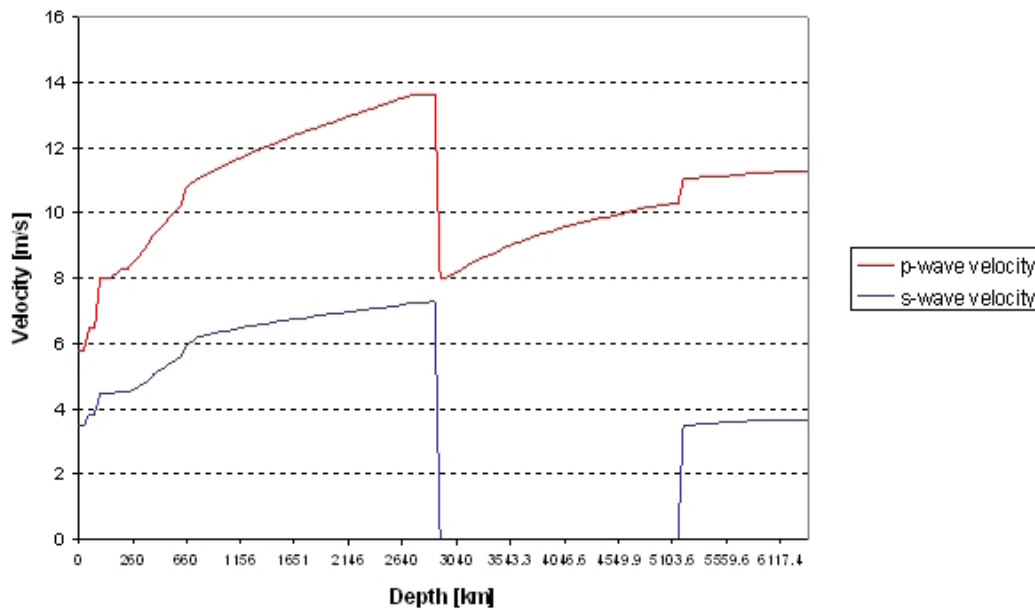


Figure 3.15: AK135 global velocity model (*Kennett et al., 1995*)

For stations near the hypocenters, rays sample for longer stretches the shallow structure of the oceanic crust and upper mantle. *Riedel and Schlindwein (2009)* compiled a velocity model (Fig. 3.16) from the teleseismic dataset of 1999 which fitted the phase observations of nearer stations best. In their model, the Mohorovicic Discontinuity is assumed to begin at 10 km with further 6 km of gradually increasing velocity. Deeper structures than 660 km were supplemented by the AK135 model (*Kennett et al., 1995*).

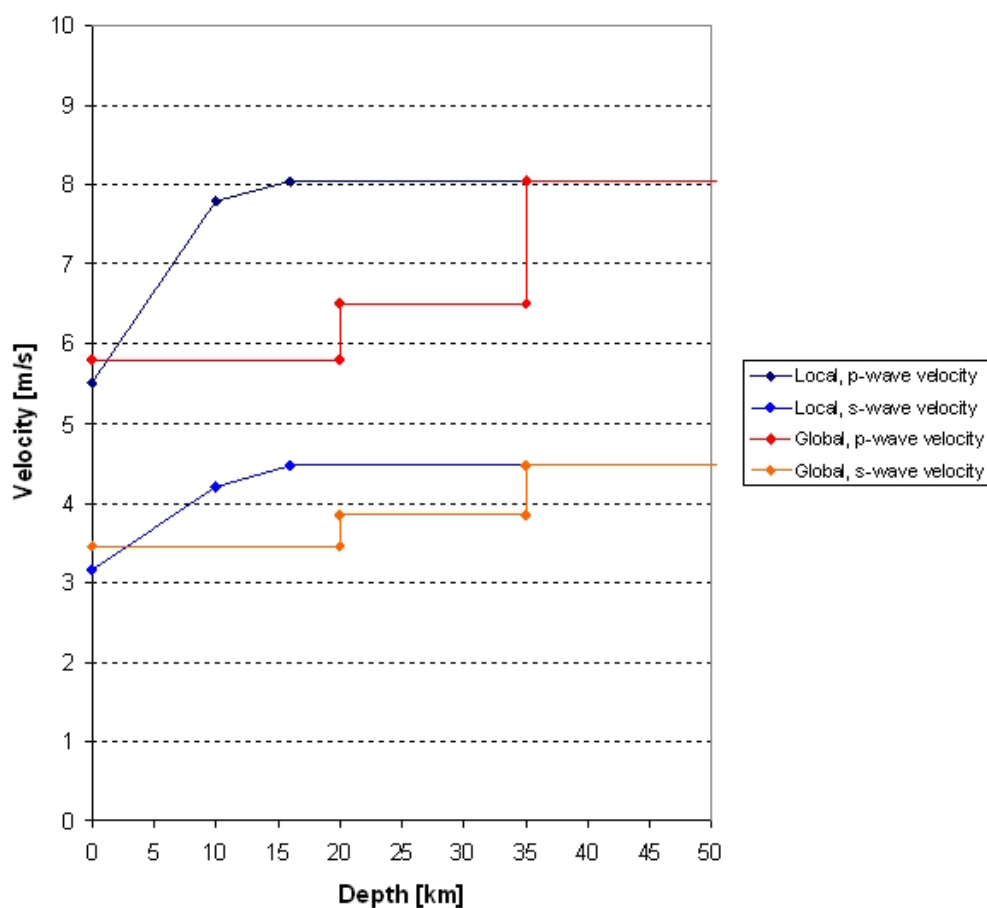


Figure 3.16: Differences between the global AK135- and the local velocity model compiled by *Riedel and Schlindwein (2009)*

I used this regional velocity model for stations near the hypocenter with about $< 30^\circ$ epicentral distance as rays from the earthquake focus travel through the crust and shallow mantle to these stations. Rays to more distant stations leave the source area subvertically down and are not affected by differences between the regional velocity model and the global model.

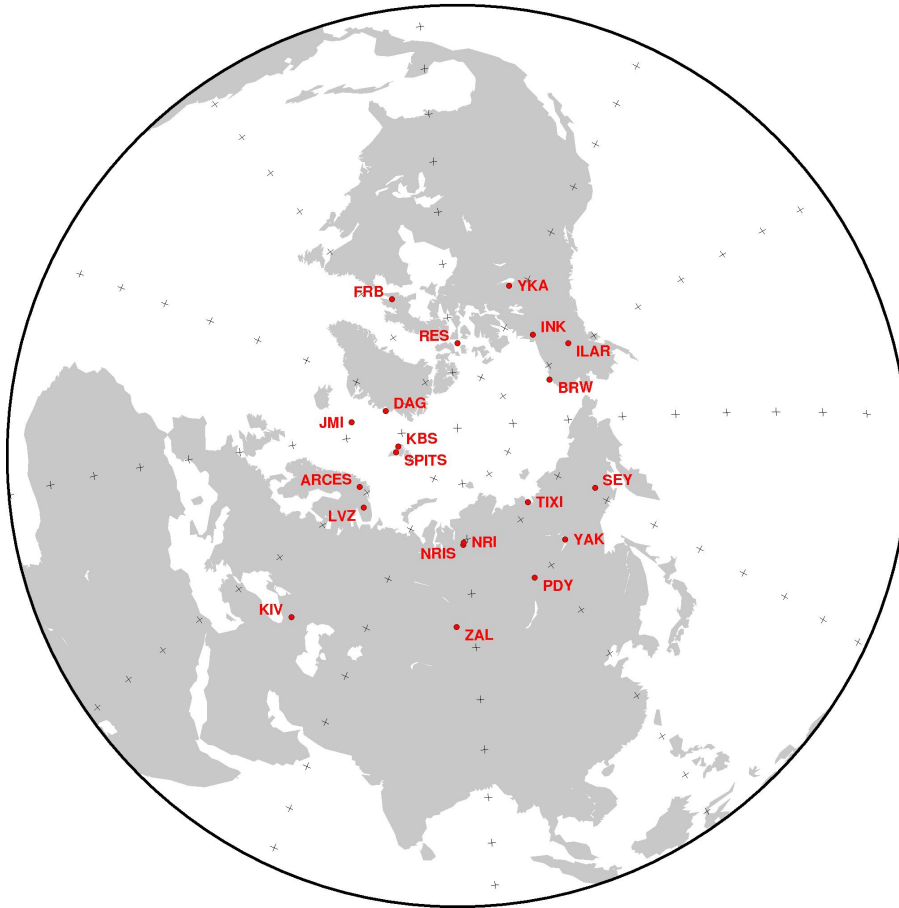


Figure 3.17: Recording seismometers near the 85°N volcanic complex for which the regional velocity model is used. Lambert azimuthal projection, center of map is at $85^\circ\text{N}/85^\circ\text{E}$.

To test the impact the use of a regional velocity model has on the calculation of epicenters I investigated the epicentral variation for different datasets, namely for < 30 , ≥ 30 phases used in localization and for events with $m_b \geq 5$.

The use of the regional velocity model has the largest impact on the poorly constrained events with < 30 registered phases (Fig. 3.18), where the epicenters vary widely in the order of more than 10 km, mostly along axis as a consequence of geographical station distribution.

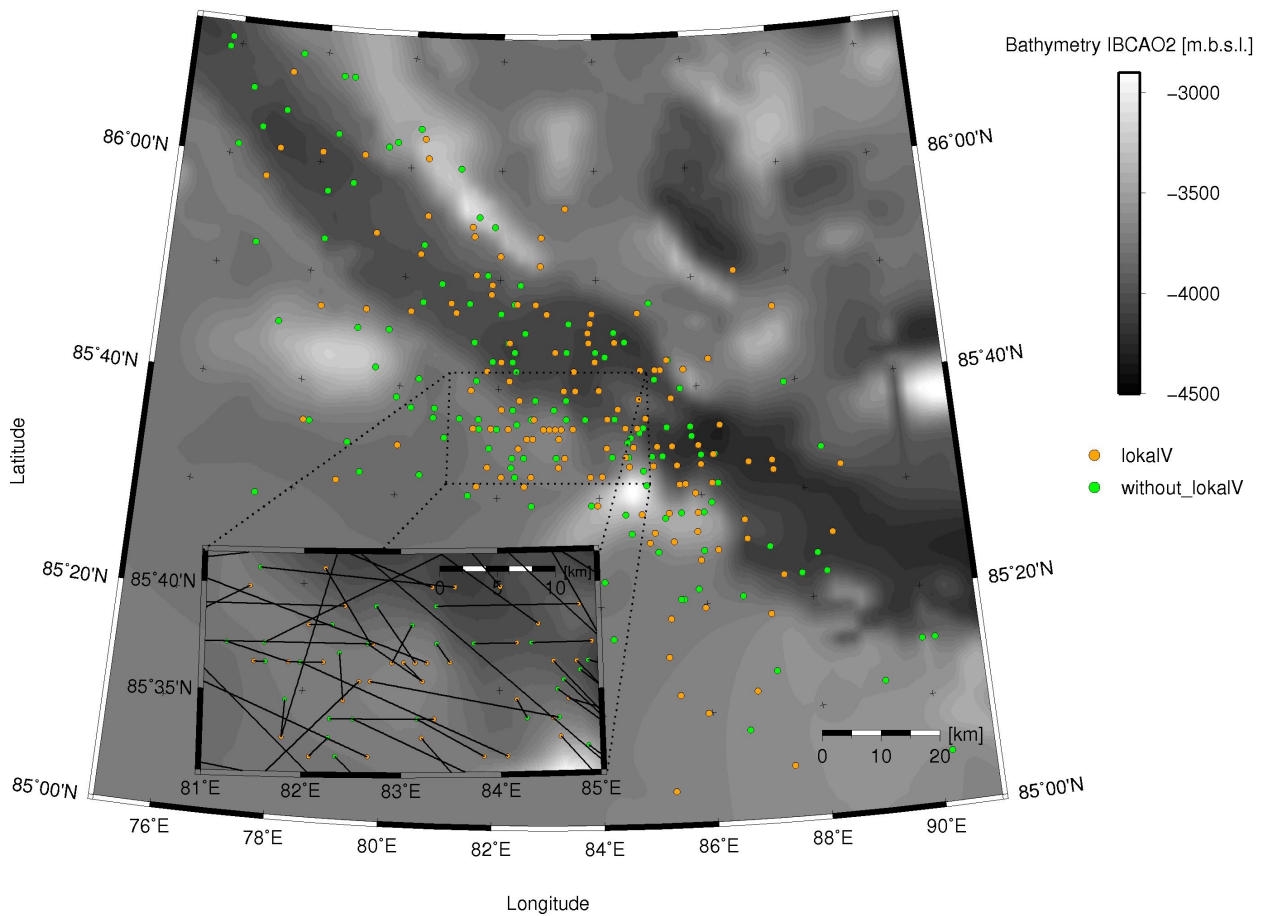


Figure 3.18: Localization with use of the local velocity model for near-stations, ≤ 30 registered phases.

For better constrained events with ≥ 30 registered phases the variation is less pronounced, the difference in epicenters mostly does not exceed 10 km. This dataset is inhomogeneous for the range of phases used in localization is great. Nevertheless, I calculated the mean scattervolume for both datasets (Fig. 3.19), finding that the mean scattervolume for the well-constrained dataset calculated while using the local velocity model is less by a measurable amount than if only using the global velocity model.

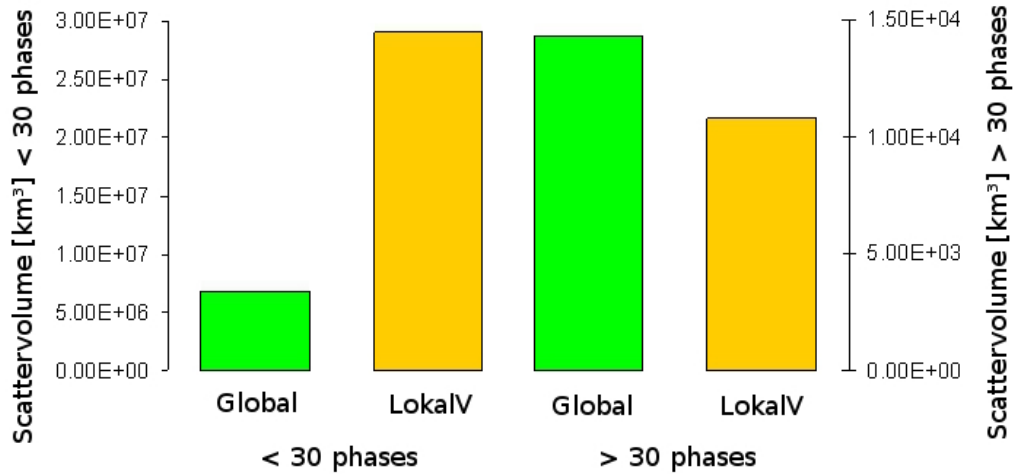


Figure 3.19: Influence of the use of an local velocity model, expressed through scattervolume [km³] of datasets for < 30 and ≥ 30 phases used in localization.

For the less constrained dataset, the localization without the use of a local velocity model is much better, though these events probably will not be interpretable due to their high scattervolumes ($> 10^6$ km³). For events with the highest number of phases used in localization (10 events with $m_b \geq 5$) I investigated additionally if the usage of a local velocity model changes the epicenter locations significantly (Fig. 3.20).

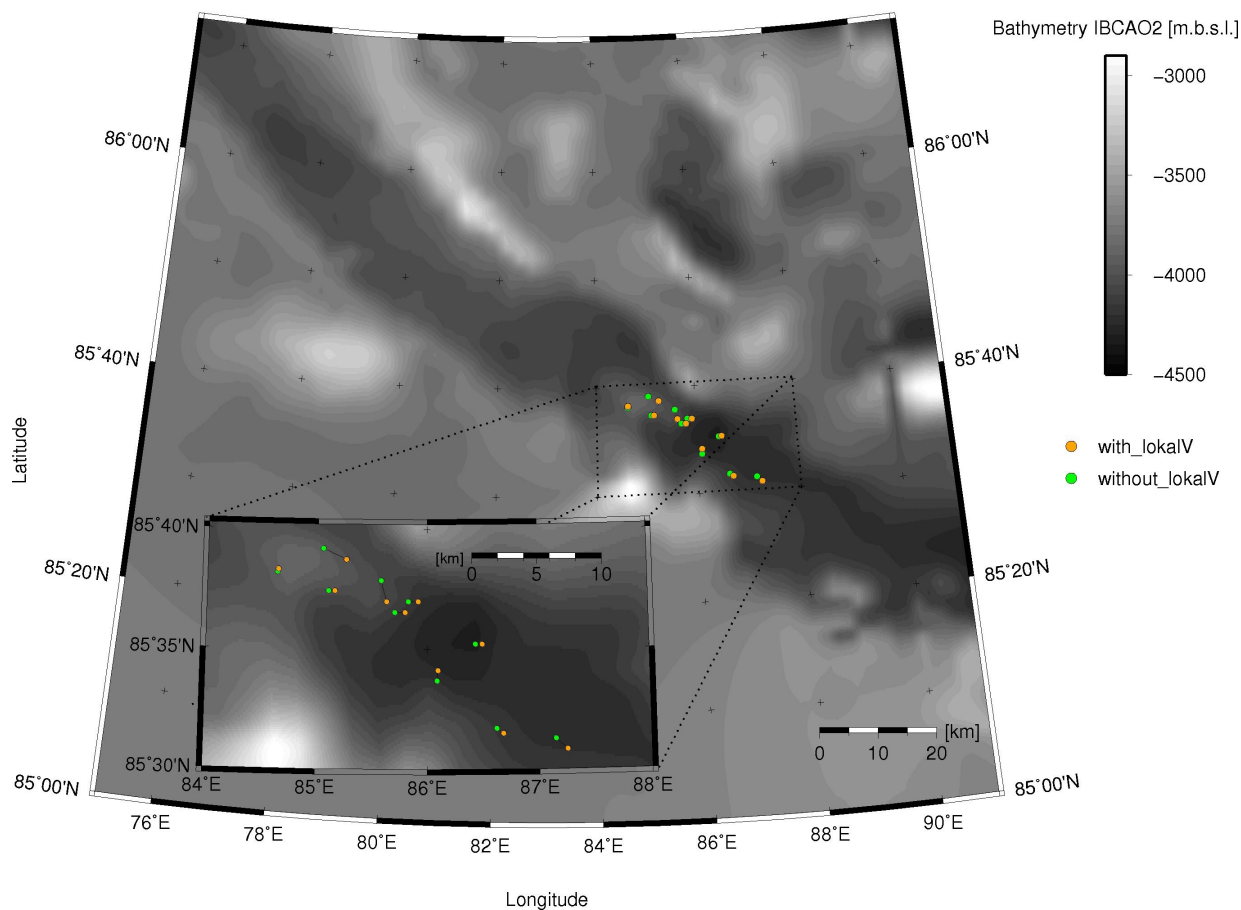


Figure 3.20: Localization with use of the local velocity model for near-stations, events with $m_b \geq 5$.

For this well constrained dataset the differences in epicenters with and without local velocity model are negligible with the greatest shift in epicenters amounting to 2.6 km.

In conclusion the use of a regional velocity model for the 85°E/85°N region only influences the localization of epicenters for events with a small number of registered phases, varying the locations depending on which near-stations registered.

Chapter 4

RESULTS of the Non-Linear Relocalization and of Uncertainties

I localized the complete dataset of 252 events in NonLinLoc global mode with the oct-tree searching routine using 96 starting cells in longitudinal direction and the corresponding 48 starting cells in latitudinal direction and 6 cells downwards for depth. AK135 (*Kennett et al.*, 1995) was used as a global velocity model (Fig. 3.15) and a local velocity model (Fig. 3.16) was applied to selected stations (Fig. 3.17). Additionally, outliers were downweighted with the weighting algorithm EDT_OT_WT.

In the final localization only 2 events (Event 2508777 on 1999-01-29: $m_b = 3.3$, and event 2582814 on 1999-02-20: $m_b = 3.4$) could not be localized as they have only three phases which were potentially usable for localization. Fig. 4.1 shows the location of the 250 localized events. However, the hypocenters are widely differing in quality and therefore have to be evaluated very carefully.

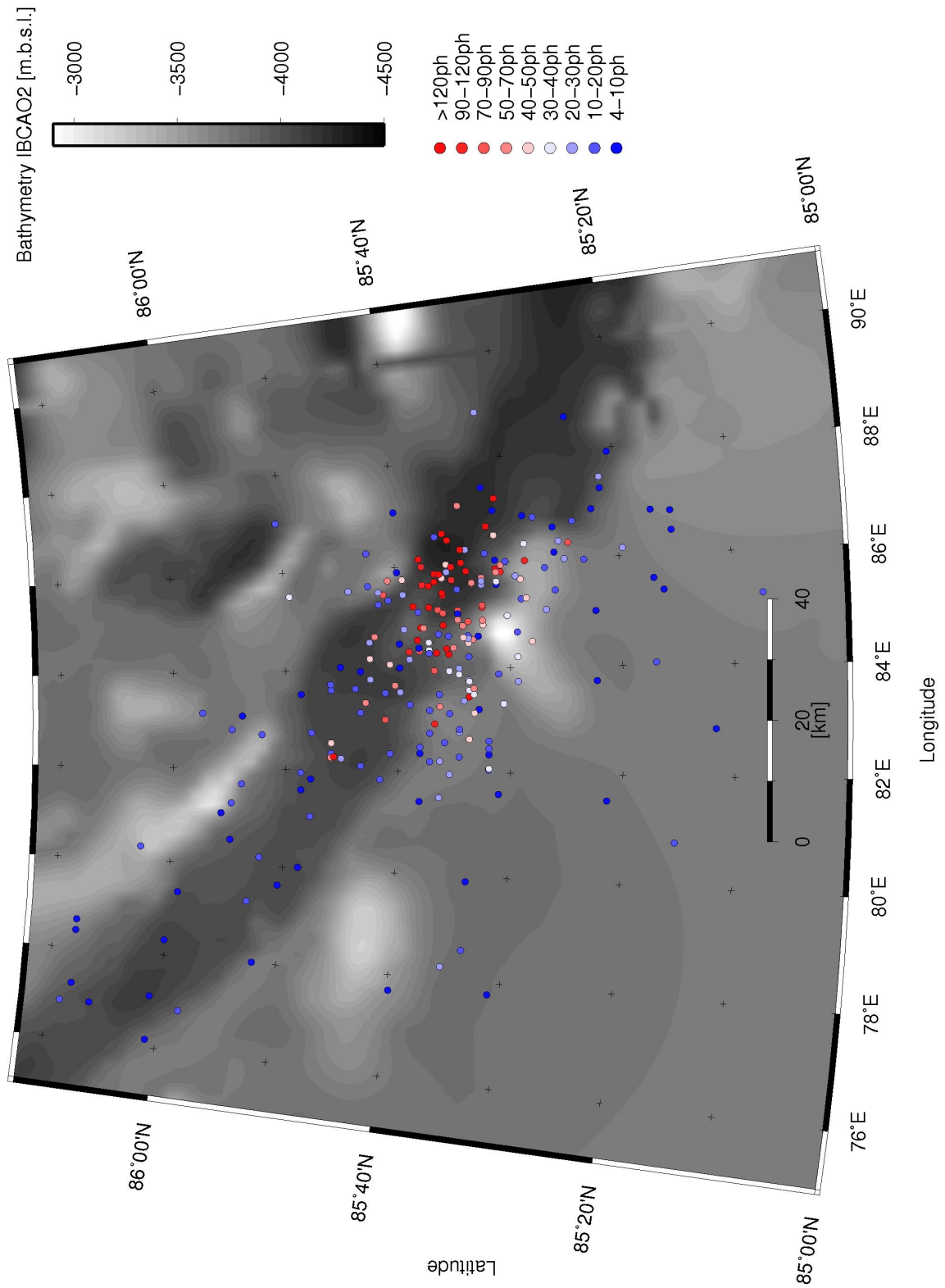


Figure 4.1: Overview over final localized dataset, 250 events

4.1 Quality of Swarm Relocation

For **general evaluation** two qualities have to be taken into account:

1. The quality **inherent in the raw data:**

The events show different epicentral- and azimuthal distributions of phase recordings. The epicentral distribution is quantified by the maximum number of phases and the maximum distance between recording station and epicenter. The azimuthal distribution is expressed through the maximum gap.

2. The quality of the **localization itself:**

For stochastic quality evaluation NonLinLoc calculates the scattervolume which designates the volume which is defined by the scattersamples of the normalized PDF. It provides the covariance matrix which then can be manipulated with single-value decomposition to give the 68.5% confidence ellipsoid with length- and orientation of error-ellipse semi-axes.

However, the final scattervolume may be arbitrary in appearance and hence the error-ellipsoid may not fit the scattercloud. In this case, the difference between the Gaussian expectation hypocenter which is obtained from the covariance matrix, and the maximum likelihood location is a good indicator of the misfit (called in the following DIFFLON/DIFFLAT). If the difference is large and the final visualized scattercloud is non-ellipsoid in appearance, then the 68.5% error-ellipse as calculated by the covariance matrix does not give an accurate error estimate.

Shown below are two examples, first a good fit of the error-ellipsoid as demonstrated by event **19990201.045512** (Fig. 4.2), secondly an example of a bad fit in event **19990204.185416** (Fig. 4.3). For the latter event on February, 4th 1999 the expectation hypocenter seems to be calculated correctly but the error-ellipsoid is not well fitted to the scattercloud. However this does not influence the final analysis, as I will only interpret events which are localized reliably. The quality parameters of these two exemplary events are summarized in Tbl. 4.1.

Event ID	19990201.045512	19990204.185416
Number of phases:	246	39
Scattervolume:	$1.48 \cdot 10^3 \text{ km}^3$	$4.18 \cdot 10^4 \text{ km}^3$
Error-ellipsoid Semi-Axis (Major):	5.42 km	19.89 km
Error-ellipsoid Semi-Axis (Minor):	5.09 km	10.8 km
DIFFLON:	0.019°	1.275°
DIFFLAT:	0.0011°	0.0820°
RMS:	1.308 sec	1.248 sec

Table 4.1: Quality parameters for exemplary events.

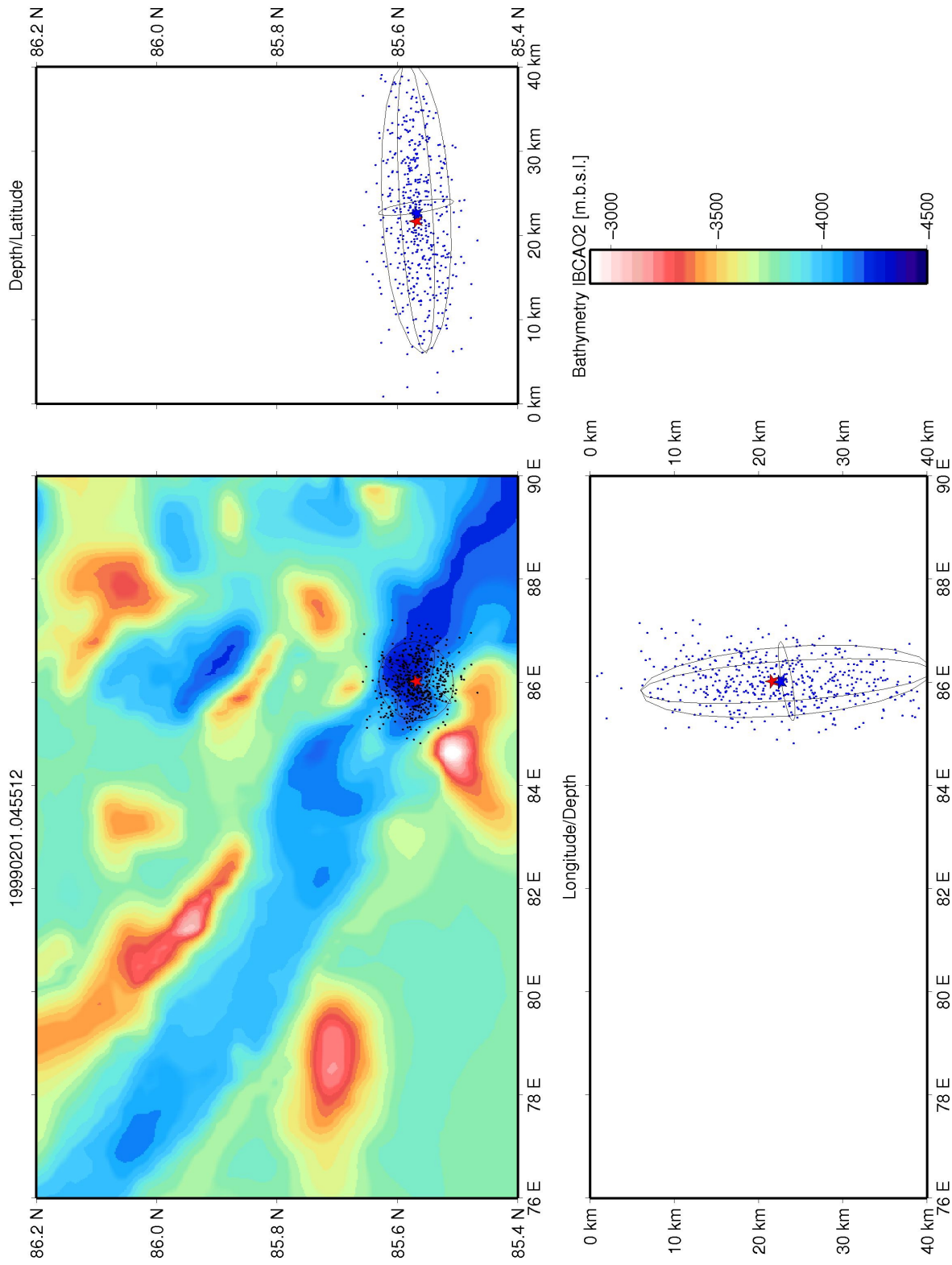


Figure 4.2: Example of a good fit of the error-ellipsoid to the scattercloud, demonstrated by event 19990201.045512. The red star indicates the maximum likelihood hypocenter, the blue star the expectation hypocenter.

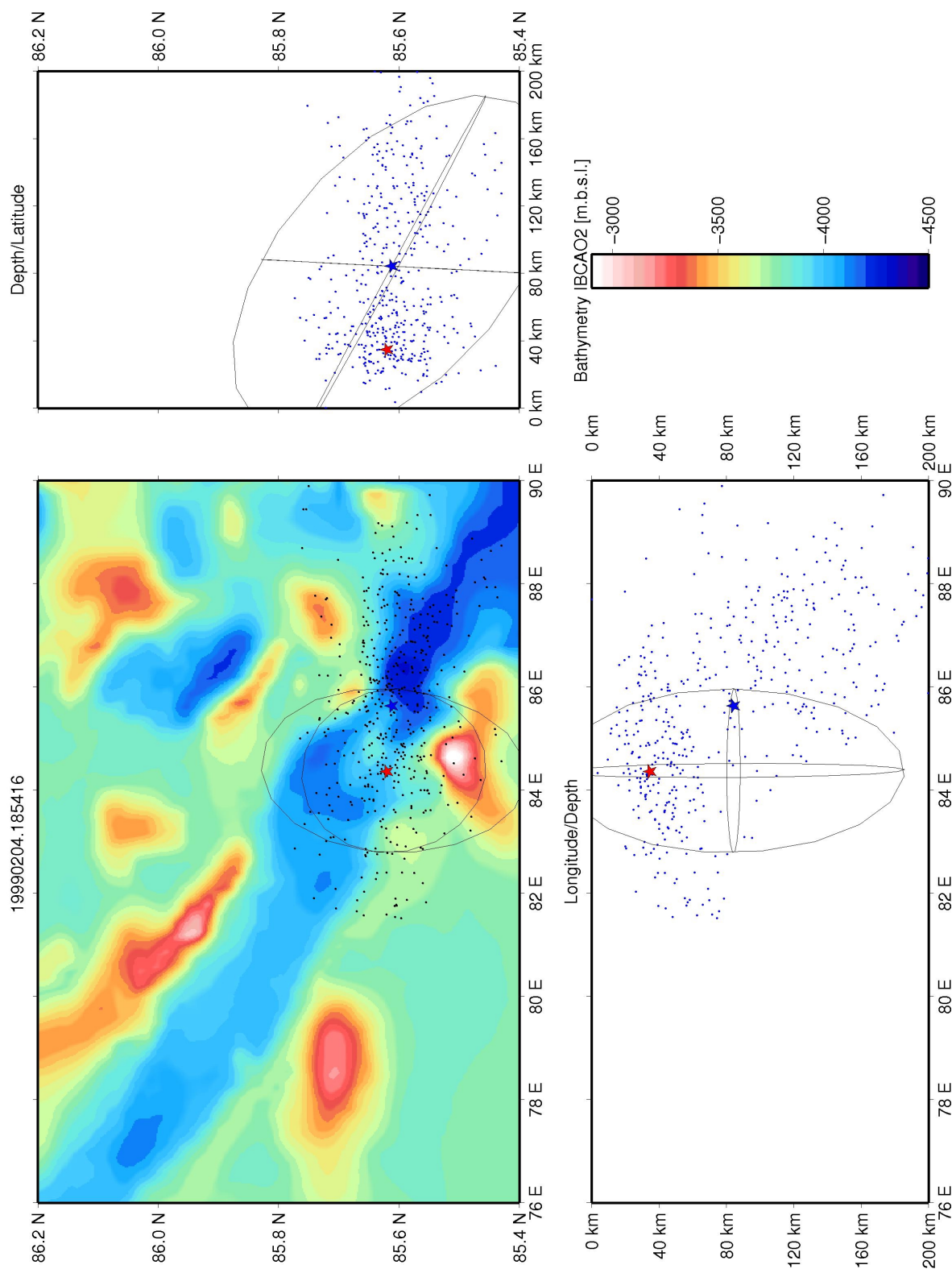


Figure 4.3: Example of a bad fit of the error-ellipsoid to the scattercloud, demonstrated by event 19990204.185415. The red star indicates the maximum likelihood hypocenter, the blue star the expectation hypocenter.

For judging consistently the quality of the individual events I first had to review the **overall quality of the final dataset**. To this end I calculated the minimum- and maximum values for epicentral- and azimuthal coverage. For RMS and scattervolume I additionally calculated the median and the mean (Tbl. 4.2):

Parameter	Median	Mean	Minimum	Maximum
Number of phases:	20	49	4	382
Maximum Epicentral Distance:			13.41°	161.27°
Maximum Gap:			32.78°	350.29°
RMS:	1.212 sec	1.219 sec	0.152 sec	6.893 sec
Scattervolume:	$3.27 \cdot 10^4 \text{ km}^3$	$1.97 \cdot 10^7 \text{ km}^3$	$1.56 \cdot 10^2 \text{ km}^3$	$1.76 \cdot 10^9 \text{ km}^3$

Table 4.2: Range of quality for the overall dataset

A median of 20 phases used in localization means that 50% of all events have more than 20 phases useable in localization and are localized with a scattervolume of $\leq 3.27 \cdot 10^4 \text{ km}^3$. Regarding the values for RMS and scattervolume, I tested if the minimum- and maximum-value events for both parameters intercorrelate (Tbl. 4.3). Comparing these events in RMS and scattervolume and including their number of phases used in localization as an independent indicator of epicentral coverage, I find a high number of phases used in localization for a minimum scattervolume and a small number of phases used in localization for a maximum scattervolume, pointing to the scattervolume as a good quality indicator. This does not hold true for the RMS, however. Here I get very small numbers of phases used in localization for minimum- and for maximum RMS and no distinguishing difference between the scattervolumes of minimum and maximum values of RMS. This suggests that the scattervolume is subsequently a more reliable quality indicator than the RMS.

	RMS	Event ID	Phases	Scattervolume
Min RMS:	0.152 sec	2995077, 1999-03-31	4	$6.45 \cdot 10^7 \text{ km}^3$
Max RMS:	6.893 sec	2984076, 1999-02-17	17	$1.22 \cdot 10^5 \text{ km}^3$
	Scattervolume	Event ID	Phases	RMS
Min Scattervolume:	$1.56 \cdot 10^2 \text{ km}^3$	2993307, 1999-03-13	382	1.232 sec
Max Scattervolume:	$1.76 \cdot 10^9 \text{ km}^3$	2614123, 1999-03-05	4	0.407 sec

Table 4.3: Minimum and maximum values for RMS and scattervolume

To get a dataset which can be analysed conclusively I need reliable events through defining quality criteria for application to the final dataset.

4.2 Selection of Well-Constrained Events

For compiling a subset of well-located events I have decided to rely firstly on dataset inherent quality markers as in epicentral- and azimuthal coverage, and secondly on the NonLinLoc localization-dependent parameters. For epicentral- and azimuthal distance cut-off criteria I implemented the given limitations found in testing. The epicentral cut-off value of ≤ 50 phases used in localization corresponds to a minimum of 67° epicentral distance for the farthest recording station.

After implementation of the epicentral- and azimuthal distance cut-off criteria the remaining dataset of 65 events shows scattervolumes from $1.56 \cdot 10^2 \text{ km}^3$ up to $2.50 \cdot 10^4 \text{ km}^3$ with the first quartil at $2.03 \cdot 10^3 \text{ km}^3$. There is no obvious threshold within the scattervolumes of these events but the third quartil gives a value of $8.31 \cdot 10^3 \text{ km}^3$ which might make a cut-off criterium of $\leq 10^4 \text{ km}^3$ reasonable when compared to a first quartil of $2.70 \cdot 10^4 \text{ km}^3$ for events not included in this dataset.

The difference between expectation- and maximum-likelihood hypocenter in longitude and latitude shows a range of values for these 65 events up to a maximum of 0.479° for DIFFLON and 0.0358° for DIFFLAT. This corresponds to 4.02 km in longitudinal direction at 85° E and to 3.99 km latitudinal difference at 85.66° N . Both values lie within the error margin given by the minimum of the length of error-ellipsoid semi-axis (4.07 km for the semi-major axis), no further curtailing of the dataset seems necessary.

For further quality considerations I give length of semi-major axis of the error-ellipsoid precedence over RMS as this parameter may be distorted by the fitting of many phases to a hypocenter, giving a greater RMS if the event in question is actually better constrained.

Quality of the dataset:

Epicentral distance:	≥ 50 phases used in localization Farthest recording station at $\geq 67^\circ$ or farther
Maximum azimuthal gap:	$\leq 80^\circ$

Quality of the localization:

Scattervolume:	$\leq 10^4 \text{ km}^3$
DIFFLON / DIFFLAT:	$\leq 0.892^\circ$ / $\leq 0.0675^\circ$
Length of error-ellipse semi-major axis 2D:	$\leq 10 \text{ km}$

Table 4.4: Quality criteria in localization.

- For **Quality 1**, all criteria shown in Tbl. 4.5 had to be met rigorously. Included in this set is a cut-off criterium of 10 km for the semi-major axis of the error-ellipsoid adjusted for 2D as this corresponds roughly to half of the valley extension. 43 events fit this category.
- In **Quality 2** the remaining events with the same cut-off parameters but a greater length of semi-major axis number 10.
- A deviation of one order of ten within the scattervolume was tolerated within **Quality 3** if all other parameters, excluding the length of semi-major axis, were met. Further 10 events fit in this category.
- All remaining events which did not fit these criteria were given **Quality 5**.

The final well-located dataset which consisted of events included in Quality 1, 2 and 3 comprises a total of 63 events, which are located predominantly within the central rift valley and the southern rift flank (Fig. 4.4).

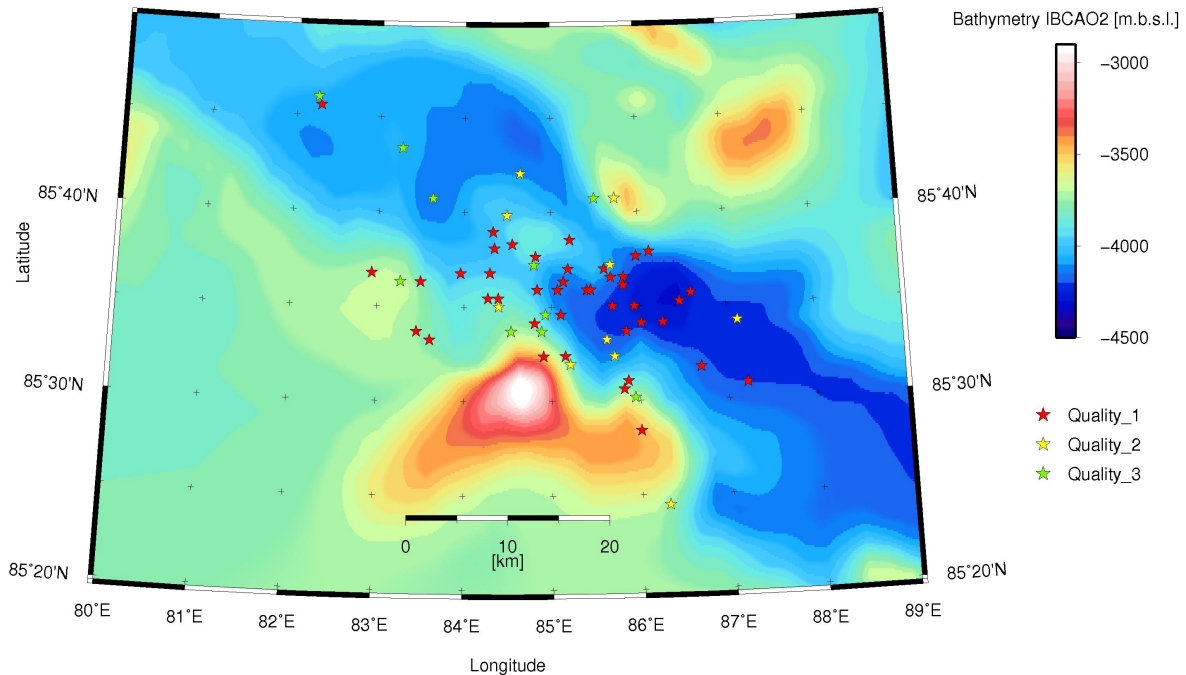


Figure 4.4: Final well-located dataset, 63 events

Value	Number of Phases	Δ	Γ	Scattervolume	DIFFLON	DIFFLAT	Length of semi-major axis
Average Q1	174	82.59 °	56.24 °	$3.32 \cdot 10^3 \text{ km}^3$	0.052 °	0.0038 °	7.18 km
Median Q1	147	83.75 °	53.16 °	$2.94 \cdot 10^3 \text{ km}^3$	0.037 °	0.0031 °	7.34 km
Average Q2	70	75.41 °	67.80 °	$7.64 \cdot 10^3 \text{ km}^3$	0.113 °	0.0052 °	11.8 km
Median Q2	68	75.73 °	73.06 °	$7.86 \cdot 10^3 \text{ km}^3$	0.089 °	0.0041 °	12.1 km
Average Q3	60	79.71 °	70.92 °	$1.37 \cdot 10^4 \text{ km}^3$	0.127 °	0.0075 °	14.4 km
Median Q3	59	83.10 °	77.11 °	$1.23 \cdot 10^4 \text{ km}^3$	0.083 °	0.0046 °	13.2 km
Average Q1+2+3	139	81.05 °	60.38 °	$5.65 \cdot 10^3 \text{ km}^3$	0.074 °	0.0046 °	9.03 km
Median Q1+2+3	102	83.29 °	59.77 °	$3.96 \cdot 10^3 \text{ km}^3$	0.042 °	0.0035 °	8.25 km

Table 4.5: Average quality characteristics of for well-located events. Dataset inherent quality as in maximum epicentral distance (Δ) and in azimuthal gap (Γ) as well as quality of the location in scattervolume, difference in maximum-likelihood hypocenter and expectation hypocenter (DIFFLON/DIFFLAT) and length of semi-major axis of error-ellipsoid adjusted to 2D.

4.3 Stability and Uncertainties of the Solution

4.3.1 Stability of well-located Events

The stability of the localization can only be judged through careful evaluation of the results in testing, namely the velocity model, the grid-search algorithm and weighting of station clusters.

Teleseismic earthquake localization is critically dependent on the velocity structure of the modelled earth. For the 85°N region and the 1999 swarm I implemented a local velocity model of oceanic crust (Fig. 3.16) to be used at a list of near-stations (Fig. 3.17) where the error introduced by an assumed continental crust as displayed by the AK135 velocity model would have a large influence on calculated travel times. The usage of this local velocity model improves the localization as displayed by the drop in scattervolumes (Fig. 3.19) for the better constrained events. The fact that the epicenters do not shift significantly for this dataset signifies a stable location.

In searching for the maximum of the PDF, the oct-tree algorithm defines the search for the true maximum, which can only be located within the size of the smallest searched grid-cell. This is visually observable at linearities in epicenter distribution of less-constrained events along geographic longitudes (Fig. 3.8). For the better constrained events this effect is not visually observable and the shifting of epicenters as originating from a variation of starting cells does not exceed 3 km which is less than 4.07 km as the smallest semi-major axis for the well-located dataset. Therefore the oct-tree algorithm seems to be stable in teleseismic localization of well-constrained events.

The influence of weighting for station clusters is again highly dependent on the dataset. For the 85°N region and the 1999 swarm the biggest effect is displayed for less constrained events (Fig. 3.12) where the weighting algorithm weights the global distribution of recording stations which are scarce, giving a slightly better scattervolume. For better constrained events (Fig. 3.13) with actual station clusters included the difference between the weighted and the unweighted set does not exceed 3 km which is less than 4.07 km as the smallest semi-major axis for the well-located dataset, therefore the localization itself is stable with regard to epicentral shift. The lack of difference in scattervolumes (Fig. 3.14) indicates reasonable homogeneous coverage in epicentral- and azimuthal direction.

4.3.2 Uncertainties

The predefined error for travel-time inherent in the velocity model, as well as the error from recording are assumed to be Gaussian and normal distributed. In teleseismic earthquake localization this assumption is most certainly not realistic. The error this introduces into the hypocenter location cannot be quantified.

For quantification and judging of results, uncertainties of individual hypocenters are calculated as the probabilistic quality marker scattervolume and as the Gaussian error parameters RMS and the 68% error-ellipsoid.

Scattervolume gives the relative volume of the scattercloud with respect to the global searched grid, with samples drawn in proportion to the value of the normalized PDF. As shown in Tbl. 4.3 the volume of the scattercloud is a reliable quality marker in probabilistic earthquake localization.

Gaussian error parameters are based on the assumption of a normal distribution which is not realistic in teleseismic earthquake localization. The value of the RMS of the travelttime-residuals designates in this context the deviance of the root-mean-square of calculated travelttime-residuals from a supposed normal distribution and does not give an indication of the deviance to the true hypocenter location.

The 68% error-ellipsoid is calculated from the covariance matrix of the scattersamples. The covariance matrix itself is given by the following equation (Eq. 4.1) with the expectation hypocenter as $E(\mu_i, \mu_j)$ and is based on the chi-squared distribution.

$$Cov_{ij}(X_i, Y_j) = E[(X_i - \mu_i) - (X_j - \mu_j)] \quad (4.1)$$

The expectation hypocenter designates the weighted average between all sets of scatter-samples and gives the center of the error-ellipsoid. This expectation hypocenter does not in fact have to coincide with the maximum-likelihood hypocenter which is only dependent on the value of the PDF within the smallest searched grid-cell. If both hypocenters occupy the same point in space (expressed in the calculated parameters DIFFLON/DIFFLAT) then the scattercloud is likely to have ellipsoidal form and can be described by the 68% error-ellipsoid (Fig. 4.2). If the scattercloud does not have ellipsoidal form this likely is caused by problems in calculation of the PDF i.e. through second maxima (Fig. 2.3(a)) or oscillating hypocenters (Fig. 2.3(b)), hence the 68% error-ellipsoid cannot be fitted to the scattercloud and gives erroneous parameters. Therefore the 68% error-ellipsoid can only be evaluated combined with DIFFLON/DIFFLAT.

For the characteristics of the well-located dataset with regard to scattervolume, RMS, DIFFLON/DIFFLAT and the semi-major axis of the error-ellipsoid adjusted for 2D I refer to Tbl. 4.5.

4.4 Hypocentral Depth Evaluation

The distribution of hypocentral depth to number of events within the well-located dataset (Fig. 4.5) shows the majority of events between 0 and 5 km with 14 events. Only 5 events locate between 5 and 15 km. Between 15 and 20 km, 13 events took place. The 31 deepest events have a hypocentral depth ≥ 20 km.

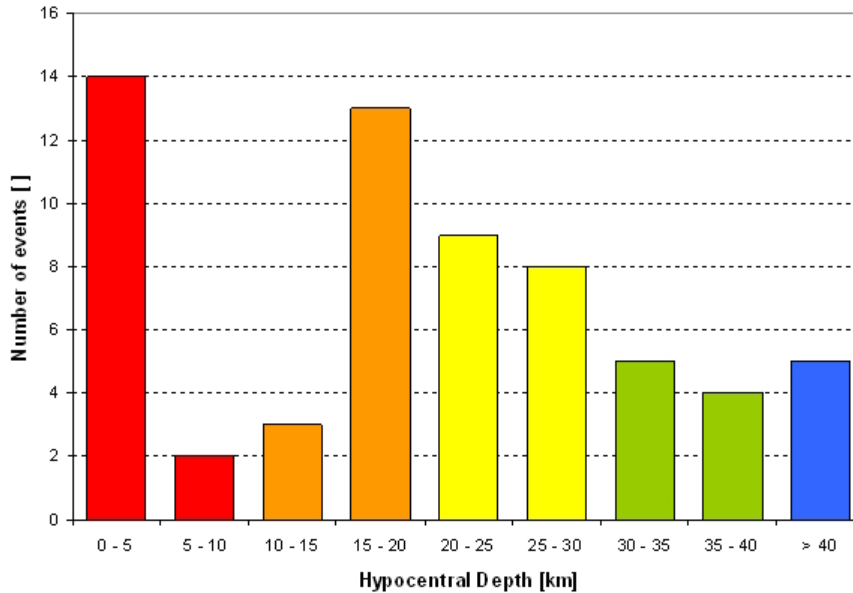


Figure 4.5: Hypocentral depth distribution of the 63 well-located events.

Regarding uncertainty in depth a median of 19.9 km for the error-ellipsoid semi-axis of the complete well-located dataset of 63 events adjusted for 2D seems to disqualify any attempted interpretation of hypocentral depth. A comparison of the NonLinLoc Qualities (1-3) in Tbl. 4.6 shows, that as the dataset overall gets more uncertain from Quality (1) to (3), the median of the corresponding error-ellipsoid semi-axis gets longer.

Quality	Number	Median
NonLinLoc (1)	43	16.7 km
NonLinLoc (2)	10	22.8 km
NonLinLoc (3)	10	35.2 km

Table 4.6: Median lengths of error-ellipsoid semi-axis in depth, adjusted for 2D of NonLinLoc Quality 1-3

In teleseismic localization depth presumably is always poorly constrained in the absence of near stations and when calculated using only P- and S-phases. In probabilistic earthquake localization, a further problem lies in calculating the depth within the spherical grid which is used for the calculation of traveltimes. Here, discontinuities can cause the search for the maximum of the PDF in depth to oscillate, giving depth coordinates which correspond to a velocity discontinuity (Fig. 2.3(b)). Within my well-located dataset, I found an indication of this behaviour preferentially in events with a high number of phases and here almost exclusively for events with the highest number of phases, namely the 11 $m_b \geq 5$ events. Of these, 8 events showed hypocenters at 0.1 km depth which is unlikely even if supposing shallow hypocenters. The remaining 3 events within the dataset of $m_b \geq 5$ events all display 25.0 km hypocentral depth.

A visual plot of hypocentral depths for the well-located dataset (Fig. 4.6) shows a clustering of events with shallow hypocenters elongated within the central rift valley. Farther southwest, at the rift valley walls and beyond, the hypocentral depths get more diverse.

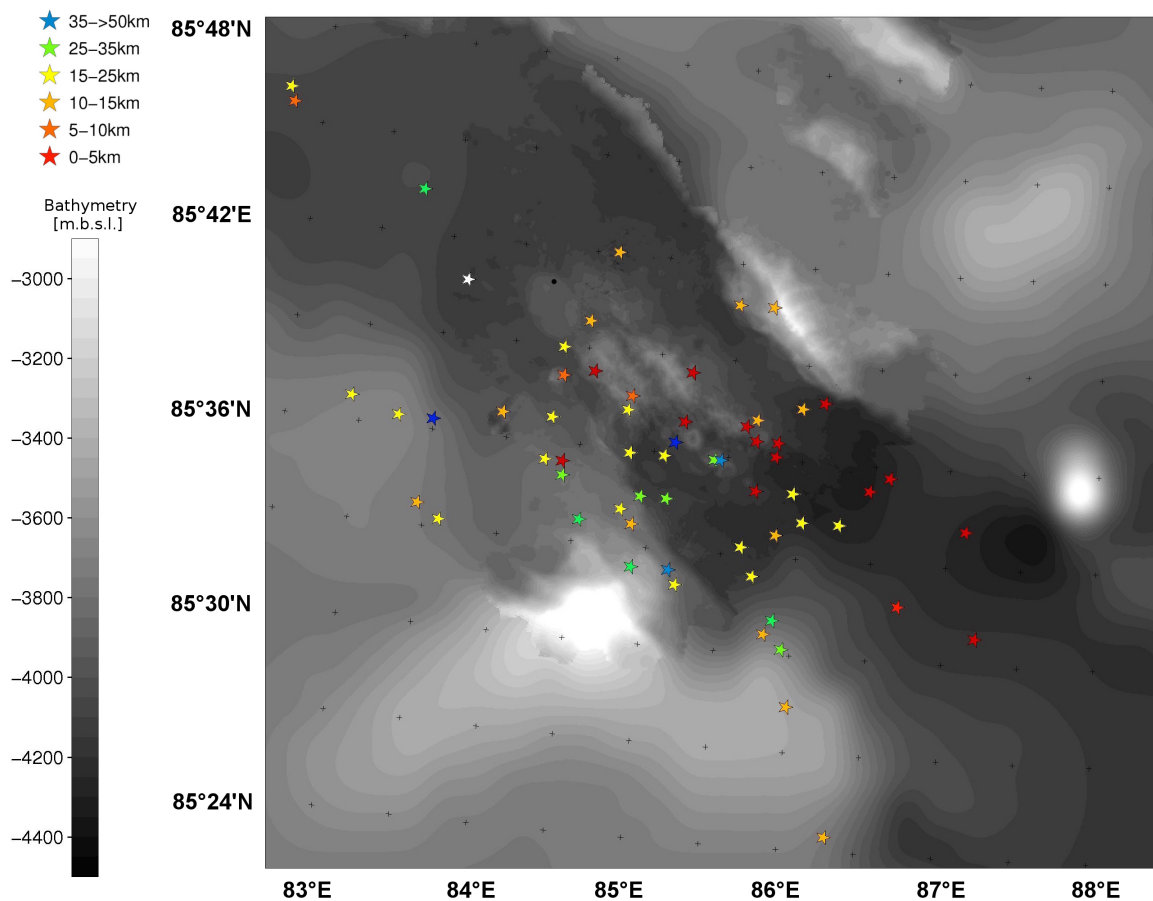


Figure 4.6: Epicenters of the 63 well-located events, colour-coded for their source depth.

The interpretation of hypocentral depths is critically dependent on the local velocity structure in the source region. The local velocity model for oceanic crust by *Riedel and Schlindwein* (2009) describes gradually increasing velocity in the absence of clear layering down to a depth of 16 km. At oceanic crustal depths a seismic velocity of about 6 km s^{-1} as assumed by the local velocity model corresponds to a temperature of 800°C (*Khitarov et al.*, 1983) for laboratory measurements of peridotite. The brittle-ductile boundary occurs at about 1000°C or a depth of 23 km if 30°C temperature increase per kilometer is assumed as for an average continental crustal environment. At $85^\circ\text{E} / 85^\circ\text{N}$ the AGAVE and AMORE expeditions found multiple evidence for recent volcanic activity (*Sohn et al.*, 2008) which points to a recently existing magma source and suggests brittle-ductile transition in a warm thermal regime with shallower hypocentral depths.

An independent method to get a crude estimate of hypocentral depths are traveltimes differences of pP-P-waves and sP-P-waves respectively. sP- and pP-waves leave the earthquake focus vertically upwards and are reflected at the sea surface or at the seafloor before travelling onward to the seismic recording station. The difference in arrival times to the direct P-arrival signifies depth under the assumption of vertical ray take-off from the source. For the upper crustal structure at Gakkel Ridge, a P-wave velocity of 6 km s^{-1} has been assumed for the oceanic crust; S-wave velocity is 3.4 km s^{-1} assuming a v_p/v_s ratio of 1.73. A problem of this method is the reliability of picking and the correct identification of phases which I have provisionally assumed to be accurate due to the finished review by the ISC (*ISC*, 2008).

In the following I will calculate the mean depth for two exemplary $m_b \geq 5$ events (events 19990201.045512 and 19990313.012903) as there the largest number of pP- and sP-phases were identified (Tbl. 4.7).

NonLinLoc Event	Stations	pP-arrivals	Median pP-P	sP-arrivals	Median sP-P
19990201.045512	249	6	2 sec	21	7 sec
19990313.012903	373	3	3 sec	28	8 sec

Table 4.7: Characteristics of two exemplary events for mean depth estimation by the number of pertinent phases and the mean difference in arrival times of P- and pP-/sP-phases.

I have calculated a rough source depth from the pP-P and the sP-P traveltimes differences assuming two different reflection points for each phase (Tbl. 4.8). The first ray is assumed to be reflected at the solid/water boundary, the second at the water/air boundary. I assumed a water layer of 3.5 km with a velocity of 1.5 km s^{-1} .

Event	Source Depth	Seafloor reflection		Sea surface reflection
		pP-P	sP-P	sP-P
19990201.045512	0.1 km	12 km	24 km	8 km
19990313.012903	0.1 km	20 km	27 km	11 km

Table 4.8: Mean depth estimation by difference in arrival times of P- and pP-/sP-phases of two exemplary events and comparison with NonLinLoc hypocentral depth.

For pP-waves reflected at the sea surface the calculation gives negative results, indicating that traversing the water column takes longer than the observed pP-P traveltime-difference. Hence these phases must have bounced off the solid/water boundary. The sP-waves seem to be reflected at the water/air boundary as the source depth estimation for a reflection at the seafloor comes out rather large (24 and 27 km depth below the seafloor respectively) for a supposedly thin oceanic crust. If I calculated the source depth for this phase (called in the following pP_s) I obtain values which are close to the ones for pP-waves with 14 km and 20 km respectively (Tbl. 4.9). This would point to a misidentification of phases by automatic picking.

Event	Source Depth	Sea surface reflection
		pP_s -P
19990201.045512	0.1 km	14 km
19990313.012903	0.1 km	20 km

Table 4.9: Mean depth estimation of two exemplary events by difference in arrival times of pP_s -P source depth which was calculated under the assumption of a misidentification of a pP-phase as the sP-phase.

Both events nevertheless seem to have source depths which are some distance down into the crust, at 12 and 20 km, if I assume that the consistency of pP- and pP_s takes precedence over correct automatic identification of phases. This contradicts the calculation of NonLinLoc which gave 0.1 km hypocentral depth for these two events. *Bergman and Solomon* (1990) mark that the largest earthquakes on mid-ocean ridges probably are induced by normal faulting at deep faults and their epicenters locate near the center of the inner floor of the median valley as because these faults are dipping at about 45° . A substantial depth of several kilometers below the seafloor would therefore be more realistic than directly at the seafloor.

However, this crude estimate uses first-order assumptions which are not strictly valid (vertical ray take off, single-velocity layer model, straight ray path along a flat surface) and prevent an accurate estimate of true source depths. Certainly the observed traveltime-differences pP-P tells us at least, that probabilistic hypocentral depth calculation for teleseismic events by NonLinLoc with only P- and S-phases and no additional information incorporated into the calculation is not stable enough to make an interpretation possible.

4.5 Comparison of NonLinLoc probabilistic localization with Hyposat least-squares based algorithm

Riedel and Schlindwein (2009) relocated the 1999 swarm with the localization routine Hyposat (*Schweitzer*, 2001). The program is based on conventional least-squares minimization of traveltime residuals and it incorporates additional phases and phase differences to constrain the hypocenter better than the routine procedure *iscloc* (*Luckett and Storchak*, 2006) used by the ISC (*Luckett and Storchak*, 2006). It seems indicated to compare the probabilistic localization with this least-squares based algorithm.

NonLinLoc localized 250 events, but only 237 events could be localized by Hyposat. The missing 13 events are only found among the NonLinLoc quality (5) and display small magnitudes $m_b \leq 4.1$. All of these events occurred before April 15th. In the following I will only compare the 63 epicenters of NonLinLoc Quality 1,2 and 3 with the corresponding Hyposat epicenters. Hypocentral depth evaluation by NonLinLoc for this dataset is not reliable so I will exclude depth from comparison.

For a first visual overview I plotted only NonLinLoc Quality 1 events and the corresponding Hyposat epicenters (Fig. 4.7). Whereas NonLinLoc clusters epicenters within the central rift valley with diffuse events at and beyond the southern rift valley walls and virtually no events reliably located at the northern rift valley walls, Hyposat gives a more diffuse clustering of epicenters at the northern rift valley wall and within the central rift valley. The difference in kilometers for the two sets of epicenters does not exceed 25 km which is, however, larger than the calculated epicenter uncertainties of each method.

Regarding uncertainty, Hyposat gives vastly smaller error-ellipses than NonLinLoc for teleseismic localization (Tbl. 4.10). For teleseismic localization, an 68% error-ellipse with a length of semi-major axis of 2.02 km (Hyposat, median of Quality 1) is unrealistically small.

		Q 1	Q 2	Q 3
Hyposat	Minimum	1.10 km	2.50 km	2.77 km
	Maximum	4.79 km	4.23 km	7.71 km
	Median	2.02 km	4.32 km	3.88 km
NonLinLoc	Minimum	4.07 km	10.43 km	11.89 km
	Maximum	9.94 km	13.10 km	22.64 km
	Median	7.34 km	12.09 km	13.14 km

Table 4.10: Comparison of 68% error-ellipse parameters for NonLinLoc Quality 1,2 and 3 events with the corresponding Hyposat localized events.

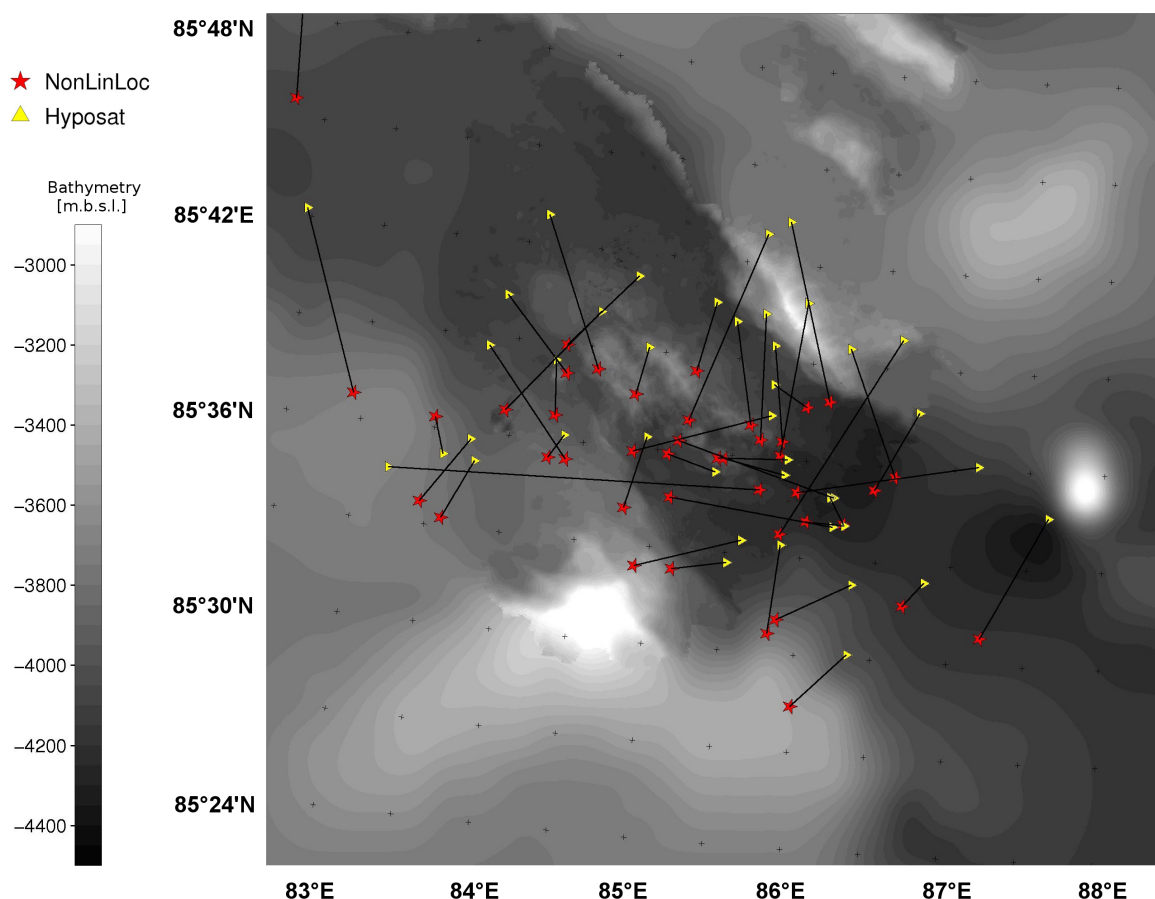


Figure 4.7: 43 events of NonLinLoc Quality 1 and corresponding Hyposat epicenters.

When comparing the systematic variation of the length of error-ellipse semi-major axes of Hyposat and NonLinLoc with regard to the dataset which is expressed by the NonLinLoc Quality 1,2 and 3 it seems as if a significantly lower quality of the dataset (NonLinLoc Quality 3 in comparison to Quality 1) increases the length of error-ellipse semi-major axes when calculated by both programmes. NonLinLoc Quality 2 is a variation of Quality 1 with a slightly greater scattervolume (Tbl. 4.5) and it comprises events with longer error-ellipsoid semi-major axes which is surprisingly not seen in the lengths of semi-major axes as calculated by Hyposat.

The calculation of small error-ellipses by Hyposat may be based on the fact that Hyposat removes phases with big traveltime residuals to better fit the remaining phases to each other. In comparison, NonLinLoc, when faced with the same problem, downweights the pertinent phases but does not remove them entirely.

Another problem with Hyposat lies with the influence of the start model for the iteration. When varying the start epicenter other phases may have big traveltime residuals and consequently get removed, making the localization unstable in that regard. Additionally,

Hyposat as a least-squares algorithm probably includes skewing of epicenters which is caused by the attempted fitting of outliers to the data. The lack of reliability of the RMS as a quality indicator (Tbl. 4.3) seriously influences the localization by Hyposat as its algorithm calculates hypocenters by least-squares minimization of traveltime residuals.

Regarding location of epicenters as calculated by Hyposat and NonLinLoc, both solutions fail to match even with error-ellipses uncertainty taken into account (Fig. 4.8). Hyposat locates the majority of events further to the north and northeast than NonLinLoc, showing more activity at the northern rift valley wall compared to the southern rift valley wall activation as indicated by NonLinLoc. In conclusion as seen in this comparison, the location algorithm significantly influences the resulting locations and should be chosen deliberately with regard to the quality of the initial dataset.

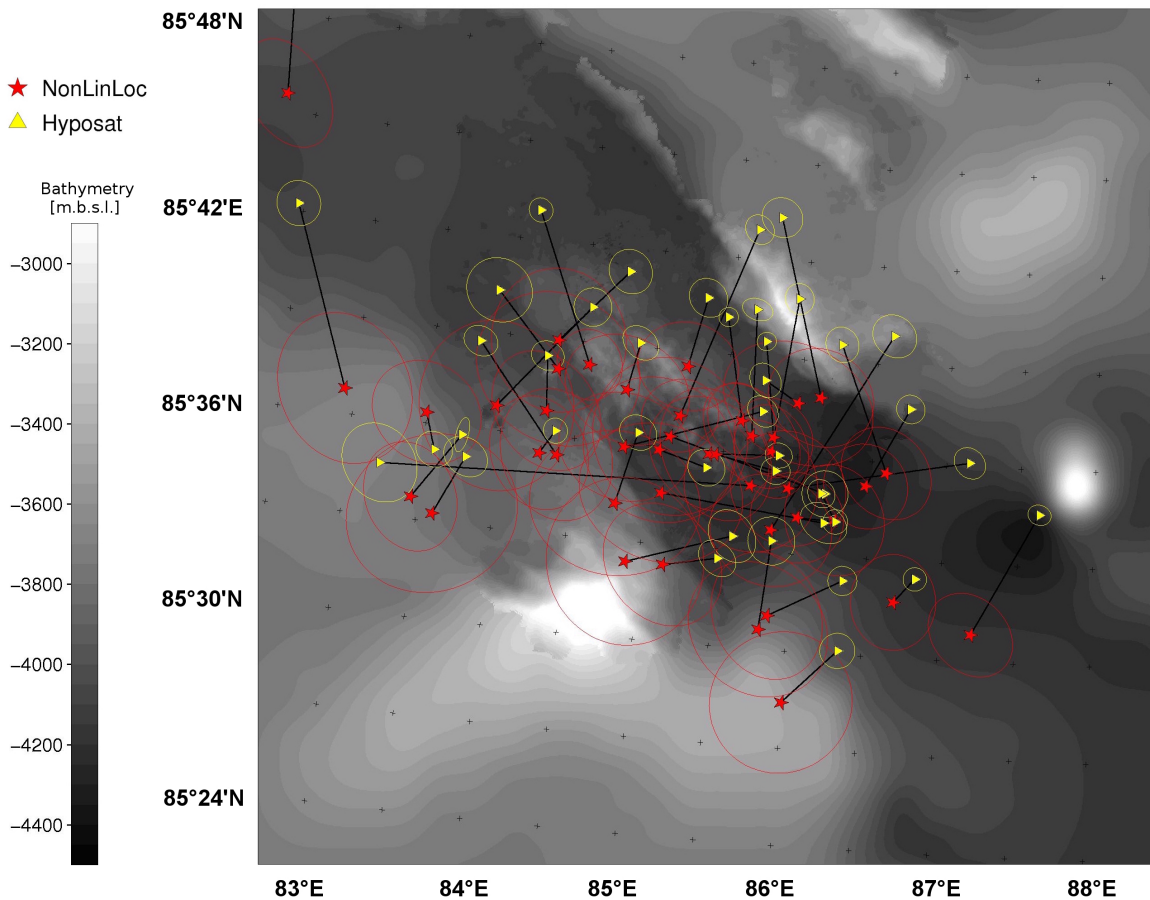


Figure 4.8: 43 events of NonLinLoc Quality 1 and corresponding Hyposat epicenters with 68% error-ellipses.

4.6 Evaluation of Station Residuals

Riedel and Schlindwein (2009) indicated systematic station residuals at the stations closest to the earthquake swarm (Fig. 1.35), based on their location with the least-squares algorithm Hyposat. To investigate if this trend is still observable after relocation with NonLinLoc probabilistic location algorithm, I performed a traveltime residual analysis for stations near the epicenter at a maximum of 30° epicentral distance. I used traveltimes from all earthquakes of the 1999 Gakkel Ridge swarm and calculated the residual analysis separately for P-waves.

For analysis, I calculated mean, variance and standard deviation of P-wave traveltime residuals at these near-stations and plotted a histogram for each station. Additionally I separated between events with < 50 phases and ≥ 50 phases used in localization to see if mean station residuals differ significantly between events which are reasonable well constrained and the less constrained dataset. In the following I will show selected station histograms (Fig. 4.9).

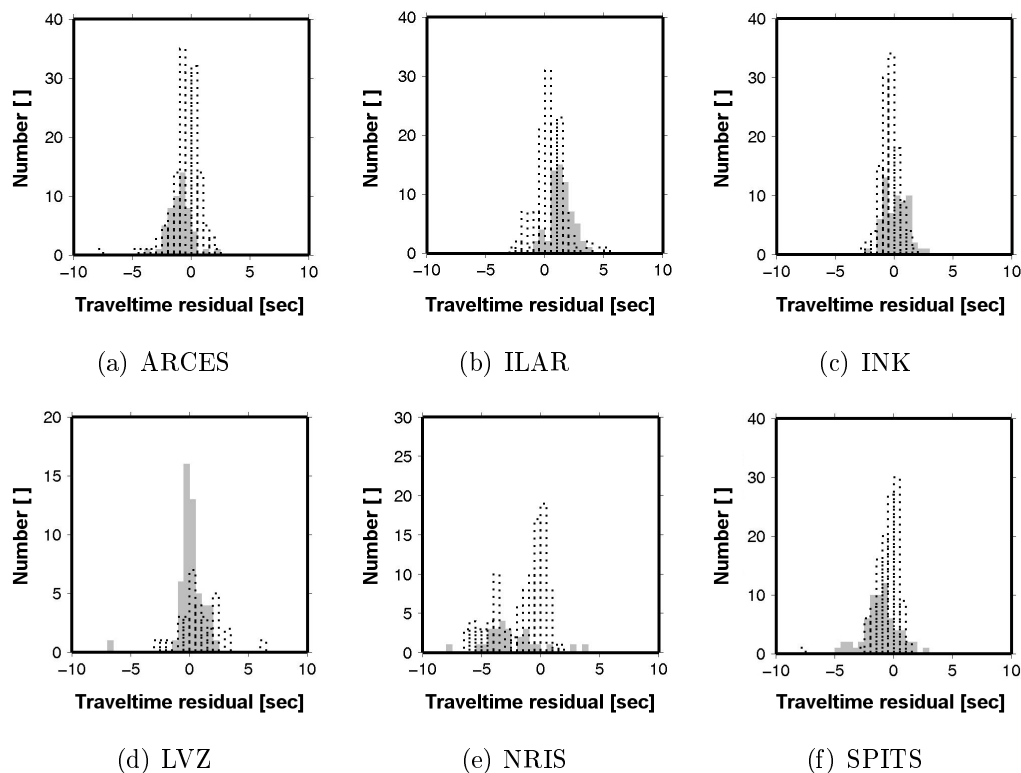


Figure 4.9: Station residuals for selected near-stations. Grey bars are traveltime residuals by well-constrained events with ≥ 50 phases used in localization, dotted lines designate the less-constrained dataset.

Peaks scatter for the less constrained dataset around 0 sec, however for the better constrained events I observe a shift to greater positive or negative anomalies. The corresponding mean, variance and standard deviation of P-wave traveltime residual for both datasets are given in Tbl. 4.11.

Station	< 50 phases			≥ 50 phases		
	Mean	Variance	Stdev	Mean	Variance	Stdev
ARCES	-0.48	1.57	1.25	-0.97	1.23	1.11
ILAR	1.37	1.47	1.21	0.49	1.47	1.21
INK	-0.38	0.61	0.78	0.15	0.94	0.97
LVZ	0.81	3.12	1.77	0.07	1.51	1.23
NRIS	-1.92	9.84	3.14	-2.46	8.17	2.86
SPITS	-0.53	1.15	1.07	-1.07	2.39	1.55

Table 4.11: Statistical parameters of station residuals for selected near-stations.

A plot only for the better constrained events with stations color-coded for their mean delay (Fig. 4.10) visualizes interestingly, that stations in Russia and in the western part of the USA exclusively display positive traveltime-residuals. This supports the findings of *Riedel and Schlindwein* (2009). Stations in Europe and Greenland/Spitsbergen display diverse residuals.

For well-constrained events with a large number of observations, an abundance of large distance stations exists for which the homogeneous 1D velocity model achieves a good fit. However, for closer stations rays travel through shallower layers of the upper mantle with heterogeneities not incorporated in a 1D velocity model. Residuals at these sparse near-stations are tolerated by the algorithm to better fit the abundance of large distance stations, but they are not removed entirely from calculation. This results in predominantly travel time delays along Gakkel ridge toward the east, indicating lower velocities in this direction than the reference velocity model. In the opposite direction towards Svalbard and northern Norway, a tendency to faster arriving phases is observed, although results may differ at nearby stations, indicating potential influence of the local sub-receiver structure.

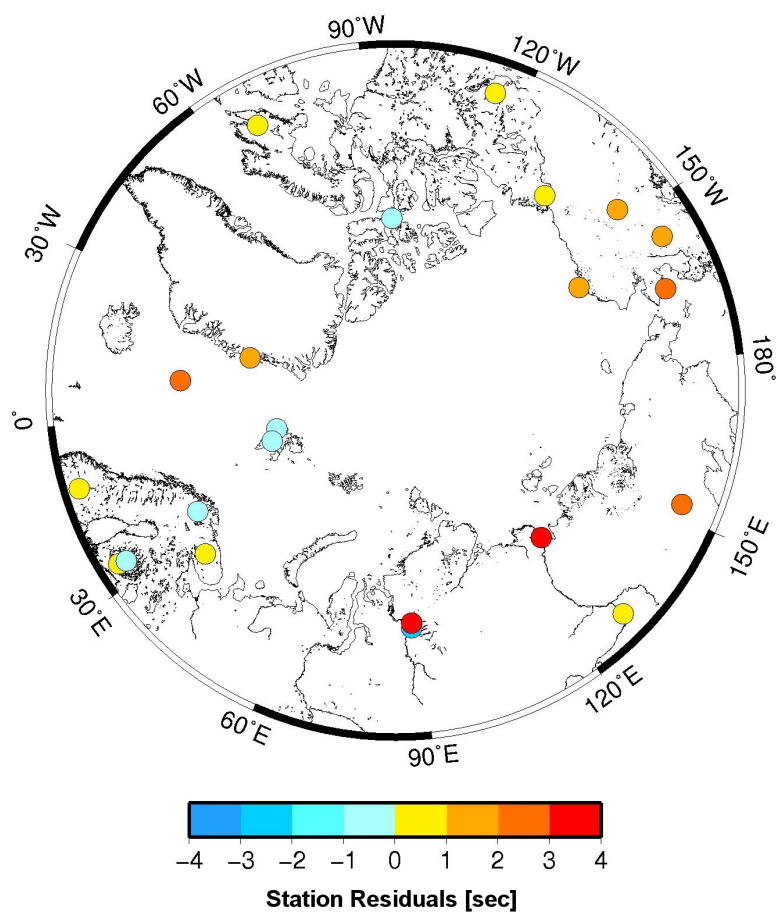


Figure 4.10: Geographical location of stations, plotted color-coded with their mean station residual.

Chapter 5

INTERPRETATION

Active spreading at slow- and ultraslow spreading mid-ocean ridges is characterized by distinct, infrequent magmatic events. The inner valley floor is heavily fissured, the faulting getting deeper as the median valley walls are approached. The deepest faults probably sit at the valley walls and extend several kilometers down the median valley. In 1999 the longest and strongest earthquake swarm ever to have been recorded occurred at the volcanic center 85°E/85°N on eastern Gakkel Ridge.

Earthquake swarms at mid-ocean ridges can be classified into two categories: The first class accompanies the creation of new oceanic crust by intrusion of dykes from a magma chamber, second class earthquakes are created by extensional tectonics as the newly created crust adjusts to the environment. Volcanic swarms itself are not unheard of at mid-ocean ridges but they are rare e.g. *Dziak et al.* (1995).

The nature of the 85°E swarm has been cause of some debate. *Müller and Jokat* (2000) postulated crustal breakage, followed by a volcanic event with caldera collapse. *Tolstoy et al.* (2001) suggested fault activation by an initial magmatic pulse from a deep magma chamber, and later on activation of a large area through slow lateral migration of several following pulses. *Sohn et al.* (2008) suspected that the volumetric changes in the source mechanisms of the later events are indicative of multiple episodes of explosive volatile discharge from a deep magma chamber. *Riedel and Schlindwein* (2009) speculate that the location of a volcanic conduit was marked by three highly correlating events. In this study, I review these interpretations in the light of the best constrained relocated epicenters.

5.1 Temporal Analysis

Seismicity itself is described first and foremost by the number of events and the duration of swarms. Up to the beginning of 1999, the number of teleseismic events within an earthquake swarm did not exceed 55 (*Fox and Dziak, 1998*) and the longest duration was 25 days (*Crane et al., 1997*). As seen in the figure below for swarms located on the MAR up to 1989, the 1999 earthquake swarm would not even be on the graph.

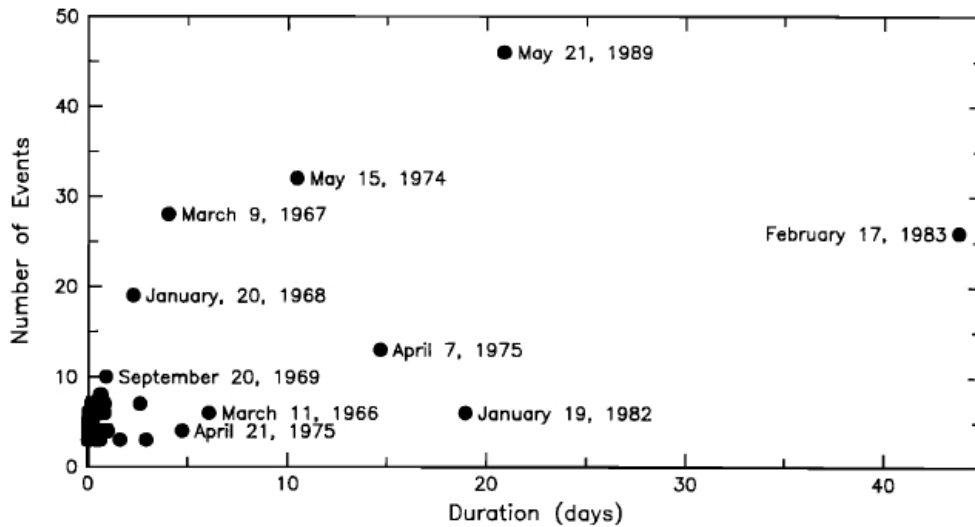


Figure 5.1: Earthquake swarms on the MAR between 10°N and 60°N in the years 1964-1989 with number of events and duration. Swarms with 10 or more events or lasting longer than 3 days are labelled (*Bergman and Solomon, 1990*).

Tolstoy et al. (2001) analysed the 252 events of the 1999 earthquake swarm with regard to event rate and found a marked drop onward from the 15th of April from more than 2 events per day to a quarter of that. My analysis of the cumulative number of events gave the same characteristic (Fig. 5.2).

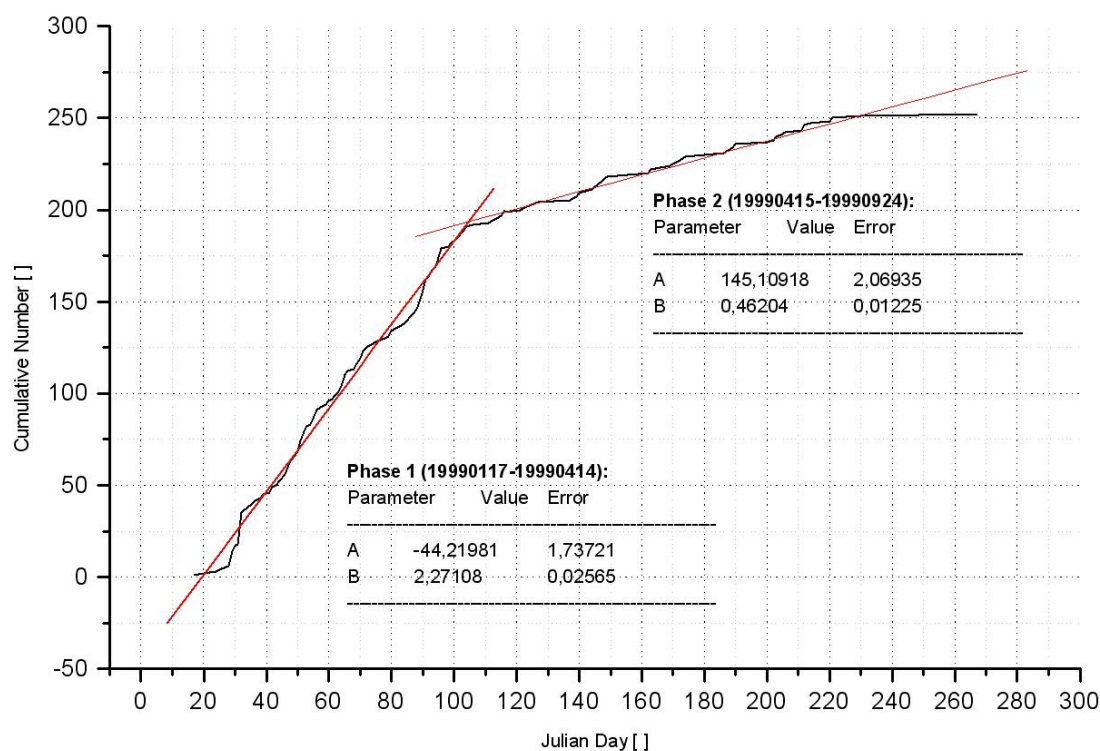


Figure 5.2: Seismicity based on cumulative number of events. Regression has been described by a linear equation $Y = A + B \cdot X$

For a better understanding of the released energy I investigate additionally the temporal development of the seismic moment (M_0) as it is closely related to the low frequency displacement spectrum and therefore to tectonic processes like static displacement and rupture. M_0 is calculated from the surface wave magnitude (M_s) by an exponential factor (Eq. 5.1) for events with $M_s \leq 6.4$ chenzhen89 p85 under the assumption of a Huskell source modell.

$$\log M_0 = M_s + 12.2 \quad (5.1)$$

The *ISC* (2008) comprehensive bulletin includes M_s -values if available, but in the case of the 1999 earthquake swarm at Gakkell Ridge only about one quarter of the reported events have them included. To get a sensible M_s -value for the incomplete events I plotted the linear fit regression for all events which had m_b as well as M_s magnitudes reported and calculated then the missing M_s values from the regression line (Fig. 5.3). The error for M_s lies between 0.2 for $m_b = 4.3$ and 0.3 for $m_b = 5.2$ which corresponds up to $3 \cdot 10^{12}$ Nm.

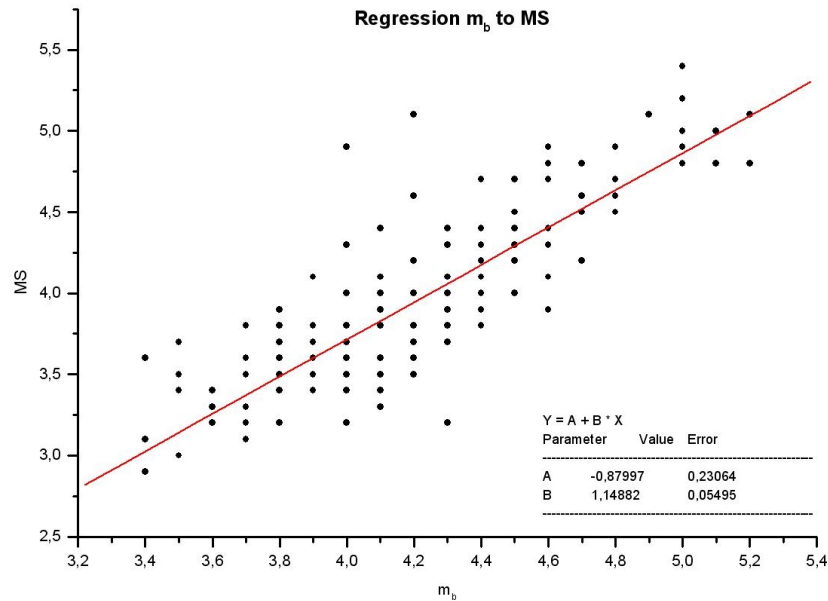


Figure 5.3: Regression for conversion m_b to M_s from reported values. Regression has been described by a linear equation $Y = A + B \cdot X$

Within the plot for cumulative seismic moment, three temporal phases are observable (Fig. 5.4). The first phase from 17th January up to and including the 1st February released by far the most seismic energy and lies within the high seismicity time window as observable in the cumulative seismicity plot (Fig. 5.2). The second phase from 2nd February to 6th April also has high seismicity with 2 events per day. Its end is not well defined and the change to events of the third category is subtle over at least one week. Within this changeover lie the three highly correlating events Riedel and Schlindwein (2009) speculate to be indicative of an opening volcanic conduit. The third and last phase which I defined from the 7th April to the end of the swarm at 24th September, corresponds roughly to the second temporal seismicity phase with one event per two days and only sparse releasing of seismic moment.

Within the 16 days of the the first phase in time, roughly the same amount of energy has been seismically released as within the 171 days of the third phase (Tbl. 5.1). The 64 days of phase 2 released about two times the seismic energy as the preceding and the following phase.

	Number of events	Energy release
Phase 1: 19990117-19990201	16	$1.4 \cdot 10^{18}$ Nm
Phase 2: 19990202-19990406	64	$3.1 \cdot 10^{18}$ Nm
Phase 3: 19990407-19990924	171	$1.4 \cdot 10^{18}$ Nm

Table 5.1: Seismic energy release during three phases in time for the 1999 earthquake swarm.

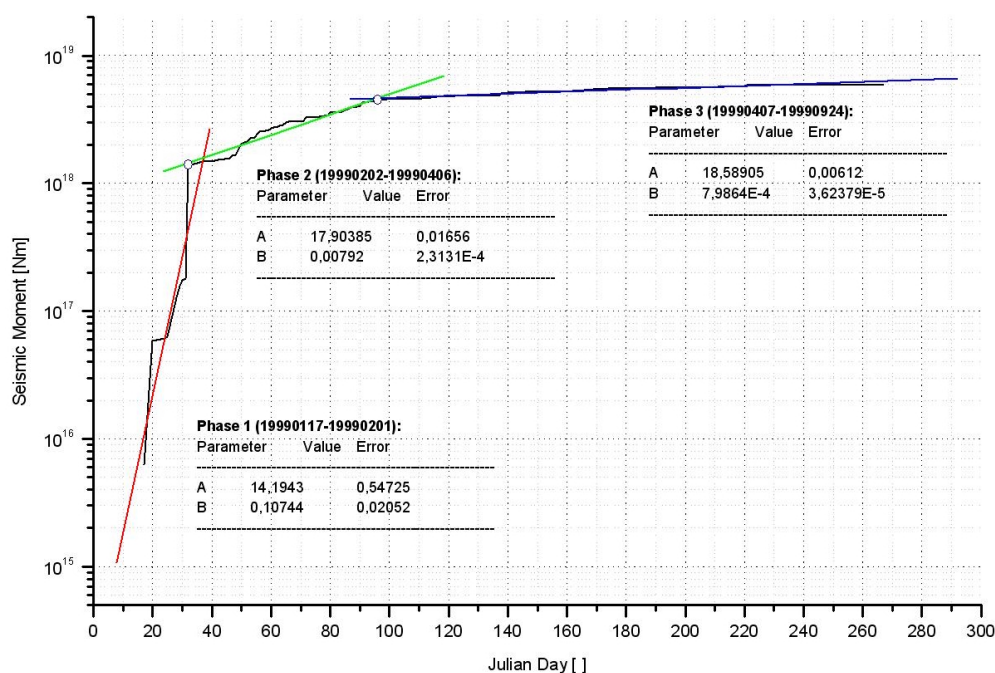


Figure 5.4: Cumulative seismic moment per julian day. Regression has been described by a linear equation $Y = A + B \cdot X$

I also recalculated the b-values with a magnitude of completeness of $m_{bC} = 4.2$ as indicative for the number of events to their magnitudes m_b (Tbl. 5.2). I cannot confirm the extremely high b-values as published by *Müller and Jokat* (2000) of 1.4 before 4th March and 1.9 after March, 4th as they were calculated by another dataset, namely the 258 NEIC catalogue events. The recalculated b-values of the ISC reviewed bulletin have a completely new characteristic. With the recalculated b-values, at the beginning of phase 2 a substantial change to fewer high magnitude events in comparison to the number of low magnitude events is observable. The later high b-values could be explained by a weaker crust which cannot sustain high stress levels. This change in b-values would be consistent with a previous emplacement of new material into a dyke system within temporal phase 1 and thereafter the adjustment of the old, weak crust to the new stress field.

	b-value
Phase 1: 19990117-19990201	0.96
Phase 2: 19990202-19990406	1.30
Phase 3: 19990407-19990924	1.36
Overall	1.36

Table 5.2: b-values of the magnitude-frequency relation, calculated for the three phases in time of the 1999 earthquake swarm.

5.2 Spatiotemporal Analysis

Regarding spatiotemporal development of the swarm I only analysed the 63 well-located events for their epicenters. I calculated the rectangular activated area for each phase in time (Tbl. 5.3) with a center of mass given by the mean of earthquake epicenters within each phase. Because of the curtailed dataset, this analysis may not give the actual spatial extension of each phase (when all epicenters would be included). Assuming that all teleseismically recorded events are associated with the same geological processes, the spatial trend of the well-located earthquake epicenter should be indicative of the actual spatial migration (Fig. 5.5).

	Activated Area
Phase 1: 19990117-19990201	2300 km ²
Phase 2: 19990202-19990406	3451 km ²
Phase 3: 19990407-19990924	3875 km ²

Table 5.3: Activated area during each phase in time for the well-located dataset.

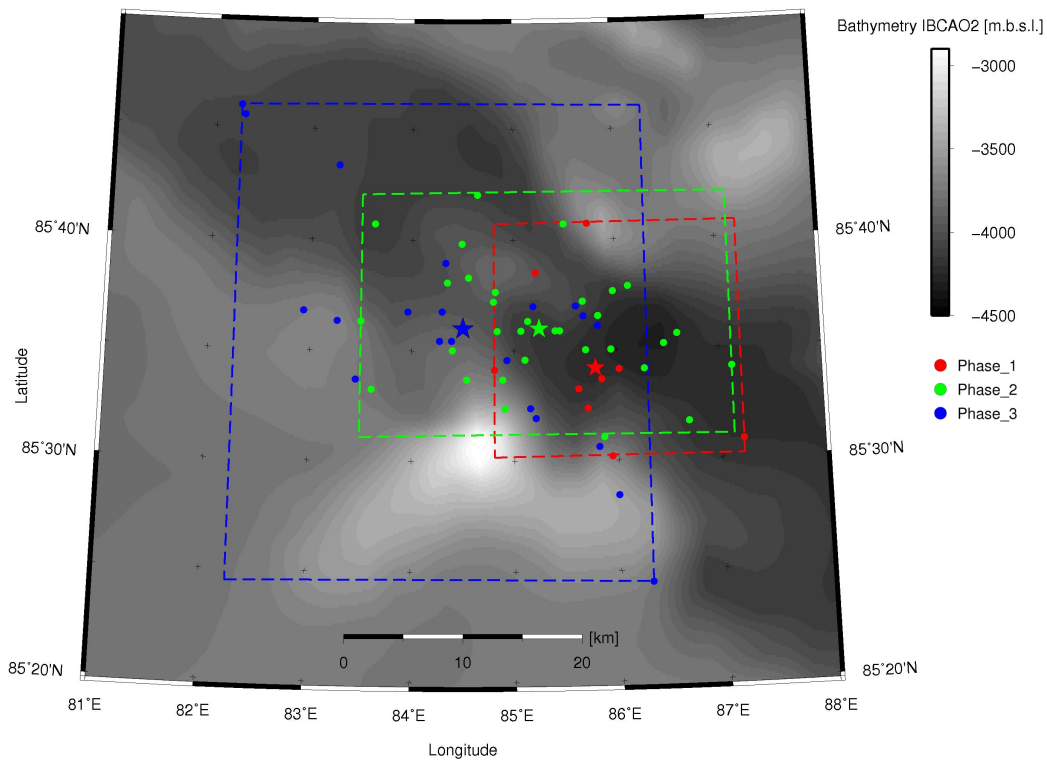


Figure 5.5: Overview on spatiotemporal development of the 1999 earthquake swarm. Colors refer to phases in time. The geographic center of mass of earthquake epicenters for each phase was marked by a star. Each activated area is marked by a dashed line.

From phase 1 to phase 3 the activated area gets progressively greater. Epicenters of phase 1 and 2 are confined more or less within the central rift valley. Earthquakes of phase 1 occur almost exclusively within the deepest part of the rift valley. Phase 2 earthquakes are mostly scattered about the site of the volcanic ridge in the rift valley, with some events at the southern rift valley walls. Finally phase 3 activates the widest area and is situated more to the northwest with mostly scattered epicenters at the southern rift flanks.

Phase 1: (Figs. 5.6(a), 5.6(b))

The well-located dataset for phase 1 comprises only 9 events within 5 days. The very first event at day 28 was located within the central rift valley, at the foot of the southern rift valley wall with the following events taking place on day 32 and mostly activating faults in the vicinity. The highest seismic moment was released by two events in red within the central rift valley, one of them to the north in the vicinity of the volcanic cones and the other to the south. Three geographically close events within the central rift valley released about the same amount of moderate seismic energy (green), and events located at the rift flanks released the smallest amount (light blue). Excluding the one event on day 28, all other well-located events within phase 1 happened on February, 1st.

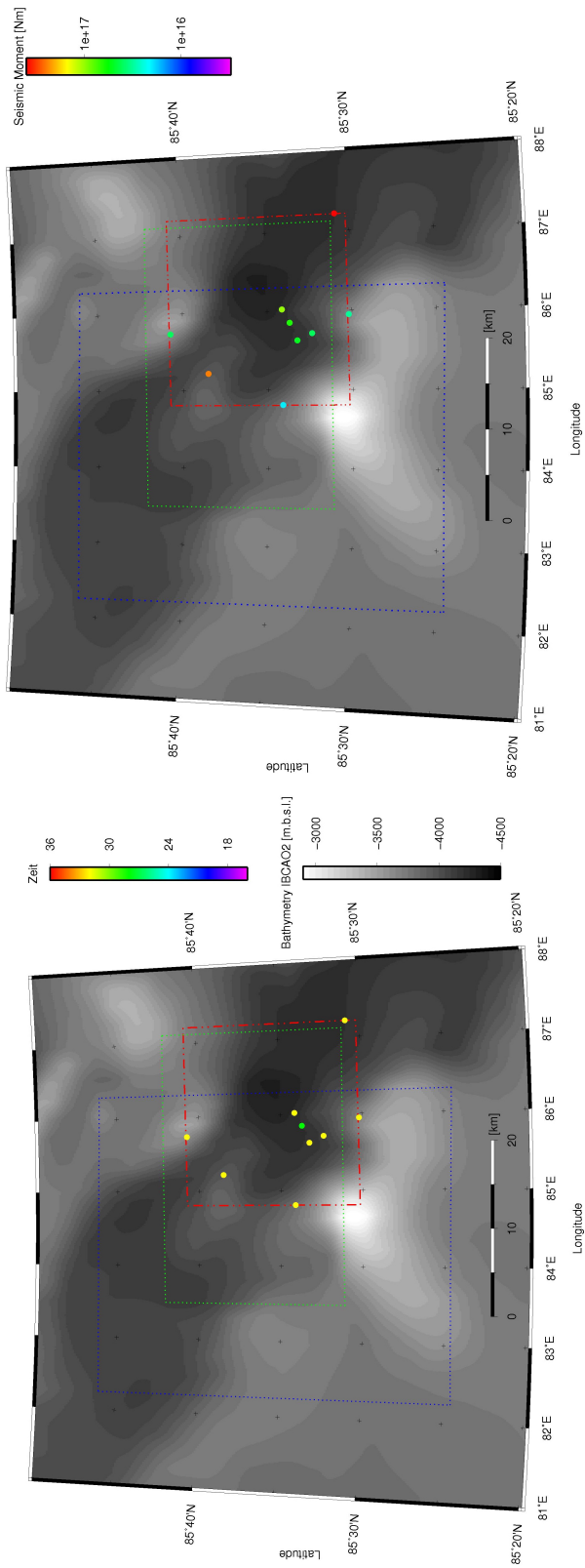
Phase 2: (Figs. 5.7(a), 5.7(b))

Events of phase 2 are more heterogeneously distributed with a difficult spatial development. At the beginning the events concentrate at the southern rift valley walls (blue and light blue colors), followed by a cluster of green events within the central rift valley in the north about day 70. Finally at the end of phase two, epicenters in orange and red locate again predominantly within the southern central rift valley. Regarding seismic moment it seems as if most of the seismic moment (medium and moderately high release in yellow and orange) got released within the southern central rift valley at the end of phase two. The end of phase two also designates a marked drop in seismicity. Low energy events (blue and light blue colors) seem to be located at the southern rift walls.

Phase 3: (Figs. 5.8(a), 5.8(b))

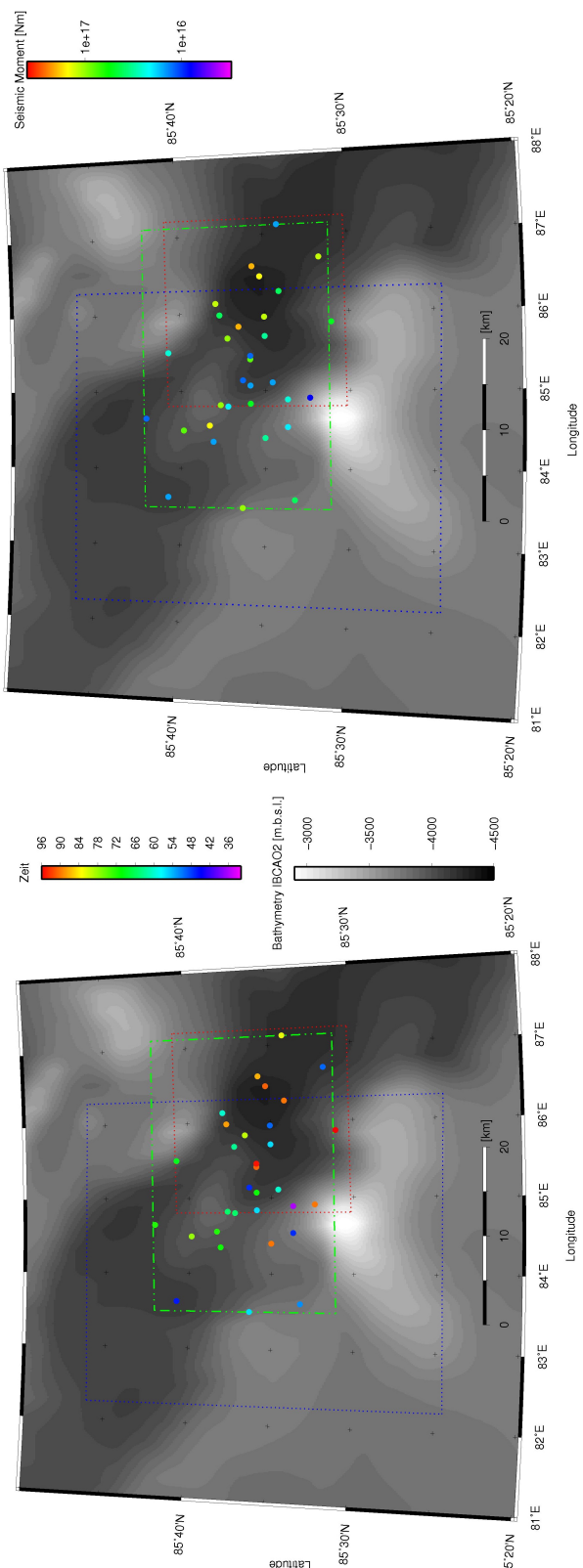
Phase 3 at day 96 starts where phase 2 left off, at the southern flanks and within the southern central rift valley with events in violet and dark blue. Later on, epicenters in green locate more northwesterly, farther away from the volcanic center. Seismic moment release again shows the highest values at the southern central rift valley and at the southern flanks. In comparison the rift flanks more northwestwards release comparatively low seismic moment. The last well-located event was also the very last event of the whole swarm on September, 24th far to the southeast at the southern flanks.

In conclusion events seem to indicate spatiotemporal clustering with clusters at the southern rift valley flanks, and the northern- and the southern central rift valley but no clear direction of migration. Seismicity seems to be episodic, with consecutive activation of spatiotemporal areas.



(b) Released seismic moment

Figure 5.6: Spatiotemporal development of epicenters for phase 1. The corresponding activated area is marked by a dashed line. Activated area of Phase 2 and 3 are marked by a dotted line in the corresponding color.



(a) Temporal development

(b) Released seismic moment

Figure 5.7: Spatiotemporal development of epicenters for phase 2. The corresponding activated area is marked by a dashed line. Activated area of Phase 1 and 3 are marked by a dotted line in the corresponding color.

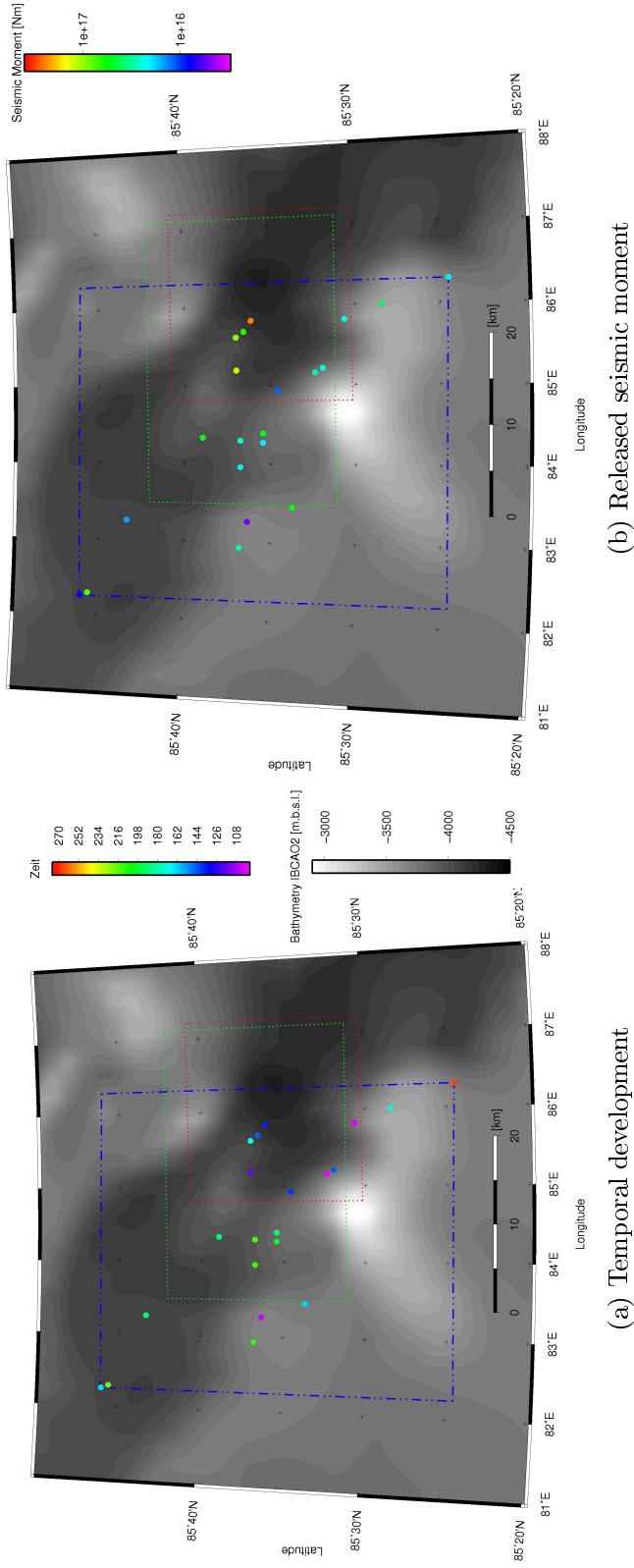


Figure 5.8: Spatiotemporal development of epicenters for phase 3. The corresponding activated area is marked by a dashed line. Activated area of Phase 1 and 2 are marked by a dotted line in the corresponding color.

5.3 Source Mechanisms

Moment tensor solutions can point to possible geological source mechanisms. The moment tensor itself is three dimensional and describes the radiation pattern of an energy source (i.e. an earthquake) through, ideally, definition of a double-couple force which describes a simple shear failure on a planar fault. The focal mechanism consists of two perpendicular nodal planes, the fault surface and the auxiliary plane, which in turn are described by three parameters, strike, dip and rake. More complicated source processes with volume change require non-double-couple source mechanisms which are also represented by the full moment tensor solution. These solutions are only possible if station coverage is good and arrival times are well defined to detect compressional or dilatational onset within the seismograms. For the best constrained 21 events of the 1999 Gakkle ridge earthquake swarm, the Harvard Centroid Moment Tensor (CMT)-catalogue (*CMT*, 2009) gives source mechanisms, discussed in chapter 5.1.

Plotting the focal mechanisms of the CMT-catalogue in relation to seismic moment over time characterizes the three phases (Fig. 5.9). For the high seismic moment release of phase 1 the CMT solutions are exclusively pure normal faulting. Phase 2 is characterized at first by again normal faulting mechanisms but at the beginning of March the source mechanisms are getting more diverse and include non-double-couple parts which are complex rupture mechanism not easily interpretable. The non-double-couple part of focal mechanisms is most pronounced within phase 3 in almost exclusively moment tensors which cannot be explained by pure double-couples.

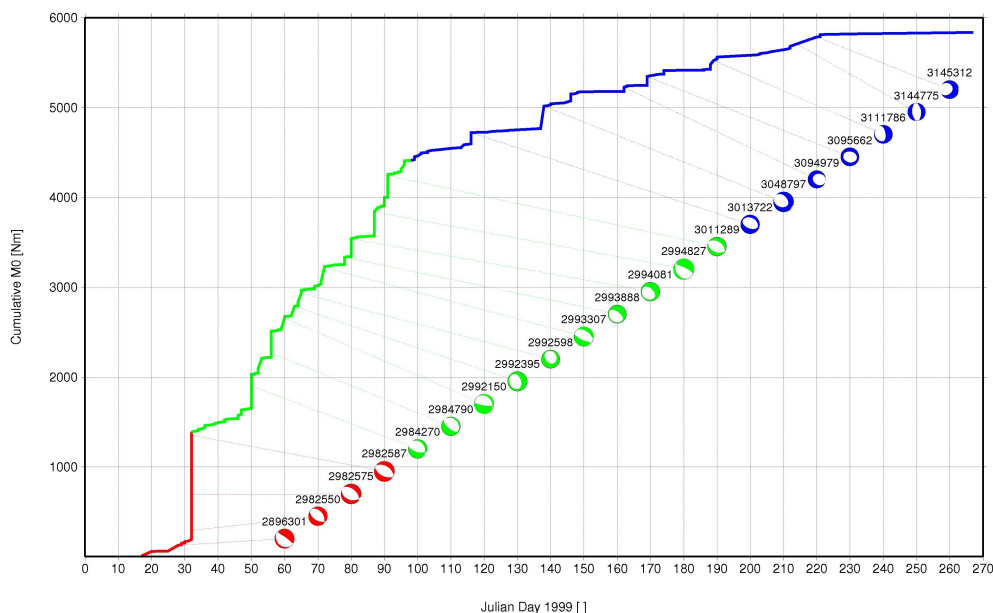


Figure 5.9: Seismic moment release for all events, plotted for phase 1-3 together with source mechanisms from the Harvard CMT-catalogue.

A visualization of the CMT-source mechanisms at their maximum likelihood epicentral location places the normal-faulting solutions of phase 1 exclusively within the center of the rift valley (Fig. 5.10). The non-double-couple mechanisms of phase 2 are found also within the central rift valley (Fig. 5.11). The source mechanisms of phase 3 are located from the volcanic center on northwestwards, both at the rift valley walls and within the central rift valley (Fig. 5.12).

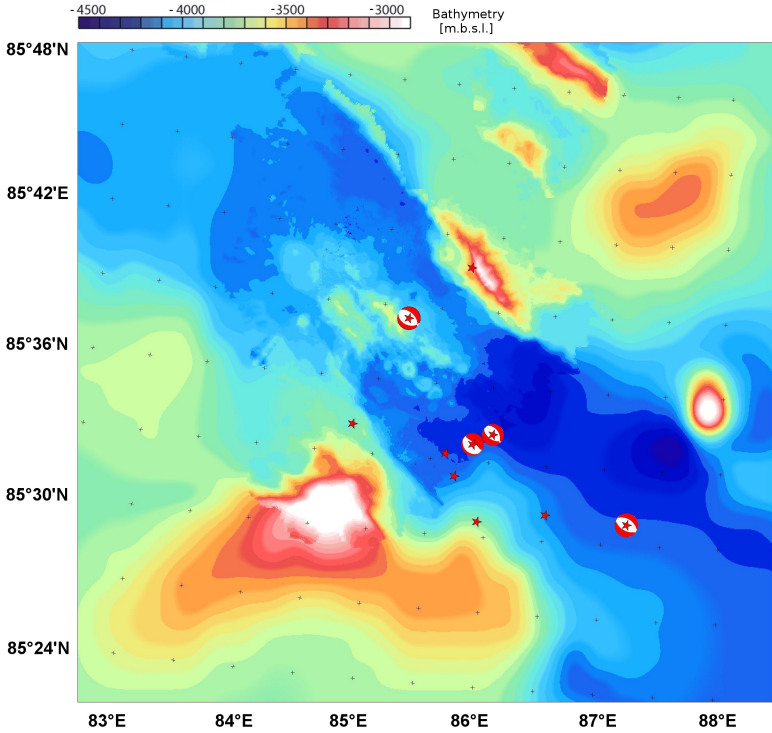


Figure 5.10: Focal mechanisms of CMT-solutions overlying the epicenters of the well-located dataset for temporal phase 1.

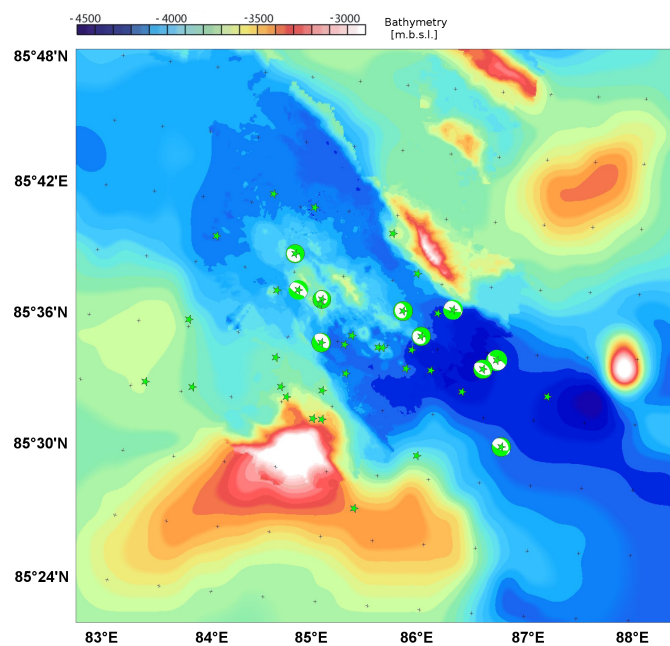


Figure 5.11: Focal mechanisms of CMT-solutions overlying the epicenters of the well-located dataset for temporal phase 2.

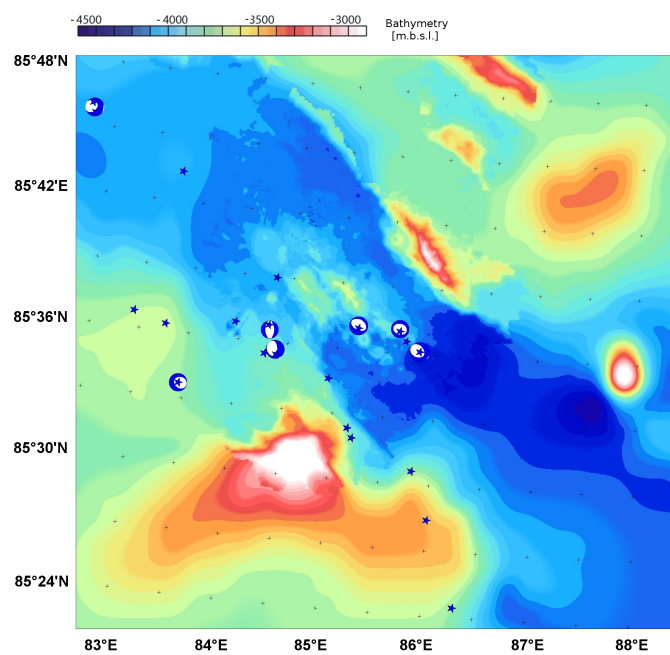


Figure 5.12: Focal mechanisms of CMT-solutions overlying the epicenters of the well-located dataset for temporal phase 3.

I investigated three highly correlating events at the crossover time-window between the ending of phase 2 and the beginning of phase 3 as reported by *Riedel and Schlindwein* (2009) for their source mechanisms (Tbl. 5.4). All of these events were among the well-located dataset which ensures a reasonable well-distributed station coverage.

Date	Source time	Longitude	Latitude	m_b
1999 04 05	08 hr 08 min 42.8 sec	85.45166°	85.598145°	4.6
1999 04 06	10 hr 05 min 31.0 sec	85.869141°	85.517578°	4.5
1999 04 09	01 hr 06 min 5.3 sec	85.158691°	85.539551°	4.6

Table 5.4: Three highly correlating events with location, magnitude and first motion.

I calculated for the best fitting double-couples with the programm focmec. I used the NonLinLoc location as epicenter and as depth I fixed 15 km for all of these events. I picked P-wave first motion only if the first motion was observable in the unfiltered data. The parameters which were set for calculation are given in Tbl. 5.5.

Date	First motion picks	Allowed polarity mismatches	Increment
1999 04 05	22	1	5°
1999 04 06	11	1	17°
1999 04 09	17	2	5°

Table 5.5: Characteristics of calculation of focal mechanisms for three crossover-events.

All three events can be explained by source mechanisms that do not require non-double-couple parts. The best defined focal mechanism was calculated for the first event at April, 5th. There is a very well defined distinction between stations with compressive first motion and stations which record a dilatational first motion, describing an oblique-slip solution (Fig. 5.13).

The second event on April, 6th is less defined with a high increment in the calculation of solutions which indicates that multiple solution fit the data (Fig. 5.14), even though a oblique-slip faulting mechanism is indicated here too. Individual focal mechanisms differ a bit, but the nodal plane for the 53° and the 66° strike are similar to solutions for the April, 5th event.

The event on April, 9th gives again a reasonable good focal mechanism, this time characterizing purely strike-slip with a vertical slip direction (Fig. 5.15). All three events share an orientation of the likely fault plane parallel to the rift axis.

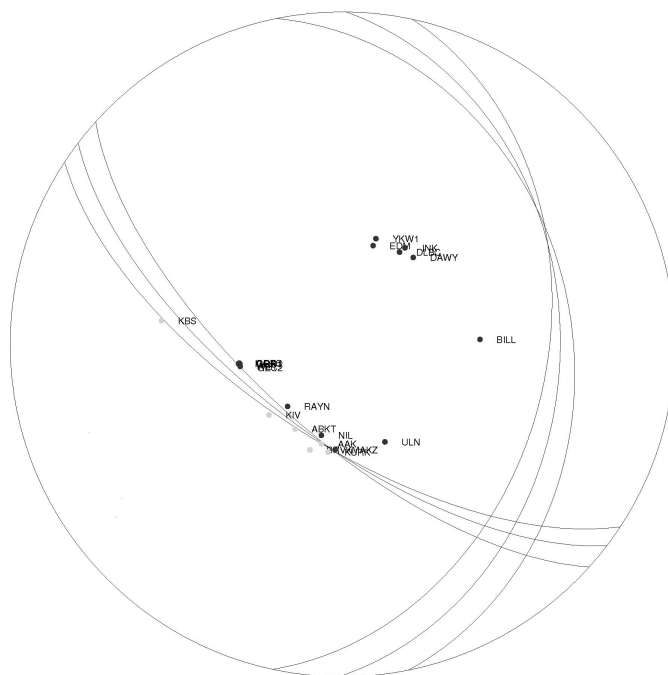


Figure 5.13: Focal mechanism solutions for the event on April, 5th.

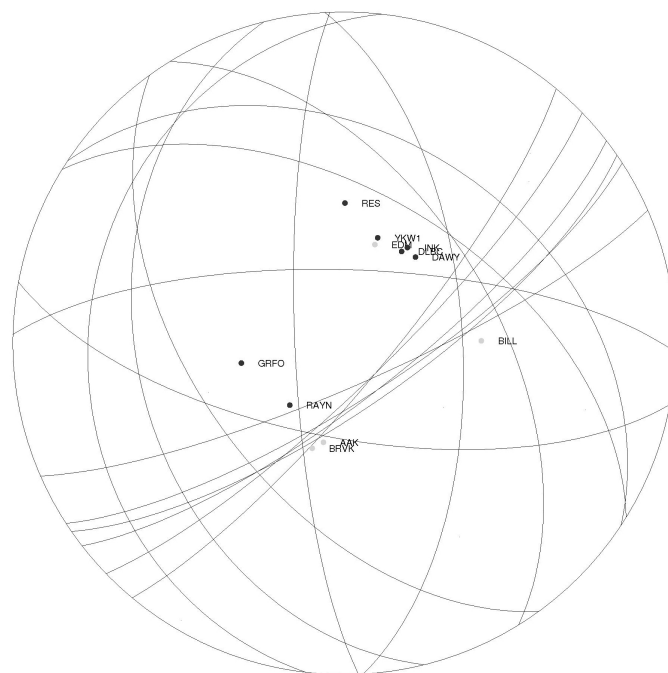


Figure 5.14: Focal mechanism solutions for the event on April, 6th.

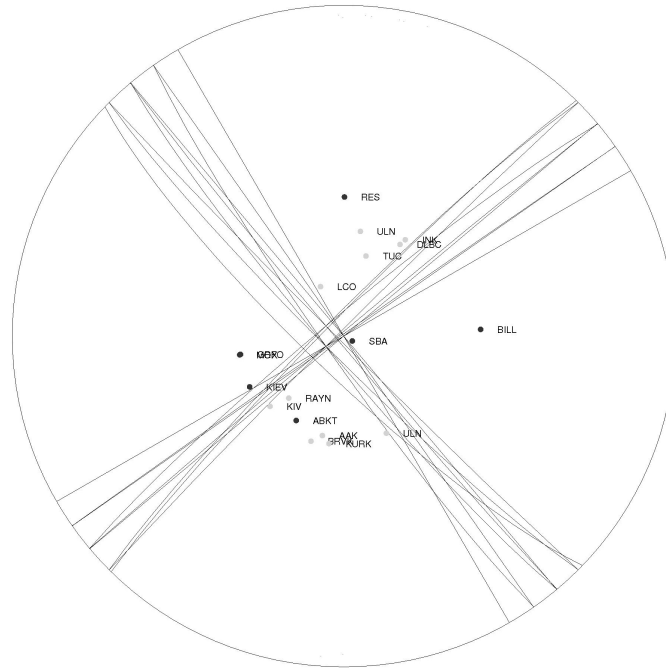


Figure 5.15: Focal mechanism solutions for the event on April, 9th.

Riedel and Schlindwein (2009) speculated that these three events should have a non-double-couple solution based on general compressive P-wave first motion which they detected in filtered waveform data recorded by surrounding stations and interpreted these events as signs of potential vent opening and onset of eruption. In contrast to their speculation, I find calculated double-couple solutions for these three events and can find no evidence of a general compressive P-wave first motion within the unfiltered dataset (Tbl. 5.6).

In summary, a plot for the epicenters of all events for which focal-mechanism exist places most of them within the central rift valley (Fig. 5.16). The crossover-events of the transition between phase 2 and phase 3 are exclusively double-couple oblique-slip events with both the events of April 6th and April 9th located at the southern rift valley wall. The location of the April 6th event corresponds with the source of the sound-signals found by *Schlindwein and Riedel* (2010).

1999 04 05	Station	First motion	Station	First motion
	AAK	D	INK	C
	ABKT	D	KBS	D
	BILL	C	KIV	D
	BRVK	D	KURK	D
	DAWY	C	MAKZ	C
	DLBC	C	MOX	C
	EDM	C	NIL	C
	GEC2	D	RAYN	C
	GRB1	C	ULN	C
	GRC1	C	WET	C
	GRFO	C	YKW1	D
1999 04 06	Station	First motion	Station	First motion
	AAK	D	GRFO	C
	BILL	D	INK	C
	BRVK	D	RAYN	C
	DAWY	C	RES	C
	DLBC	C	YKW1	C
	EDM	D		
1999 04 09	Station	First motion	Station	First motion
	AAK	D	KURK	D
	ABKT	C	LCO	D
	BILL	C	MOX	C
	BRVK	D	RAYN	D
	DLBC	D	RES	C
	GRFO	C	SBA	C
	INK	D	TUC	D
	KIEV	C	ULN	D
	KIV	D		

Table 5.6: P-wave first motion of all picks for the three crossover-events.

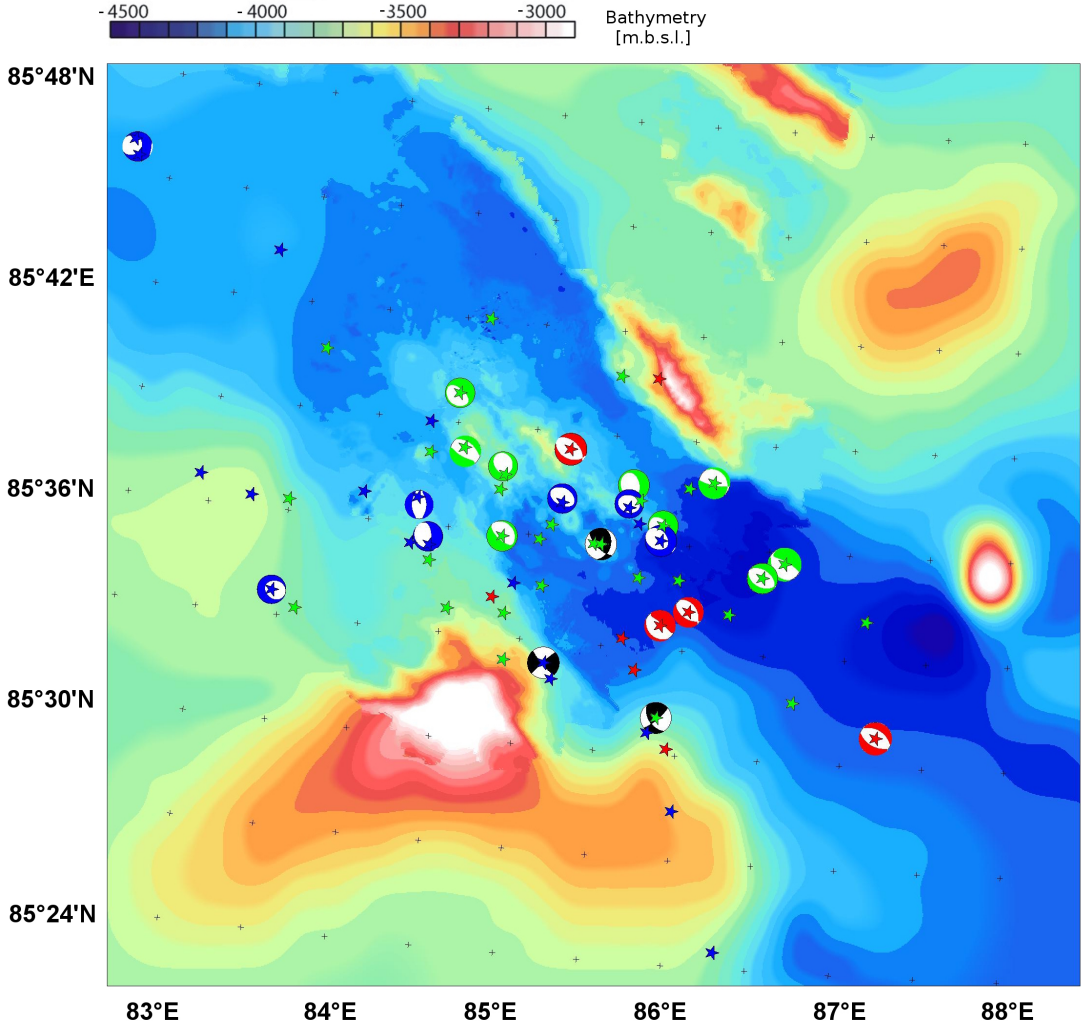


Figure 5.16: Focal mechanisms of the CMT-solutions (plotted in the color of their corresponding temporal phase: red for phase 1, green for phase 2, blue for phase 3) and the three crossover-events (plotted in black, best solution) overlying the 63 well-located epicenters.

5.4 Final Evaluation of the 1999 Earthquake Swarm

Based on the preceding analyses, the following geological scenario for the 1999 earthquake swarm at Gakkel Ridge can be proposed:

Within temporal **phase 1** (January 17th-February 1st) high seismicity and high released seismic moment are connected with a low b-value of 0.96 and purely normal faulting events, indicating purely tectonic events. The events for which focal mechanisms are calculated take place solely within the central rift valley and at adjacent faults, within a narrow total activated area. This phase can be interpreted as a breaking of cold, brittle crust.

In **phase 2**, seismicity is also high but stretched out over a longer time (February 2th-April 6th) and a larger area. Seismic moment release is constantly high but less than within phase 1, with moment tensor solutions displaying about half of the events with non-double-couple parts which indicates some kind of volumetric change. *Foulger et al.* (1994) notes that a heterogeneous stress field with both shear sources and non-double-couple focal mechanisms follows closely a crustal spreading episode. This would also be supported by the sudden increase of the b-value to 1.30. A high b-value indicates heterogeneous crust which cannot support a high stress field and is indicative of volcanic swarm events. In addition, *Arnott and Foulger* (1994) observed that considerable seismicity can be induced by fluid-involvement within a geothermal field and high fracturing may provide a conduit for magmatic dyking. This interpretation would be in agreement with the data as the relocation concentrates seismicity in spatiotemporal clusters (Fig. 5.7(a)) which, seen in connection with the moment tensor solutions (Fig. 5.11) might indicate magmatic pulses. *Tolstoy et al.* (2001) also interpreted the shifting of the area of seismicity to the northwest as indication of a succession of vertical magmatic pulses from a deep source. The end of phase 2 is characterized by medium- to moderately high seismic energy events, centered within the southern central rift valley.

The start of **Phase 3** (April 6th-September 24th) is marked by a drop in seismicity rate. The b-value stays high, with even more events displaying non-double-couple parts. Seismicity starts at the southern rift flanks, southeastwards of the volcanic complex and releases low energy. Three highly correlating events at 5th, 6th and 9th April display strike-slip solutions within this area (Fig. 5.16). *Bergman and Solomon* (1990) found that a volcanic event on a mid-ocean ridge seems to go along with a drop in seismicity rate and low energy release. A marked decrease in the seismic event rate was also observed at the Krafla volcanic episode 1975-1984 by *Einarsson and Brandsdottir* (1980) and interpreted by *Dahm et al.* (2010) to represent a halt in dyke propagation with subsequent dyke expansion which would also go along with volumetric moment tensor solutions. This would tentatively support the hypothesis of *Riedel and Schlindwein* (2009) that on about April 6th a volcanic event took place in or around the southern rift valley. *Sohn et al.* (2008) observed only a light dusting of pyroclastic deposits on the freshest looking lava

flows, placed within Oden and Loke volcanoes. This would indicate them as one potential source of this supposed volcanic event. However, a clear epicenter is absent in the data as the area in question, which had relatively high energy release in phase 2, is suspiciously seismically quiet in phase 3. Later in the 1999 Gakkel ridge earthquake swarm, a series of relatively low energy events within the northwestern rift valley took place. A lack of a clear migration of epicenters in the northwestern direction as postulated by *Tolstoy et al.* (2001) probably indicates therefore a late adjustment of the stress field to the new regime.

In summary, a purely tectonic nature of this unusually strong teleseismic earthquake swarm as noted for a compilation of teleseismically recorded earthquake swarms at the Mid-Atlantic Ridge (*Bergman and Solomon, 1990*) fails to account for the seismic characteristics of the 1999 Gakkel ridge swarm. An interplay between tectonic and magmatic events is indicated by the previous analysis. The observation of various signs of recent volcanic activity in 2001, including persistent hydrothermal venting (*Baker et al., 2004; Edmonds et al., 2003; Stranne et al., 2010*) and ongoing eruption sounds (*Schlundwein and Riedel, 2010; Schlundwein and Linder, 2007*) yields supporting evidence for an onset of magmatic dyking or effusion during the 1999 earthquake swarm.

5.5 Outlook

The question how the 1999 earthquake swarm relates in time and space to a potential volcanic eruption during that time period cannot be answered based on teleseismic data alone. Most of the seismicity related to volcanic eruptions is well below the detection threshold of teleseismic recording stations. Therefore, volcanic events and seismic structure in this area remain a subject of speculation.

In 2007, *Schlindwein and Linder* (2007) recorded over 400 microearthquakes at the 85°E volcanic complex with three seismic arrays on drifting ice-floes. The locations of the seismometer-arrays changed constantly due to the drifting ice, giving a good coverage which will be used in seismic tomography. An investigation aimed at seismic velocities and attenuation at the 85°E volcanic complex could identify structures with increased temperature, which may have been active in 1999, leading to a geologic reinterpretation.

With regard to testing of the localization algorithm NonLinLoc, a major result was the stable localization by NonLinLoc which was calculated independent of the conventional least-squares method. An investigation if this result is further applicable for teleseismic earthquake localization with a different dataset at Lena Trough will also be done.

Acknowledgements

First and foremost I want to express special and sincere gratitude to my scientific advisors at the Vienna University of Technology, Austria and the Alfred-Wegener-Institute in Bremerhaven, Germany. Without the support I got from both scientists, this work would never have been what it now is.

At the Vienna University of Technology I highly valued the penetrating questions of Ewald Brueckl. Our meetings always helped to refine my objectives and therefore improved the overall quality of my work considerably. I am very grateful that he consented to supervise my work and want to express sincere thanks.

Vera Schlindwein of the Alfred-Wegener-Institute in Bremerhaven has been an exceptional skillful and supportive on-site supervisor who provided not only perceptive criticism and scientific support, but who also initiated MOVE - Mid Ocean Ridge Volcanoes and Earthquakes. This DFG-supported Emmy-Noether Young Scientists Group was the framework of this scientific project. The exciting and collaborative atmosphere within our group contributed an element of enthusiasm which would have been difficult to find elsewhere.

Particular thanks I own to Anthony Lomax, who programmed the earthquake localization algorithm NonLinLoc which I used extensively. I greatly appreciated his help in troubleshooting and his willingness to answer a ton of questions.

I also want to express my gratitude to Bruno Meurers of the University of Vienna who made it possible that I could accept this diploma thesis and to Wilfried Jokat of the Geophysics Department at the Alfred-Wegener-Institute in Bremerhaven who provided infrastructure and importantly, many scientists who would discuss, question, encourage or simply be there to chat with when needed.

What would this work be without people who often made crucial contributions which had nothing whatsoever to do with seismology or university? For providing a sympathetic ear when my spirits were down, a helping hand at papering the kitchen, for feeding my cats when I was away taking an exam, and the occasional invitation to Sushi .. and many other unacknowledged odds and ends I now say a resounding 'Thank you!', addressed to the community of family, friends and colleagues out there!

Bibliography

- Arnott, S., and G. Foulger (1994), The Krafla spreading segment, Iceland. 1. Three-dimensional crustal structure and the spatial and temporal distribution of local earthquakes, *J. Geophys. Res.*, *99*(B12), 23,801-23,825, doi:10.1029/94JB01465.
- Baker, E., H. Edmonds, P. Michael, W. Bach, H. Dick, J. Snow, S. Walker, N. Banerjee, and C. Langmuir (2004), Hydrothermal venting in magma deserts: The ultraslow-spreading Gakkel and Southwest Indian Ridges, *Geochem. Geophys. Geosyst.*, *5*(8), doi:10.1029/2004GC000712.
- Bergman, E., and S. Solomon (1990), Earthquake Swarms on the Mid-Atlantic Ridge: Products of Magmatism or Extensional Tectonics?, *J. Geophys. Res.*, *95*, 4,943-4,965.
- Boudier, F., A. Nicolas, and B. Ildefonse (1996), Magma chambers in the Oman ophiolite: fed from the top and the bottom, *Earth Planet. Sci. Lett.*, *144*, 239-250, doi:10.1016/0012-821X(96)00167-7.
- Bown, J., and R. White (1994), Variation with spreading rate of oceanic crustal thickness and geochemistry, *Earth Planet. Sci. Lett.*, *121*, 435-449, doi:10.1016/0012-821X(94)90082-5.
- Cannat, M. (1993), Emplacement of Mantle Rocks in the Seafloor at Mid-Ocean Ridges, *J. Geophys. Res.*, *98*, 4,163-4,172, doi:10.1029/92JB02221.
- Chadwick, W., K. Cashman, R. Embley, H. Matsumoto, R. Dziak, C. de Ronde, T. Lau, N. Deardorff, and S. Merle (2008), Direct video and hydrophone observations of submarine explosive eruptions at NW Rota-1 volcano, Mariana arc, *J. Geophys. Res.*, *113*, doi:10.1029/2007JB005215.
- Chen, Y., and W. Morgan (1990), Rift Valley/No Rift Valley Transition at Mid-Ocean Ridges, *J. Geophys. Res.*, *95* (B11), 17,571-17,581, doi:10.1029/JB095iB11p17571.
- CMT (2009), Harvard Centroid Moment Tensor Project, On-line Bulletin, <http://www.seismology.harvard.edu/projects/CMT/>.
- Cochran, J. (2008), Seamount volcanism along the Gakkel Ridge, Arctic Ocean, *Geophys. J. Int.*, *174*, 1,153-1,173, doi:10.1111/j.1365-246X.2008.03860.x.

- Cochran, J., G. Kurras, M. Edwards, and B. Coakley (2003), The Gakkel ridge: Bathymetry, gravity anomalies and crustal accretion at extremely slow spreading rates, *J. Geophys. Res.*, doi:10.1029/2002JB001839.
- Crane, K., L. Johnson, B. Applegate, C. Nishimura, R. Buck, C. Jones, P. Vogt, and R. Kos'Yan (1997), Volcanic and Seismic Swarm Events on the Reykjanes Ridge and Their Similarities to Events in Iceland: Results of a Rapid Response Mission, *Marine Geophysical Researches*, *19*, 319-338, doi:10.1023/A:1004298425881.
- Dahm, T., B. Brandsdottir, and P. Einarsson (2010), Linking an injection fracture model to seismicity: Application to the Krafla 1975-1984 Caldera unrest episode (Iceland) to estimate overpressure, acting stress gradients and variations of dike opening, *Geophysical Research Abstracts*, *12*, 7,701-1.
- DeMets, C., R. Gordon, D. Argus, and S. Stein (1994), Effect of recent revisions to the geomagnetic reversal time scale on estimates of current plate motions, *Geophys. Res. Lett.*, *21*, 2191-2194.
- Dick, H., J. Lin, and H. Schouten (2003), An ultraslow-spreading class of ocean ridge, *Nature*, *426*, 405-412, doi:10.1038/nature02128.
- Dziak, R., and C. Fox (1999), The January 1998 earthquake swarm at Axial Volcano, Juan de Fuca Ridge: Evidence for submarine volcanic activity, *Geophys. Res. Lett.*, *26*, 3,429-3,432, doi:10.1029/1999GL002332.
- Dziak, R., C. Fox, and A. Schreiner (1995), The June-July 1993 seismo-acoustic event at CoAxial segment, Juan de Fuca Ridge: Evidence for a lateral dike injection, *Geophys. Res. Lett.*, *22*, doi:10.1029/94/GL01857.
- Dziewonski, A., and D. Anderson (1981), Preliminary reference Earth model, *Phys. Earth Planet. Inter.*, *25*, 297-356.
- Edmonds, H., et al. (2003), Discovery of abundant hydrothermal venting on the ultraslow-spreading Gakkel ridge in the Arctic Ocean, *Nature*, *421*, 252-256, doi:10.1038/nature01351.
- Edwards, M., G. Kurras, M. Tolstoy, D. Bohnenstiel, B. Coakley, and J. Cochran (2001), Evidence of recent volcanic activity on the ultraslow-spreading Gakkel Ridge, *Nature*, *409*, 808-812.
- Einarsson, P., and B. Brandsdottir (1980), Seismological evidence for lateral magma intrusion during the July 1978 deflation of the Krafla volcano in NE-Iceland, *J. Geophys.*, *47*, 160-165.
- Engen, O., and O. Eldholm (2003), The Arctic plate boundary, *J. Geophys. Res.*, *108*, 5.1-5.16, doi:10.1029/2002JB001809.

- Escartin, J., D. Smith, J. Cann, H. Schouten, C. Langmuir, and S. Escrig (2008), Central role of detachment faults in accretion of slow-spreading oceanic lithosphere, *Nature*, *455*, 790-795, doi:10.1038/nature07333.
- Foulger, G., R. Long, P. Einarsson, and A. Bjornsson (1994), Implosive earthquakes at the active accretionary plate boundary in northern Iceland, *Nature*, *337*, 640-642, doi:10.1038/337640a0.
- Fox, C., and R. Dziak (1998), Hydroacoustic detection of volcanic activity on the Gorda Ridge, February-March 1996, *Deep-Sea Res.*, *II(45)*, 2,513-2,530, doi:10.1016/S0967-0645(98)00081-2.
- Goldstein, S., G. Soffer, C. Langmuir, K. Lehnert, D. Graham, and P. Michael (2008), Origin of a 'Southern Hemisphere' geochemical signature in the Arctic upper mantle, *Nature*, *453*, doi:10.1038/nature06919.
- Henstock, T., A. Woods, and R. White (1992), The Accretion of Oceanic Crust by Episodic Sill Intrusion, *J. Geophys. Res.*, *98*, 4,143-4,161, doi:10.1029/92JB02661.
- IDC (2000), CTBTO Preparatory commission, vienna international centre, <http://www.ctbto.org/>.
- ISC (2008), International Seismological Centre, Thatcham, United Kingdom, *On-line Bulletin*, <http://www.isc.ac.uk/Bull>.
- Jokat, W., and M. Schmidt-Aursch (2007), Geophysical characteristics of the ultraslow spreading Gakkel ridge, Arctic Ocean, *Geophys. J. Int.*, *168*, 983-998, doi:10.1111/j.1365-246X.2006.03278.x.
- Jokat, W., O. Ritzmann, M. Schmidt-Aursch, S. Drachev, S. Gauger, and J. Snow (2003), Geophysical evidence for reduced melt production on the Arctic ultraslow Gakkel mid-ocean ridge, *Nature*, *423*, 962-965, doi:10.1038/nature01706.
- Kelemen, P., K. Koga, and N. Shimizu (1997), Geochemistry of gabbro sills in the crust-mantle transition zone of the Oman ophiolite: Implications for the origin of the oceanic lower crust, *Earth Planet. Sci. Lett.*, *146*, 475-488.
- Kennett, B., and E. Engdahl (1991), Traveltimes for global earthquake location and phase identification - IASP 91 model, *Geophys. J. Int.*, *105*, 429-465.
- Kennett, B., E. Engdahl, and R. Buland (1995), Constraints on seismic velocities in the Earth from travel times, *Geophys. J. Int.*, *122*, 108-124, doi:10.1111/j.1365-246X.1995.tb03540.x.
- Khitrov, N., E. Lebedev, A. Dorfman, and N. Bagdasarov (1983), Study of process of melting of the Kirgurich basalt by the wave method, *Geochimica*, *9*, 1,239-1,246.

BIBLIOGRAPHY

- Korenaga, J., and P. Kelemen (1998), Melt migration through the oceanic lower crust; a constraint from melt percolation modeling with finite solid diffusion, *Earth Planet. Sci. Lett.*, *156*, 1-11.
- Lavier, L., R. Buck, and N. Poliakov (1999), Self-consistent rolling-hinge model for the evolution of large-offset low-angle normal faults, *Geology*, *27*, 1,127-1,130, doi:10.1130/0091-7613.
- Le Meur, H. (1998), Tomographie tridimensionnelle a partir des temps des premieres arrivees des ondes P et S, application a la region de Patras (Grece).
- Le Meur, H., J. Virieux, and P. Podvin (1997), Seismic Tomography of the gulf of Corinth: a comparison of methods, *Ann. Geofis.*, *40*, 1-24.
- Lomax, A., J. Virieux, P. Volant, and C. Berge (2000), *Probabilistic earthquake location in 3D and layered models: Introduction of a Metropolis-Gibbs method and comparison with linear locations*, Kluwer, Amsterdam.
- Lockett, R., and D. Storchak (2006), ISCloc Routine, <http://www.isc.ac.uk/code/iscloc>.
- Macdonald, K. (1982), Mid-ocean ridges, fine scale tectonics, volcanic and hydrothermal processes within the plate-boundary zone., *Annu. Rev. Earth Planet Sci.*, *10*, 155-190.
- MacLennan, J., T. Hulme, and S. Singh (2004), Thermal models of oceanic crustal accretion: Linking geophysical, geological and petrological observations, *Geochem. Geophys. Geosyst.*, *5/2*, doi:10.1029/2003GC000605.
- Macnab, R., and M. Jakobsson (2003), The International bathymetric chart of the Arctic Ocean (IBCAO): An improved morphological framework for oceanographic investigations., *Geophys. Res. Abstr.*, *5*, 10,909.
- Magde, L., D. Sparks, and R. Detrick (1997), The relationship between buoyant mantle flow, melt migration, and gravity bull's eyes at the Mid-Atlantic Ridge between 33°N and 35°N, *Earth Planet. Sci. Lett.*, *148*, 59-67, doi:10.1016/S0012-821X(97)00039-3.
- Menke, W. (1978), Geophysical data analysis: discrete inversion theory, *International Geophysics Series*, *45*.
- Mével, C. (2003), Serpentinization of abyssal peridotites at mid-ocean ridges, *Elsevier*, *335*, 825-852, doi:10.1016/j.crte.2003.08.006.
- Michael, P., et al. (2003), Magmatic and amagmatic seafloor generation at the ultraslow-spreading Gakkel ridge, Arctic Ocean, *Nature*, *423*, 956-961, doi:10.1038/nature01704.
- Müller, C., and W. Jokat (2000), Seismic Evidence for Volcanic Activity Discovered in Central Arctic, *Eos Trans. Am. Geophys. Union*, *81*, 265-269.

- NEIC (2010), Preliminary Determination of Epicenters (PDE) Monthly Listing, <http://earthquake.usgs.gov/regional/neic/>.
- Podvin, P., and I. Lecomte (1991), Finite difference computation of traveltimes in very contrasted velocity models: a massively parallel approach and its associated tools, *Geophys. J. Int.*, *105*, 271-284.
- Quick, J., and R. Denlinger (1993), Ductile deformation and the origin of layered gabbro in ophiolites, *J. Geophys. Res.*, *98*, 14,015-14,027.
- Riedel, C., and V. Schlindwein (2009), Did the 1999 earthquake swarm on Gakkel Ridge open a volcanic conduit ? - a detailed teleseismic data analysis, *J. Seismol.*, doi:10.1007/s10950-009-9179-6.
- Rundquist, D., and P. Sobolev (2002), Seismicity of mid-ocean ridges and its geodynamic implications: a review, *Earth-Sci. Rev.*, *58*, 143-161, doi:10.1016/S0012-8252(01)00086-1.
- Schlindwein, V., and J. Linder (2007), Characteristic microearthquakes of the active submarine volcanic complex at 85°E, Gakkel ridge, *Eos Trans. AGU*, *88(52)*, Fall Meet. Suppl., OS42A-02.
- Schlindwein, V., and C. Riedel (2010), Location and source mechanism of sound signals at Gakkel ridge, Arctic Ocean: submarine Strombolian activity in the 1999-2001 volcanic episode, *Geochem. Geophys. Geosyst.*, *10*, Q01002, doi:10.1029/2009GC002706.
- Schlindwein, V., C. Müller, and W. Jokat (2005), Seismoacoustic evidence for volcanic activity on the ultraslow-spreading Gakkel Ridge, Arctic Ocean, *Geophys. Res. Lett.*, *32*, doi:10.1029/2005GL023767.
- Schlindwein, V., C. Müller, and W. Jokat (2007), Microseismicity of the ultraslow-spreading Gakkel ridge, Arctic Ocean: a pilot study, *Geophys. J. Int.*, *169*, 100-112, doi:10.1111/j.1365-246X.2006.03308.x.
- Schweitzer, J. (2001), HYPOSAT - an enhanced routine to locate seismic events, *Pure Appl. Geophys.*, *158*, 277-289.
- Sinton, J., and R. Detrick (1992), Mid-Ocean Ridge Magma Chambers, *J. Geophys. Res.*, *97*, 197-216, doi:10.1029/91JB02508.
- Sohn, R., et al. (2008), Explosive volcanism at the ultraslow-spreading Gakkel ridge, Arctic Ocean, *Nature*, *453*, 1,236-1,238, doi:10.1038/nature07075.
- Solomon, S., and D. Toomey (1992), The structure of mid-ocean ridges, *Annu. Rev. Earth Planet Sci.*, *20*, doi:10.1146/annurev.ea.20.050192.001553.
- Stein, S., and M. Wysession (2003), *An Introduction to Seismology, Earthquakes and Earth Structure*, Blackwell Publishing, ISBN: 0865420785.

BIBLIOGRAPHY

- Stranne, C., R. Sohn, B. Liljebladh, and K. Nakamura (2010), Analysis and Modelling of Hydrothermal Plume Data Acquired from the 85°E Segment of the Gakkel Ridge, *J. Geophys. Res.*, *in press*, doi:10.1029/2009JC005776.
- Tarantola, A., and B. Valette (1982), Inverse problems = quest for information, *J. Geophys.*, *50*, 159-170.
- Tolstoy, M., D. Fornari, and C. Fox (1999), Detailed investigation of T-phase swarms on the East Pacific Rise, *Eos Trans. Am. Geophys. Union*, *80*, F1073.
- Tolstoy, M., D. Bohnenstiel, M. Edwards, and G. Kurras (2001), Seismic character of volcanic activity at the ultraslow-spreading Gakkel Ridge, *Geology*, *29*(12), 1,139-1,142, doi:10.1130/0091-7613(2001)029.
- USGS (1999), <http://pubs.usgs.gov/publications/text/baseball.html>.
- Zhou, H. (1994), Rapid 3-D hypocentral determination using a master station method, *J. Geophys. Res.*, *99*, 15,439-15,455, doi:10.1029/94JB00934.

Appendix A

Abstract

In 1999 lasting over 7 months, the largest ever earthquake swarm at a mid-ocean ridge was teleseismically registered worldwide. It featured 252 recorded events, including 11 events with a magnitude $m_b \geq 5.0$ and originated from around 85°E at the eastern Gakkel Ridge (full spreading rate 6-14 mm yr⁻¹). At ultraslow spreading ridges, heat loss by conductive cooling is thought to decrease magma supply and focus magmatism in widely spaced discrete volcanic centres.

Using the ISC reviewed dataset, a relocation with the probabilistic routine NonLinLoc was tested extensively regarding the influence of velocity model, station coverage and weighting on the location result. For calculation of travel times, the velocity model AK135 combined with a regional velocity model for recording stations with epicentral distance $< 30^\circ$ was used. The dataset was reviewed with regard to the quality of the location and reduced to 63 well located events whose epicenter locations are largely independent of the above tested parameters. The 68% error in ellipse semi-major axes of the new localization is in the order of 15 km for the best events. The new locations of the epicenters show a clustering of events within the central rift valley and the southern rift flank. Comparing this probabilistic solution to that for the L2-norm-based algorithm Hyposat gives significant differences in the location for the well located dataset, the epicenters not even matching within error-ellipses. This reflects the influence of the location routine on the resulting locations.

A spatiotemporal analysis showed three distinct phases in the evolution of the swarm. In the first phase up to the 1st of February a breaking of crust activates the area. The second phase from February, 1st up to April, 6th indicates seismic release of energy through heterogeneous crust reacting to magmatic pulses. A clear volcanic event is absent in the data. Three events with highly correlating waveforms within the second week of April which were thought to indicate a volcanic eruption could be explained by strike-slip mechanisms. At around April, 6th, the third phase in the temporal evolution of the swarm characterizes probably an adjustment of the stress field to the new regime.

Appendix B

Kurzbeschreibung

Zwischen Januar und September 1999 wurde weltweit der bisher größte und längste Erdbebenschwarm an einem mittelozeanischen Rücken teleseismisch registriert. 252 Ereignisse, davon 11 Ereignisse mit $m_b \geq 5.0$ konnten bei 85°E am östlichen Gakkel Rücken (volle Spreizungsrate: $6\text{-}14 \text{ mm yr}^{-1}$) lokalisiert werden. Ultralangsame Rücken werden durch vermindertes magmatisches Angebot charakterisiert, dass diskreten Zentren fokkustiert ist.

Auf Basis korrigierter Daten von ISC wurde der Erdbebenschwarm mit dem wahrscheinlichkeitsbasierten Lokalisierungsprogramm NonLinLoc relokalisiert und die Lösung auf Einflüsse des Geschwindigkeitsmodells, der Stationsverteilung, sowie der Wichtungsverteilung untersucht. Als Geschwindigkeitsmodell wurde AK135 implementiert, während für nahe seismische Aufnehmer mit einer Epizentraldistanz von $< 30^\circ$ ein lokales Modell hinterlegt wurde. Die Lösung wurde auf 63 gut lokalisierte Epizentren beschränkt, die von oben genannten Parametern weitgehend unabhängig sind und einen 68% Fehler der Halbachsen in der Größenordnung von 15 km haben. Die neuen Epizentren häufen sich im zentralen Rifttal und an der südlichen Riftflanke. Ein Vergleich dieser Lösung mit einer Lokalisierung durch das konventionelle Programm Hyposat zeigt eine Unvereinbarkeit beider Lösungen auch unter Berücksichtigung der Fehlerellipsen. Dies reflektiert den Einfluss der Lokalisierungsroutine auf die Berechnung der Epizentren.

Eine räumliche und zeitliche Analyse zeigt drei klar unterscheidbare Phasen in der Entwicklung des Erdbebenschwarms. Die erste Phase dauerte bis zum 1. Februar und zeigt Aktivierung der Kruste durch tektonische Vorgänge. In der zweiten Phase bis zum 6. April wird niedrigere seismische Energie in heterogener Kruste als Reaktion auf magmatische Vorgänge freigesetzt. Ein klares vulkanisches Ereignis ist nicht in den Daten sichtbar. Drei Ereignisse mit gut korrelierenden Wellenformen in der zweiten Aprilwoche, von denen man bisher dachte dass sie ein vulkanisches Ereignis anzeigen könnten, können jedoch durch Blattverschiebungen erklärt werden. In der dritten Phase zeigen die Beben möglicherweise eine Anpassung des Spannungsfeldes an die veränderten Bedingungen.



EDITH KORGER

Geophysicist in training, University of Vienna

Residency: Georg-Seebeck-Str 60, D – 27570 Bremerhaven

Phone / eMail: +49-176-85256800, edith.korger@awi.de

Date / Place of Birth: 13th of September 1975, Vienna
Austrian Citizenship

TRAINING - GEOPHYSICS

08/30/2009 - 09/11/2009

ECORD Summer School

Geodynamics of mid-ocean ridges

11/2006

University of Natural Resources & Applied Life Sciences, Vienna

Blasting technician, Certificate of Competence in Austria

Since 10/2005

University of Vienna – Diploma Study in Geophysics

Diploma thesis: Nonlinear relocalization of the 1999 earthquake swarm on Gakkel Ridge, Arctic Ocean

1st Level completed on January 11th, 2007

JOB EXPERIENCE - GEOPHYSICS

Since 05/01/2010

Alfred-Wegener-Institute for polar- and marine research

Research Assistant: Seismology

02/16/2009 - 11/16/2009

Alfred-Wegener-Institute for polar- and marine research

Student Assistant: Seismology

10/01/2009 - 03/31/2010

10/01/2008 - 03/31/2009

Leopold-Franzens-Universität Innsbruck

Tutor: Geophysical Data Acquisition

09/01/2008 - 09/31/2008

ZAMG - Zentralanstalt für Meteorologie und Geophysik

Internship: Seismologischer Dienst

Compilation of macroseismic intensityplots

08/11/2008 - 08/31/2008

08/01/2007 - 08/31/2007

07/01/2006 - 08/31/2006

OMV Exploration and Production GmbH

Internships: Seismic Department

- Survey Geometry Evaluation

- Evaluation of statical corrections

- Preserved Amplitude Processing

07/04/2008 - 08/10/2008

Alfred Wegener Institut für Polar- und Meeresforschung

Student Assistant: Seismological Measurements on Ice Floes

FS Polarstern, ARK23/2 - Fram Strait

08/2008, 06/2007, 10/2007

Univ. Prof. Dr. Peter Steinhauser

Student Assistant: Seismic Measurements

03/12/2006 - 03/29/2006

GFZ - GeoForschungsZentrum Potsdam

Student Assistant: Seismic Measurements (Israel)

JOB EXPERIENCE - ADMINISTRATION

11/2004 – 07/2005	<p>UPS-SCS Logistics, Headquarters Austria Assistant of Management (Logistics)</p> <p>Responsibilities: Office- & Travel-Management, Time monitoring, Graphical and numerical statistics, Correspondence in German and English</p>
11/2003 – 07/2004	<p>Docu AG - Austria Assistant of Management (Publishing Industry)</p> <p>Responsibilities: Office- & Travel-Management, Graphical and numerical statistics, Conception of - as well as employee training on a customer data base, Interface between graphical agencies and customers</p>
09/2002 – 07/2003	<p>Manpower Austria – Temporary employment company for Boehringer Ingelheim Austria Project Assistant, Data Base Support (Pharmaceutical Industry)</p> <p>Responsibilities: Team Assistant, Data Base Conception (MS Access 97), Administration of documents, Correspondence in German and English</p>
[2001/2002]	[<i>SAE Technology College (Administrative Training)</i>]
01/1999 – 12/2000	<p>Melbrosin International GesmbH Desk Clerk (pharmaceutical industry)</p> <p>Responsibilities: Office-Management, Correspondence in German and English, Travel organisation, Administration of database for trademarks</p>
03/1997 – 12/1999	<p>Psychotechnisches Institut Wien Back office (Market research)</p> <p>Responsibilities: Graphical and numerical statistics (MS Powerpoint 97), Organisation of market researchs, Reporting</p>
08/1996 – 02/1997	<p>Torrex Pharma GesmbH Desk Clerk (pharmaceutical industry)</p> <p>Responsibilities: Graphical and numerical statistics, Correspondence in German and English, Inventory control</p>

SPECIALIZED KNOWLEDGE & QUALIFICATIONS

Processing Software:	Geocluster (CGG), Promax, Reflex, LAB
Seismological Software:	NonLinLoc, Hyposat
Geoelectrical Software:	Res2/3Dinv/Mod, Surfer
Statistical Software:	Spotfire
Programming Skills:	Fortran, Matlab, awk, gmt
Operating Systems:	UNIX – bash, csh Microsoft Office
Blasting Technician:	Certificate of Competence in Austria
Foreign Languages:	English (fluent in Word and Speech)
First Language:	German
Driving Licences:	Eligible to operate motorcycles and cars

ADMINISTRATIVE TRAINING

2001/2002	SAE Technology College, Vienna Multimedia Producer, Diploma <ul style="list-style-type: none">• JavaScript, HTML• Director 8.0• FreeHand 9.0, Photoshop CS
1997	VHS Margareten, Vienna Cambridge Certificate of Advanced English
1996	Colleg for medical Administration, Vienna Medical Representative Diplom (Pharmareferentendiplom) Medical Assoziation Diplom (Ärztammerdiplom) Pharmig – Assoziation of Austrian pharmaceutical Industrie, Diplom
1995	General qualification for university entrance (Austria) BORG Vienna, 1 st District

PERSONAL INTERESTS

Geophysics (Seismology, Volcanology, Seismics)
Classical Music
Brit/amerik Sci-Fi (OV)
Scuba diving, Canoeing
Sports climbing